In situ Sintering Study of Model Nickel Catalysts

by

Malebelo Maphutha

Thesis presented to the University of Cape Town

in the fulfilment of the requirements

for the degree of

Master of Science in Engineering

Centre for Catalysis Research

Department of Chemical Engineering

University of Cape Town

Cape Town

September 2014

Acknowledgements

My sincerest gratitude goes to my supervisor Prof. Michael Claeys for giving me the opportunity to study at the University of Cape Town. His open door policy, outstanding guidance and support throughout my project were invaluable. He encouraged and motivated me during difficult times and I would not have been able to complete this manuscript without his detailed and helpful comments. I will forever be appreciative of the time and interest he invested in this project.

I would also like to sincerely thank Dr Robert Henkel for guiding me through the process of learning how to operate the *in situ* magnetometer. I am thankful for his patience and encouragement throughout my project. Special thanks also go to Dr Nico Fischer for assisting me with the *in situ* PXRD, helping me with the interpretation of the magnetic data and for reviewing and helping me complete this manuscript.

Thank you to Mohamed Jaffer for TEM analysis, particularly for always making time to analyse my samples even on short notice. Thank you to Zulfa le Riche for BET analysis, Jessica Heynes and Mbesi May for AAS analysis and Chantal Ceylon for assistance in the laboratory.

I would also like to acknowledge Sasol for the funding they provided for my studies. Also, I would like to thank DST-NRF Centre of Excellence in Catalysis c*change for the additional financial support.

Synopsis

The methanation reaction is the most basic reaction in the hydrogenation of carbon monoxide (CO) and is essential in the production of substitute (synthetic) natural gas (SNG). Nickel has been found to be the most appropriate methanation catalyst. However, deactivation by thermally induced sintering is problematic at the conditions associated with the methanation catalyst. Crystallite size plays an important role in the activity of the methanation reaction and so it becomes important to also determine the effects of crystallite size on the deactivation of the nickel catalyst.

The main objective of this study was to conduct an *in situ* magnetic investigation on the effects of crystallite size on thermally induced sintering at elevated temperatures in an inert atmosphere as well as in a steam and hydrogen atmosphere. The approach taken to meeting these objectives included the use of the microemulsion technique in synthesising unsupported nickel nanoparticles with a narrow size distribution. Use of the microemulsion technique in synthesising γ-alumina supported nanoparticles was also investigated in order to determine the most appropriate approach in the synthesis of model nickel catalysts.

The microemulsion technique proved successful in the synthesis of nickel oxide nanoparticles with a narrow size distribution, in the size range of 3 – 13 nm, where the size of the particles was linearly dependent on the water/surfactant ratio. Partial reduction of the nickel oxide nanoparticles was observed during calcination in air resulting in the simultaneous formation of nickel nanoparticles.

Two preparation methods were proposed for the synthesis of supported nickel nanoparticles: direct support addition to the microemulsion and addition of the support to already synthesised and calcined nanoparticles. Two different sizes (4 nm and 12 nm) were synthesised. Direct support addition to the microemulsion resulted in catalyst samples which displayed poor reducibility. Catalyst samples prepared according to the addition of the support to the nanoparticles showed markedly improved reducibility, making them highly suitable for a magnetic investigation.

Model catalysts were prepared by adding nickel nanoparticles (5 nm and 12 nm) with a narrow size distribution to a γ-alumina support. Although both model catalysts had

similar size distributions after reduction, they did not display similar behaviour during the sintering studies. The catalyst synthesised using smaller nanoparticles showed a far greater propensity to sinter, both in an inert and oxidising atmosphere. Steam exacerbates the sintering process.

Contents

List of figures

List of tables

Nomenclature

Abbreviations

3WV	three way valve
AAS	atomic absorption spectroscopy
BET	Brunauer-Emmett-Teller
BPR	back pressure regulator
DOR	degree of reduction
FIC	flow indicator and control
MFC	mass flow controller
NTP	normal temperature and pressure (1 atm and 293 K)
NV	needle valve
PEDGE	penta-ethyleneglycol-dodecylether
PEG	polyethylene glycol
PIC	pressure indicator and control
PRV	pressure relief valve
PXRD	powder X-ray diffraction
SMSI	strong metal support interactions
STEM	scanning transmission electron microscopy
TEM	transmission electron microscopy
TIC	temperature indicator and control

Chemical formulas

Al_2O_3	aluminium oxide (alumina)
Ar	argon
C_2H_2	ethyne
C_2H_4	ethene
C_2H_6	ethane
Cd	cadmium
Co	cobalt
CO	carbon monoxide
CO_2	carbon dioxide
$NH_4HCO_3.NH_2$	ammonium carbonate

$NiAl_2O_4$	nickel aluminate
$Ni(NO_3)_2.6H_2O$	nickel (II) hexahydrate
Fe	iron
H_2	hydrogen
H_2O	water
N_2	nitrogen
Ni	nickel
Pt	platinum
Rh	rhodium
Ru	ruthenium
SiC	silicon carbide

Notations

d	diameter	nm
k	Boltzmann constant, 1.38065048×10^{-16}	erg/K
M	magnetisation	emu
P	pressure	bar
T	temperature	°C

Greek notations

γ	percentage ferromagnetic material	%
θ	diffraction angle	°
ω	water/surfactant mass ratio	-

Subscripts

C	Curie
r	remnant
p	particle
S	saturation

1. Introduction

The methanation reaction is the most basic reaction in the hydrogenation of carbon monoxide (CO) and is expressed according to the equation:

$$CO + H_2 \leftrightarrow CH_4 + H_2O, \Delta H^0_{298K} = -206 kJ/mol \qquad \text{Equation 1}$$

It is a highly important process in the chemical industry and has a number of applications. It has long been used as the final clean-up step in ammonia synthesis plants. The methanation process is also used in the removal of trace amounts of CO from hydrogen (H_2) rich gas feeds (Karellas, *et al*., 2012), in the purification of reformate gas for fuel cells (Dagle, *et al*., 2007) and, most recently, as an essential step in the production of substitute (synthetic) natural gas (SNG) from coal or biomass (Tian, *et al*., 2013). The production of SNG from solid fuels such as coal, petcoke, biomass or waste is financially attractive because it involves the conversion and upgrade of cheap, abundant and widely distributed carbonaceous feedstock into methane rich gas which is stable for fuel supply and may be used in any existing gas infrastructure lines (Liu, *et al*., 2012). SNG poses an excellent alternative for areas which have abundant coal reserves but are poor in the natural gas resource (Chandel & Williams, 2009).

From a comprehensive analysis of raw material sources, cost and activity, the most appropriate methanation catalyst has been found to be nickel (Tian, *et al*., 2013). Current methanation catalysts are almost entirely based on nickel due to its high activity, high selectivity for methane and comparatively low price (Atkinson & Nicks, 1976; Yan, *et al*., 2013; Hwang, *et al*., 2011; Watson, 1980). However, a major problem for processes based on this methanation reaction remains the deactivation of the nickel catalyst by coking, sintering and poisoning. Agnelli, *et al*. (1998) has shown that in the absence of poisoning, the deactivation of supported nickel catalysts could primarily be due to particle sintering. During low temperature methanation, nickel has a tendency of forming volatile nickel carbonyl species,

resulting in a continuous loss of metal. This carbonyl formation is limited to temperatures below 300 °C (Rostrup-Nielsen, *et al*., 2007). However, at higher temperatures, thermally induced sintering becomes critical where the migration of atoms results in the coalescence of particles (Jensen, *et al*., 2011).

Crystallite size plays an important role in the activity of the methanation reaction. According to Boudart & McDonald (1984), decreasing crystallite size results in a higher number of surface atoms per gram of the metal being exposed and available for reaction which then suggests that there would be an increase in activity. Hence, nickel crystallite size is postulated to have an effect on the activity of the methanation reaction. Thus, by noting the importance of the effect of crystallite size on activity, it in turn becomes important to also investigate how this crystallite size affects the deactivation process, particularly thermally induced sintering.

In order to adequately study the effects of crystallite size on this sintering process, it becomes crucial to be able to synthesise model catalysts with crystallite sizes in the nanometre range and with a very narrow size distribution (Fischer, *et al*., 2011). Microemulsions are an effective means to synthesise metal or metal oxide crystallites in this nanometre size range (Barkhuizen, *et al*., 2006).

The main objective of this investigation was to synthesise unsupported and supported model nickel catalysts in the nanometre size range where the crystallites had a sufficiently narrow size distribution using the microemulsion technique. The effects of nickel crystallite size on thermally induced sintering in an inert atmosphere and in the presence of water vapour were then also studied using novel *in situ* techniques developed at the University of Cape Town: *in situ* powder X-ray diffraction (PXRD) and the *in situ* magnetometer.

2. Literature Review

2.1. Methanation reaction

The main reaction which takes place during the methanation process is given by Equation 1. Side reactions are expressed according to:

$$CO + H_2O \leftrightarrow H_2 + CO_2, \Delta H^0_{298K} = -41 kJ/mol \quad \text{Equation 2}$$

$$2CO \leftrightarrow C + CO_2, \Delta H^0_{298K} = -172 kJ/mol \quad \text{Equation 3}$$

$$CO_2 + 4H_2 \leftrightarrow CH_4 + 2H_2O, \Delta H^0_{298K} = -165 kJ/mol \quad \text{Equation 4}$$

According to Hu, *et al*. (2012), the methanation of CO can take place over a number of transition metal catalysts including Ni, Ru, Rh, Co and Fe. Ru and Rh are not economically viable for use in the large scale production of SNG because of their high cost and low availability, despite the fact that they exhibit high activity at low temperature for the removal of trace amounts of CO from H_2 rich gas streams (Gorke, *et al*., 2005; Fujita & Takezawa, 1997; Utaka, *et al*., 2003; Vannice, 1975). Cobalt is very active for the hydrogenation of carbon monoxide but is less selective than nickel for methane (Watson, 1980). Iron is also a possible methanation catalyst. It is, however, not as effective as nickel when comparing yield, activity and selectivity towards methane production (Haynes, *et al*., 1974).

Recently, the interest in the methanation process, particularly its use in SNG production, has been increasing, as evidenced by the renewed interest in the technology and catalysts associated with this process (Jensen, *et al*., 2011).

2.2. Methanation for SNG production

Jensen, *et al*. (2011) describe SNG as a high-methane replacement for natural gas. SNG can be used on-site, fed into a natural gas pipeline, or be liquefied into liquefied natural gas (LNG). Natural gas demand is projected to grow at a faster rate than general energy demand growth (Jensen, *et al*., 2011). Sudiro & Bertucco (2010) list the advantages of SNG with respect to other synthetic fuels. They note that the transport of SNG is efficient and cheap and can be done in any existing gas pipelines and distribution networks, and it can be coverted to other products in natural gas combined-cycle power plants and petrochemical facilities.

The methanation of syngas process is typically operated at high concentrations of carbon monoxide with a H_2/CO feed ratio of 3.0 and high temperatures ranging from 300 to 600 °C (Rostrup-Nielsen, Pedersen, & Sehested, 2007). Jensen, *et al*. (2011) noted that the methanation reaction is favoured at low water content and high pressures.

According to Gao, *et al*. (2012), the production of SNG is primarily based on the gasification of coal or biomass to synthesis gas (syngas). This process is particularly useful in areas which have abundant coal reserves but are poor in natural gas resources (Chandel & Williams, 2009). The syngas which emerges from gas cleaning and conditioning usually contains hydrogen, carbon monoxide, carbon dioxide, water, methane and higher hydrocarbons including C_2H_6, C_2H_4 and C_2H_2 (Haryanto, *et al*., 2009; Jurascik, *et al*., 2009). The latter increase the risk of carbon deposition on the methanation catalyst, in turn suppressing its activity. This syngas can then be converted to SNG by the catalytic hydrogenation of the carbon oxides through the methanation reaction.

Two main processes have been proposed for SNG production on an industrial scale. The first is a high temperature process (Luterbacher, *et al*., 2009, Rostrup-Nielsen, *et al*., 2007) which requires several stages for heat exchange and where the catalyst has to be exceptionally stable. The second process is low temperature methanation. This process requires rapid heat removal, resulting in decreased thermal stress for the catalyst. The catalyst of choice does, however, have to display very high activity

and stability (Huang, *et al*., 2014). Typically, fluidized bed reactors and slurry reactors are employed due to the fast heat transfer (Rahimpour, *et al*., 2012). This, however, introduces a new pathway for catalyst deactivation: attrition. Fluidized beds are exceptionally suitable for highly exothermic reactions (Rahimpour, *et al*., 2012). Liu, *et al*. (2013) found that the fluidized bed reactor, under the same conditions, gas velocities and pressures, showed higher CO conversion and selectivity to methane, much closer to thermodynamic equilibrium than the fixed bed reactor. The fluidized bed also exhibited lower sensitvity to changes in reaction pressure and space velocity. Liu, *et al*. (2013) assert that the fluidized bed shows technical superiority to the fixed bed because of the efficient heat/mass transfer and interaction between gas and solid, good uniformity in bed temperature and the surface of the catalyst is regularly regenerated as a result of attrition. Regardless of these advantages, adiabatic fied bed reactors are far more commonly employed in industry, possibly due to the high degree of expertise and experience with these reactor systems. Several fixed bed reactors are placed in series with intermediate gas coolers. Product gas recycles are also employed. A number of methanation processes based on fixed bed reactors and the gasification of coal and biomass have been developed including the Lurgi process (Mills, 1971; Lee, 2007), TREMP^{TM} technology (Jensen, *et al*., 2011), Davy process (Dave, 2013) and the HICOM process.

The methanation reaction is highly exothermic. In an attempt to decrease the reaction heat in the adiabatic fixed bed methanation process, several approaches make use of recycle streams containing water and methane (Gao, *et al*., 2012, Jensen, *et al*. 2011). In the TREMP^{TM} technology developed by Haldor Topsoe (Denmark), the product recycle controls the temperature in the first methanation reactor.

Er-rbib & Bouallou (2014) note that there are a number of economic and technical barriers which limit the widespread commercial implementation of technologies associated with SNG. The primary issue is that the methanation reaction is highly exothermic. Syngas, at a temperature of 300 °C, introduced into an adiabatic methanation reactor, may reach temperatures in excess of 900 °C due to the heat produced during the reaction. The temperature increase associated with this reaction may then result in catalyst sintering and subsequent catalyst deactivation . According to Jensen, *et al*. (2011), at the high temperatures associated with the methanation

reaction nickel crystallite growth needs to be limited in order to allow for sufficient activity in the aged catalyst. A stable support will facilitate this restriction of crystallite growth. At low temperatures, the particle migration mechanism is the dominant mechanism by which nickel catalyst sintering occurs where particles are mobile over the carrier surface, collide and coalesce (Jensen, *et al*., 2011). At higher temperatures, the sintering mechanism changes to the atom migration mechanism. This mechanism is characterised by the migration of atoms (or small agglomerates) from one particle to another (Jensen, *et al*., 2011). The cross-over temperature for the two mechanisms, according to Jensen, *et al*. (2011) is in the temperature range of 500 - 600 °C.

2.3. SNG plant overview

Figure 2.1 below is a graphical representation of a typical SNG plant.

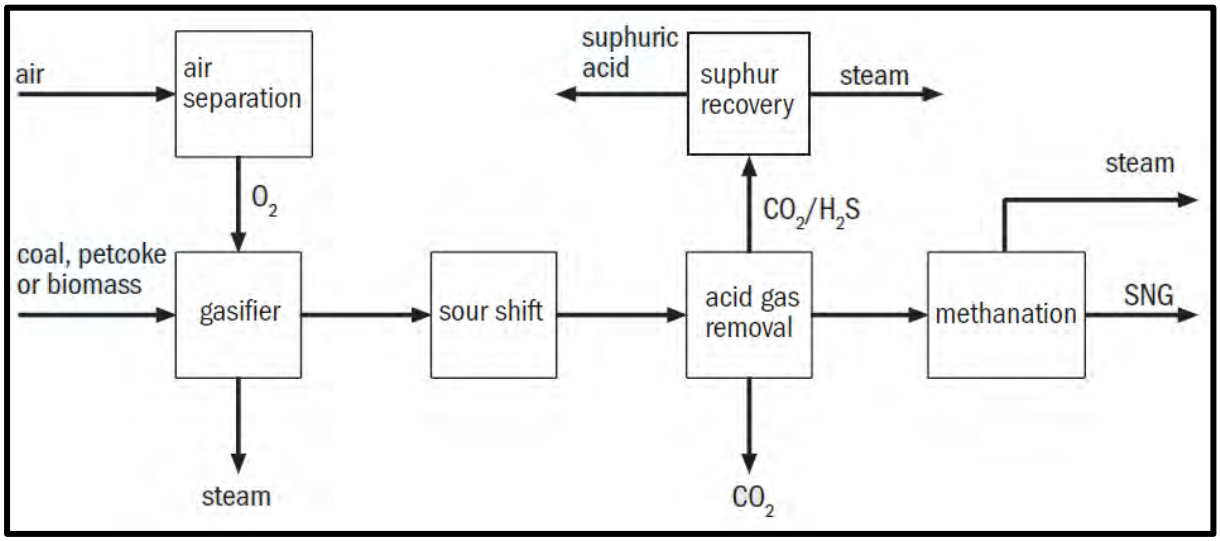

Figure 2.1.Major units of the SNG plant

Adapted from Jensen, et al. (2011)

Initially coal, petcoke or biomass is gasified in the presence of oxygen and water. The resultant gas is cooled and processed in order to remove tars, salts and dust. The sour shift unit allows for the adjustment of the hydrogen and carbon monoxide ratio by the water gas shift reaction. Emerging from the sour shift unit is syngas rich

in hydrogen sulphide and carbon dioxide, which are removed in the acid gas removal unit. Sulphur acts as a poison for methanation catalysts whilst the carbon dioxide is removed in order to obtain appropriate hydrogen to carbon ratios further downstream. Syngas then enters the methanation unit.

2.4. Crystallite size and activity in the methanation reaction

The effect of crystallite size on activity in the methanation reaction was considered. Vannice (1976) notes that the most justifiable way of comparing activity among catalysts is that normalized to unit metal surface area or to the number of reduced metal surface atoms (turnover frequency, TOF). Determination of specific activity allows for a direct comparison of the intrinsic activity of catalysts.

In order to gain an understanding of the effects of crystallite size on activity, the work by Bezemer, *et al*. (2006) was considered. They investigated the effect of cobalt particle size on activity in Fischer-Tropsch synthesis. As depicted in Figure 2.2, they found that there was an ideal crystallite size which allowed for maximum activity per gram of cobalt. It was proposed that this may be as a result of the fact that crystallites below 8 nm may not be large enough to support the step sites necessary for Fischer-Tropsch synthesis to take place, resulting in this decrease in activity.

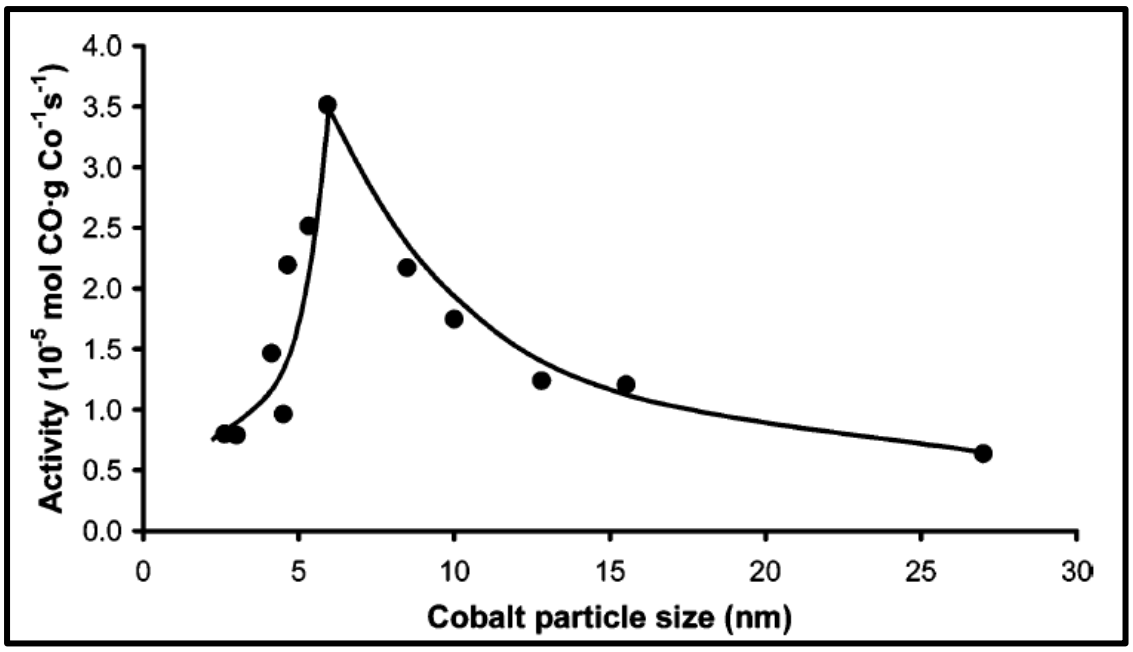

Figure 2.2: The influence of cobalt particle size on activity normalized to the cobalt loading (220 °C, H_2/CO = 2, 1 bar)

Adapted from Bezemer, et al.(2006)

The methanation reaction is a fairly simple reaction and the thermodynamic data pertaining to it is readily available in literature. Yet the detailed mechanism of the reaction on the catalytic surface has not as yet been unambiguously described (Watson, 1980). Reactions which are structure sensitive are characterised by TOF which vary appreciably with varying crystallite structure (different crystallographic planes or nanocrystallites in the 1 – 10 nm size range) (Boudart & McDonald, 1984). Structure insensitive reactions should display the opposite behaviour. It has been suggested that the methanation reaction is structure insensitive due to the comprehensive single crystal studies of methanation conducted over nickel and ruthenium. Yet, from the work conducted by Watson (1980), it is apparent that the kinetic parameters found on the basal planes of different single crystal facets and those found on supported catalysts were in agreement, suggesting that the methanation reaction was structure insensitive.

Rostrup-Nielsen, *et al*.(2007) investigated the activity and stability of a supported nickel-based catalyst (22 wt.% Ni on a stabilised support) by exposing them to

syngas which was equilibrated at high temperatures (600 - 700 °C). Hydrogen chemisorption was used to give an indication of the specific nickel surface area. They noted that the loss of methanation activity was more pronounced than the loss of the specific nickel surface area due to sintering, an eminent process at these high temperatures. The activity per unit surface area (TOF) also decreased. The authors concluded that these results indicated that the methanation reaction was highly structure sensitive. From DFT calculations the authors could show that step sites were more active than non-step sites and larger metal particles have a significantly reduced number of these step sites. Similar results were reported by Zhao, *et al*. (2012) who prepared their catalysts by the solution combustion method. In both cases, however, the crystallite size was greater than 20 nm, which may be outside the size range for the effective study of crystallite size effects.

Bartholomew, *et al*. (1980) studied the effects of support and metal dispersion on CO hydrogenation for nickel supported on alumina, silica and titania at 1.4 bar and 227 - 277 °C with a H_2 to CO ratio of four in 95 % nitrogen. They found that for Ni/Al_2O_3, the TOF decreased with increasing dispersion in the range 5 - 60 %. Dispersion is inversely proportional to particle diameter and Boudart & McDonald (1984) quantified this result: TOF increased fourfold with increasing nickel particle diameter. This trend was also observed, although less pronounced, for Ni/SiO_2. These results indicate that methanation is indeed a structure sensitive reaction.

van Meerten, *et al*. (1983) also investigated the effects of nickel crystallite size on the methanation reaction in the crystallite size range of interest. They made use of low and high field magnetisation measurements in order to gain an understanding of crystallite size and size distribution in connection with catalytic activity. Nickel on silica catalysts were prepared according to the homogeneous precipitation method with crystallite sizes ranging from 0.5 to 5 nm. Larger crystallites of up to 12 nm were obtained by exposing the crystallites to high temperatures in hydrogen and allowing them to sinter. van Meerten, *et al*. (1983) reported the activity on the basis of the initial dispersion and found that specific activity under standard conditions increases with average crystallite size from 0.6 nm up to 4.4 nm. Thereafter, the mass specific activity decreases with a further increase in nickel crystallite size up to 12.3 nm. Boudart & McDonald (1984) note that this may be because structure-sensitive reactions need a multiple-atom site or ensemble on the catalysts surface. Hence, a

structure-sensitive reaction will have an associated optimum catalyst with the most active structure.

Vannice (1976) investigated the catalytic behaviour of nickel and nickel dispersed on a number of different supports (alumina, silica and graphite) in the hydrogenation of CO reaction at 1 bar. The unsupported material was prepared using a precipitation method. The supported catalysts were synthesised using the incipient wetness technique. This involved wetting the support with an aqueous solution of nickel precursor. Vannice (1976) reported that there may be a relationship between crystallite size and activity. The highest turn over frequency was observed at the lowest particle size, contradicting the findings of the reports outlined above. However, any differences were very small at less than an order of magnitude at 205 °C. This may have been because all the synthesised particles were greater than 8 nm, perhaps outside the range where particle size effects become important.

Yet van Meerten, *et al*. (1983) found from their magnetic results that the activity of the catalyst remained almost constant during methanation, despite the crystallite distribution shifting to larger sizes and, consequently, the metal surface area decreasing. According to van Meerten, *et al*. (1983), this suggests that the sites for catalytic activity are located mainly at the larger crystallites. They confirmed that during methanation small crystallites disappear in favour of the formation of larger crystallites.

Several reports have suggested that the methanation reaction is a structure sensitive reaction. Crystallite size has an effect on the mass specific activity: as crystallite size decreases, the activity increases. There exists, however, a critical size below which the activity begins to decrease.

2.5. Catalyst deactivation

Catalyst deactivation is a major problem associated with the field of heterogeneous catalysis. It relates to the loss of activity with time-on-stream, a process that can be of a chemical or physical nature (Forzatti & Lietti, 1999). Bartholomew (2001), in a review on the mechanisms of catalyst deactivation, describes catalyst deactivation

as the loss over time of catalyst activity and/or selectivity. Although this deactivation is unavoidable, there are some mitigating steps which can be taken in order to minimise, postpone or even reverse this process. This then requires an understanding of the mechanisms of catalyst deactivation.

There are a number of different mechanisms through which a catalyst can deactivate.These deativation mechanisms are classed either as poisoning, coking or fouling, sintering and phase transformation. Catalyst deactivation may also occur via masking and loss of the active elements through volatilization, erosion and attrition (Forzatti & Lietti, 1999). Bartholomew (2001) separates the different mechanims of catalyst deactivation into six instrinsic mechanisms: poisoning, fouling, thermal degradation, vapour compound formation accompanied by transport, vapour-solid and/or solid-solid reactions, and attrition or crushing. These mechanisms could further be classed as chemical, mechanical or thermal. These deactivation mechanisms will be discussed below, particularly the effect these deactivation mechanisms have on the nickel catalyst systems employed in the methanation process.

2.5.1. Poisoning

Poisoning can be described as the loss of activity due to the strong chemisorption of impurities onto the active sites of the catalyst (Forzatti & Lietti, 1999). A poison may have a geometric effect in that it blocks an active site, or it may have an electronic effect by changing the adsorptivity of other species (Forzatti & Lietti, 1999). The chemical nature of the active sites of a catalyst may also be altered by a poison which could lead to the formation of new compounds, resulting in a change in the performance of the catalyst.

Sulphur compounds act as poisons of nickel catalysts in many catalytic processes, including methanation of synthesis gas (Bartholomew, *et al*. 1979). A number of authors including Bartholomew, *et al*. (1979), Erekson & Bartholomew (1983) and Fitzharris, *et al*. (1982) investigated the effects of sulphur poisoning on nickel methanation catalysts. Bartholomew, *et al*. (1979) conducted *in situ* activity studies

on alumina supported nickel catalysts in order to determine the effects of hydrogen sulphide on the methanation activity and found that the adsorption of hydrogen sulphide is affected by the competitive adsorption of reactants and reactant intermediates as well as residence time and temperature. Erekson & Bartholomew (1983) indicated that poisoning rates are complex functions dependent on hydrogen sulphide concentrations, temperature and partial pressures of carbon monoxide and water. Fitzharris, *et al*. (1982) highlighted the fact that sulphur as a poison has a geometric effect, resulting in the blockage of active sites, as opposed to electronic effects.

2.5.2. Fouling, coking and carbon deposition

Fouling is a mechanical deactivation mechanism characterised by the physical deposition of compounds from the fluid phase onto the catalyst surface, leading to a decrease in activity because of a blockage of sites or pores (Bartholomew, 2001). It refers to all occurrences where the catalytic surface is covered with a deposit (Moulijn, *et al*., 2001).When catalytic reactions involve hydrocarbons, side reactions may take place on the catalysts surface resulting in the formation of carbonaceous material which physically covers the active surface. This may result in the coverage of the active sites and pore blockage, as depicted in Figure 2.3, leading to catalyst deactivation (Forzatti & Lietti, 1999).

The mechanical deposition of carbon or coke is of particular importance in the methanation reaction. A distinction is made between coke and carbon and this is related to their origin (Bartholomew, 2001). Coke is the result of the decomposition or condensation of hydrocarbons whilst carbon is as a consequence of the disproportionation of carbon monoxide (Forzatti & Lietti, 1999).

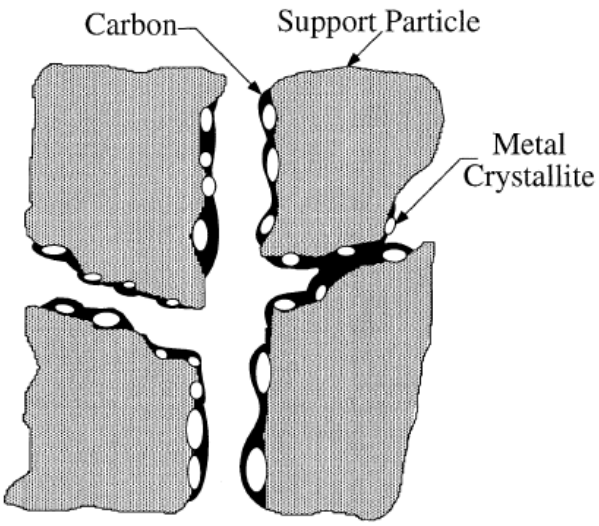

Figure 2.3. Conceptual model of fouling, crystallite encapsulation and pore plugging of a supported metal catalyst due to carbon deposition

Adapted from Bartholomew (2001)

McCarthy & Wise (1979) found that four types of carbon form on an alumina supported nickel methanation catalyst when exposed to carbon monoxide: chemisorbed carbon atoms (α), bulk nickel carbide, amorphous carbon (β), and crystalline elemental carbon.

Trimm (1983) compiled a review which focused on minimising coke deposition on supported metal catalysts. Trimm (1983) notes that the deposition of coke on a catalyst involves a multifaceted relationship between coke formation (resulting from reactions in the gas phase or on the catalyst surface), and coke removal.

2.5.3. Sintering

Thermal degradation results in a physical change in a catalyst leading to its deactivation. This deactivation can be as a consequence of the loss of catalytic surface area as a result of crystallite growth of the catalytic phase. Thermally induced deactivation can also lead to support collapse and subsequent loss of

support surface area and chemical transformation of the catalytic phase to a non-active phase as described in Section 2.5.4 (Bartholomew, 2001).

Sintering is the loss of active surface area as a consequence of the structural modification of the catalyst (Forzatti & Lietti, 1999) and is a major route for the deactivation of heterogenous catalysts which operate at elevated temperatures (Datye, *et al*., 2006).

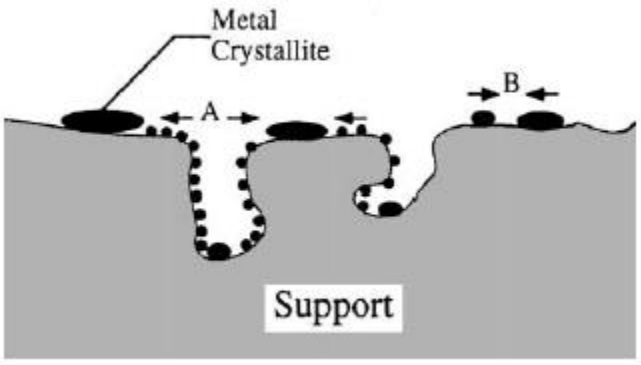

Figure 2.4. Two conceptual models for crystallite growth due to sintering by (A) atomic migration or (B) crystallite migration

Adapted from Bartholomew (2001)

There are two proposed pathways through which this sintering process may occur: atomic migration and crystallite migration (Figure 2.4). Atomic migration (Ostwald ripening) refers to sintering which occurs as a result of the escape of metal atoms from a crystallite, transport of these atoms across the support surface (or in the gas phase) and the resultant merger with another metal crystallite on collision. It is based on the assumption that the metal particles are immobile and sintering occurs due to the transfer of atoms or clusters from small particles to larger particles. Given that larger crystallites are more stable, the smaller crystallites decrease in size in favour of the larger ones increasing (Forzatti & Lietti, 1999). The second model, crystallite migration, involves the movement of crystallites across the support surface, resulting in their collision and coalescence. In order to determine ways of improving catalyst durability, it becomes important to gain an understanding of this sintering phenomenon (Datye, *et al*., 2006).

The melting point plays an important role in the sintering process (Moulijn, *et al*., 2001). The Tamman and Huttig temperatures, which are directly related to melting temperature, may give an indication as to the temperatures where thermally induced sintering may take place. These temperatures may be expressed according to the semi-empirical equations Equation 5 and Equation 6.

$$T_{Huttig} = 0.3 \cdot T_{melting}$$ Equation 5

$$T_{Tamman} = 0.5 \cdot T_{melting}$$ Equation 6

When the temperature increases, the mobility of atoms also increases. At the Huttig temperature, the atoms at the defects will become mobile. At the Tamman temperature, atoms from the bulk will begin to migrate. At the melting temperature, liquid-phase behaviour will be observed. However, a number of different factors influence the temperature at which mobility is observed in solids including texture, size and morphology. Furthermore, small particles may exhibit mobility at temperatures lower than the Tamman and Huttig temperatures (Couchman & Jesser, 1977).

Table 2.1. $T_{melting}$, T_{Tamman} and T_{Huttig} values (°C) of Ni, NiO and Al_2O_3

Compound	$T_{melting}$	T_{Tamman}	T_{Huttig}
Ni	1452	726	436
NiO	1955	978	587
Al_2O_3	2045	1023	614

A number of authors have investigated the sintering behaviour of nickel catalysts, attempting to determine the effects of time, temperature (Bartholomew & Sorensen 1983; Rostrup-Nielsen, *et al*., 2007; Shen, *et al*., 1981), support material (Rasmussen, *et al*., 2004; Richardson & Propp, 1986) and combinations thereof (Richardson & Crump, 1979). Some authors also attempted to determine whether size distributions could be used in order to identify the sintering mechanism (Datye, *et al*., 2006).

Bartholomew & Sorensen (1983) examined the sintering kinetics of silica and alumina supported nickel catalysts, with particle sizes in the 2 – 4 nm size range, prepared using a simple impregnation technique. The catalysts were exposed to elevated temperatures for different times in a hydrogen atmosphere. The work presented by Bartholomew & Sorensen (1983) indicates that the loss of metal surface area increases significantly with increasing temperature. It was hypothesised that at temperatures below 650 °C, although the growth of metal crystallites may contribute to a loss of the nickel surface area, it is primarily due to support collapse. Crystallite growth becomes the dominant mechanism of deactivation only beyond 650 °C. Bartholomew & Sorensen (1983) suggest that at temperatures below 650 °C and exposure times ranging between 5 and 20 hours, crystallite migration is the principal sintering mechanism. At higher temperatures and longer exposure times, there is a shift in the sintering mechanism to atomic migration. Bartholomew & Sorensen (1983), did not extend the study to nickel catalysts with larger crystallite size.

Shen, *et al*. (1981) found that at elevated temperatures, sintering of the metal takes place via atom migration. Similarly, Rostrup-Nielsen, *et al*., (2007) concluded that at 600 °C, sintering followed the atom migration sintering mechanism.

Rasmussen, *et al*. (2004) conducted a sintering study on alumina supported nickel catalysts. They exposed model catalysts prepared by impregnation to a 1:1 mixture of steam and hydrogen at different temperatures and ambient pressure for 50 hours. By considering the form of the nickel particle size distributions and the reaction order of loss of nickel surface area, Rasmussen, *et al*. (2004) concluded that sintering at 650 °C occurs through the particle coalescence mechanism.

Steam may exacerbate sintering by causing support sintering where the support forms mobile surface hydroxyl groups that are volatilized at elevated temperatures (Bartholomew, 2001). Also, Sehested, *et al*. (2004) and Sehested, *et al*. (2006) who conducted studies on nickel based catalysts under various P_{H_2O}/P_{H_2} ratios, propose that surface oxidation of the metal surface in H_2O/H_2 atmospheres results in the formation of a Ni_2-OH complex which enhances particle mobility, resulting in an increase in the sintering rate. The support is also susceptible to morphological and

structural changes which may then precipitate the sintering of the nickel particles facilitated by the collapse of the support pore structure (Rasmussen, *et al*., 2004). Williams, *et al*. (1972) studied the sintering behaviour of alumina supported nickel catalysts in a steam and hydrogen environment at elevated pressures by determing the loss of nickel specific surface areas. The catalyst was prepared by co-precipitation. Williams, *et al*. (1972) proposed that loss of nickel surface occurs as a result of the loss of fine pore structure and conversion of γ-alumina to α-alumina. The authors assert that the principle cause of sintering in this atmosphere is the thermal instability of the alumina base. The extent of sintering increases with an increase in the steam content of the treatment atmosphere.

Richardson & Propp (1986) investigated the effects of pore size on sintering kinetics of nickel on alumina catalysts using *in situ* magnetization techniques and hydrogen chemisorption measurements. Different alumina samples with varying average pore radii were used. It was observed that initial sintering rates increased as pore size increased, with decreased sintering rate in samples where the pore size approached the size of the crystallite.Richardson & Crump (1979) also acknowledge that pore size distribution may also play an important role in the sintering process and may account for the bimodal distributions observed at high temperatures.

Richardson & Crump (1979) investigated sintering of nickel on silica catalysts. Magnetic methods were used in order to determine the effects of temperature, time, initial distribution, and nickel concentration on crystallite size distribution in an attempt to determine the prevailing sintering mechanisms. Measurements were made *in situ*in helium. The fresh samples had nickel crystallites with sizes between 1 and 3 nm. At temperatures of 400 °C, the distribution widened. Richardson & Crump (1979) suggested that this result was consistent with the interparticle transport mechanism. Above 450 °C, however, more dramatic sintering was observed, with the migration model favoured as the sintering mechanism resulting in bimodal distributions. Richardson & Crump (1979) place great significance on initial changes in size distribution. The broadening of the distribution suggests the dominance of the interparticle transport mechanism as smaller crystallites disappear in the formation of larger ones. The crystallite migration model would be characterised by an increase in the average crystallite size with the disappearance of the small crystallites. The use of size distribution in the determination of sintering mechanism is highly ambiguous.

Datye, *et al*. (2006) conducted a study where they attempted to determine wheher the partcle size distribution of supported metal catalysts treated at 900 °C over time could be used to determine the sintering mechanism. Datye, *et al*. (2006) proposed that size distributions skewed towards small particles may indicate Ostwald ripening, whilst a size distribution with a long tail towards large particles may be characteristic of particle migration and coalescence. Their work could, however, not definitively establish a link between size distribution and the sintering mechanism.

2.5.4. Phase Transformation

2.5.4.1. Vapour compound formation accomponied by transport

The loss of metal through the formation of volatile compounds may result in significant catalyst deactivation.

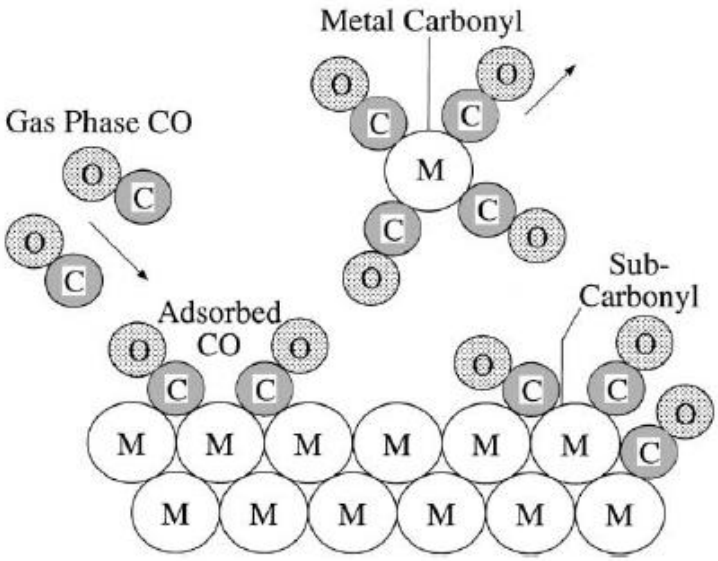

Figure 2.5. Formation of volatile tetra-nickel carbonyl at the surface of nickel crystallites in a CO atmosphere

Adapted from Bartholomew (2001)

The pathway by which sintering occurs during the hydrogenation of CO on nickel catalysts is dependent on the temperature. At low temperatures, the primary mechanism through which the catalyst deactivates is by the formation of volatile nickel carbonyls (Figure 2.5). At higher temperatures, atoms (or small agglomerates) migrate from one particle to another (Jensen, *et al*., 2011).

Van Meerten, *et al*. (1983) made use of magnetic measurements conducted during the hydrogenation of CO in order to detail how, at temperatures between 197 and 247 °C, small crystallites are lost in favour of larger particles through a process of Ostwald ripening, that is crystallite growth due to atomic migration. High CO partial pressures and lower temperatures favour the rate of transition of nickel, suggesting that nickel tetra carbonyl is the intermediate responsible for nickel transport. This finding was corroborated by Enger & Holmen (2012). They reported that nickel forms volatile carbonyls which result in a continuous loss of the metal from the reactor at temperature and pressure conditions of 200 - 300 °C and 10 - 60 bar, respectively. Similar findings were reported by Shen, *et al*. (1981) who investigated the loss of methanation activity of alumina-supported nickel catalysts at pressures of up to 6 bar and temperatures from 127 to 467 °C. The supported catalysts were prepared using the incipient wetness impregnation method. They concluded that at low temperatures the interparticle transport model involves volatile nickel carbonyl formation.

Munnik, *et al*. (2014) investigated the deactivation of silica supported nickel catalysts during the methanation reaction (230 °C, H_2:CO = 2:1, 1 bar). Ostwald ripening was the deactivation mechanism of interest, particularly the formation of nickel carbonyls. Munnik, *et al*. (2014) researched the effect of particle size (3 – 9 nm) and spatial distribution on this deactivation process. They reported that small particles (3 – 4 nm) deactivated faster and to a larger extent. There was also local destruction of the support. This all contributed to decreased catalyst stability. Medium sized particles (8 nm) displayed improved stability.

2.5.4.2. Solid state reactions

Forzatti & Lietti (1999) describe phase transformation as a process which takes place at very high temperatures and results in the transformation of one crystalline phase into a different one leading to significantly reduced activity. In alumina supported nickel catalysts, the alumina may diffuse to the surface of the catalyst, inducing the formation of an aluminate. This process may be exacerbated by the presence of gas phase oxygen and/or water (Bartholomew, 2001).

From the above investigations it can be noted that although a large amount of work has been done on the effects of temperature and steam on the sintering of nickel catalysts, there has not been an extensive study which deconvolutes and compares these two effects on crystallite size growth. The above studies were also limited in that all of them exposed a catalyst to a single temperature for an extended period of time and then characterised the sintered sample. No studies were conducted investigating nickel crystallite growth of a single catalyst over a range of temperatures. Furthermore, the above studies focussed on catalysts with a single crystallite size. The investigations were not extended to include various crystallite sizes.

2.6. The microemulsion technique

When considering a study which involves the investigation of the effects of crystallite size, it becomes crucial to be able to synthesise model catalysts with crystallite sizes in the nanometre range and with a very narrow size distribution (Fischer, *et al*., 2011). This then necessitates the investigation of techniques which would allow for the synthesis of unsupported and supported metal nanoparticles which display the required narrow size distribution as model catalyst systems.

Hada, *et al*. (2013) have highlighted a number of different techniques which have been proposed in the synthesis of nickel oxide nanoparticles including ultrasonic radiation, hydrothermal synthesis, the carbonyl method, the laser chemical method, pyrolysis by microwave, the sol-gel method, precipitation-calcinations, the

microemulsion method, anodic and plasma method and the thermal decomposition method. However, when considering a technique which could be used in the synthesis of metal or metal oxide nanoparticles in the nanometer size range and with a narrow size distribution, the microemulsion technique is most appropriate. The microemulsion technique is a soft technique which does not require extreme temperatures or pressures and is an effective means to synthesise metal or metal oxide crystallites in this nanometre size range (Han, *et al*., 2004).

According to Eastoe, *et al*. (2006), there are five main parameters which could influence particle size and polydispersity: solvent type, choice of surfactant or co-surfactant, addition of electrolyte, concentration of reagents, and water/surfactant ratio.

Boutonnet, *et al*. (1982) note that the preparation of extremely small particles of platinum, iron and nickel has gained particular attention due to the widespread use of these metals in heterogeneous catalysis. Small particles have been observed to have very large specific surface areas and a large proportion of crystalline faces or edges with specific catalytic properties, all of which is highly desirable in a heterogeneous catalyst. The preparation of such particles then requires that they be produced with uniform size and shape.

Eriksson, *et al*. (2004) highlight various advantages of the microemulsion technique for catalysts preparation, the most pertinant to this study being:

- A narrow size distribution can be obtained
- Particle size can be controlled to a large extent
- The support does not have a negative impact on the formation of the particles

Microemulsions have a number of applications ranging from oil recovery to the preparation of nanoparticles (Eriksson, *et al*., 2004). Industrially, metal catalysts are primarily prepared using the impregnation technique. This technique is successful in synthesising small metal particles, however it proves extremely difficult to also achieve a narrow size distribution. The microemulsion technique overcomes this limitation of the impregnation technique in that the reverse micelles, which are present in the microemulsion acting as nano-reactors or templates, create a suitable environment for the production of small metal nanoparticles of narrow size

distribution is created (Eriksson, *et al*., 2004). Song & Kim (1999) utilised the microemulsion technique and a conventional precipitation method to prepare tin oxide particles. They found that use of the microemulsion method resulted in the synthesis of particles with a smaller diameter and greater surface area than that observed when using the precipitation method. They reasoned that the distinguishing factor may be that the powder prepared by the microemulsion technique is formed in a controlled manner, confined to nanosize domains whilst in the precipitation method, the powder formed in an uncontrolled manner where the precipitated particles could grow and aggregate.

The term 'microemulsion' has been described by Danielsson & Lindman (1981) as a thermodynamically stable, optically isotropic solution of water, organic compound and at least one surfactant. According to Eriksson, *et al*. (2004), the microemulsion is heterogenous on a molecular level yet appears homogenous at a macroscopic scale. The internal structure of a microemulsion, at a particular temperature, is dependent on the ratio of its constituents. The system of particular interest is that involving water pools surrounded by surfactant and dispersed in the oil phase resulting in an inverted micelle. Transition metal salts can be dissolved in the water pool and serve as a precursor for final metal particles (Eriksson, *et al*., 2004; Boutonnet, *et al*., 1982).

A microemulsion which consists of small oil droplets in a continuous water phase (micelles) is consistent with a high concentration of water. Conversely a high oil concentration results in the formation of small water droplets in a continuous oil phase (reverse micelle) (Eriksson, *et al*., 2004). Pileni (1993) describes these reverse micelles as the result of a surfactant dissolved in organic solvent which then forms spheroidal aggregates. According to Pileni (1993), reverse micelles act as microreactors. The preparation of nanoparticles from microemulsions can be achieved by mixing a microemulsion containing the precursor with a microemulsion containing a precipitating agent (Eriksson, *et al*., 2004; Fischer, *et al*., 2011; Barkhuizen, *et al*., 2006; Mabaso, 2005) (see Figure 2.6 below).

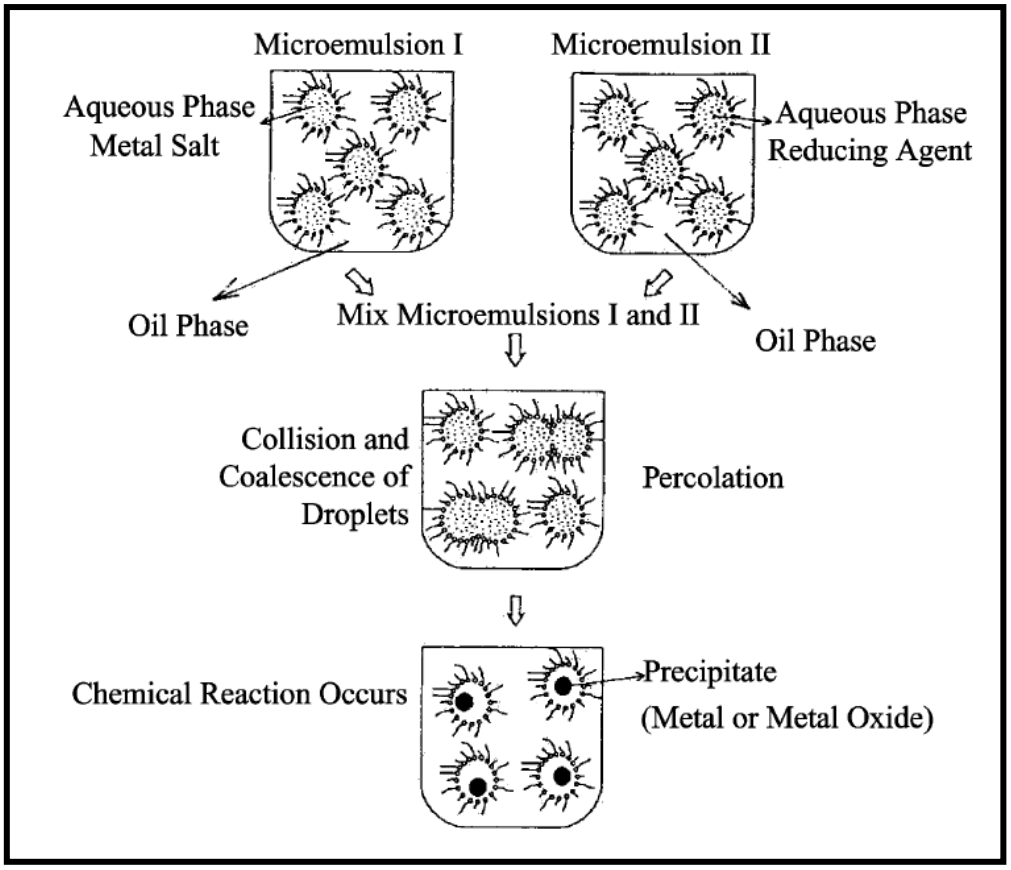

Figure 2.6: Proposed mechanism for the formation of metal particles by the microemulsion approach

Adapted from (Capek, 2004)

The size of the final metal particle is dependent on the size of the droplets in the microemulsion which may be manipulated by varying the water/surfactant ratio. Increasing this ratio results in an increase in the average diameter of the droplets (Eriksson, *et al*., 2004; Pileni, 1993; Mabaso, 2005).This property favours the synthesis of nanosize, monodispersed crystallites (Pileni, 1993).

2.6.1. Preparation of unsupported NiO nanoparticles

A number of authors have utilised the reverse micelle technique in the synthesis of nickel oxide nanoparticles. Ahmad, *et al*. (2006) used the reverse micelle technique to synthesise homogenous, spherical nickel oxide nanoparticles of 25 nm with a narrow size distribution. These partcles were characterised using transmission

electron microscopy (TEM), powder X-ray diffraction (PXRD) and Fourier transform infrared spectroscopy (FTIR) was used in order to confirm the crystalline nature of the material. Ahmad, *et al*. (2006), however, did not indicate whether this technique could be used in the synthesis of nanoparticles of different sizes.

Du, *et al*. (2012) applied the water-in-oil microemulsion technique in the synthesis of nanosized nickel oxide particles. They successfully synthesised nanoparticles in the 11.5 nm to 31.5 nm range by varying the proportion of surfactant, oil and water in the microemulsion, the mixing method and the calcination temperature. They however failed to deconvolute the contribution of each factor in controlling crystallite size and so no clear correlation was seen between varying the water/surfactant ratio and resultant nanoparticle size.

Mihaly, *et al*. (2011) also made use of the microemulsion technique in an attempt to control the particle size, morphology and size distribution of the nickel oxides. The authors successfully synthesised nanoparticles with an average size of 11 nm with a very narrow size distribution. They, however, did not determine whether this technique could be applied over a wide range of sizes.

Hada, *et al*. (2013) made use of a single microemulsion system where a unique blend of anionic and non-ionic surfactant. The blend was proposed to be more rigid than a single moiety of ionic surfactant which they hoped would result in improved size control as the rigidity of the surfactant layer has been highlighted as an essential factor in size control. Although these authors did synthesise nickel oxide particles, they merely reported that particles in the range of 14 nm to 50 nm were synthesised. No size distribution of the sample was determined. No conclusions could be made on whether this single microemulsion technique using a unique surfactant blend could successfully be used to synthesise nanoparticles with a narrow size distribution. They also failed to synthesise particles of different sizes, and so no information could be gained on whether increasing the rigidity of the surfactant layer could indeed be a possible route for increased partcle size control.

2.6.2. Preparation of supported NiO nanoparticles

When considering catalyst preparation methods, precipitation is the most widely used technique for the synthesis of both monometallic and multimettallic oxides (Schwarz, *et al*., 1995). This process results in the formation of a new solid phase (precipitate) from a homogenous liquid solution (Schwarz, *et al*., 1995). Impregnation, which includes the use of aqueous media, involves the addition of a specific volume of solution containing the precursor of the active metal of the catalyst with the carrier. Incipient wetness is a term applied to the special case of impregnation where the volume of the solution added is equal to or less than the pore volume of the solid support. Although nickel catalysts are conventionally synthesised using the impregnation or precipitation method, a technique which results in the formation of catalysts with particles in the nanometre size range and with a very narrow size distribution was required in order to successfully conduct an investigation involving crystallite size effects. Thus, the application of the microemulsion technique in the synthesis of supported nickel nanoparticles was considered.

Supported nanoparticles could also be synthesised using the reverse micelle technique. Boutonnet, *et al*.(1982) suggested that when stable dispersions are formed, the particles could be transferred to solid supports without agglomeration by evaporation of the solvent. Furthermore, Eriksson, *et al*.(2004) note that in order to prepare a homogenous supported catalyst, it is imperative that a homegenous distribution is maintained when transferring the particle onto the support. Simultaneously adding the support powder and the solvent may result in the particles adhering to the support, obtaining a homogenous distribution of the particles. This is, however, highly dependent on the properties of the support (Eriksson, *et al*., 2004). There are number of different ways to support nanoparticles using the microemulsion technique. In order to obtain homogenous distribution of the metal particles on the carrier, the support could be co-precipitated during the destabilisation of the reverse micelles (Kishida & Teranishi, 1968).The disadvantage associated with this method involves the possible encapsulation of the metal, decreasing the catalytically active surface area. The support could also be added directly to the microemulsion (Barkhuizen, *et al*., 2006; Cheang, 2009; Mabaso, 2005). Cheang (2009) and

Mabaso (2005) proved this method successful for the synthesis of model iron catalysts whilst Barkhuizen, *et al*. (2006) utilised the method for the successful synthesis of γ-alumina supported ruthenium and silica supported cobalt. However, Fischer (2011), whose investigation involved the synthesis of model cobalt catalysts for Fischer-Tropsch synthesis, observed that the addition of the support material to the mircoemulsion results in the formation of cobal aluminates, causing a decrease in the reducibility of the catalyst. An alternative would be to dry and resuspend the nanoparticles synthesised using the microemulsion techniqueand then deposit tem on the support (Fischer, *et al*., 2011).

3. Scope of study

The methanation reaction is a highly exothermic reaction and the nickel catalyst may be exposed to a range of different temperatures during operation. The sintering of nickel methanation catalysts is a relatively well studied phenomenon. A number of authors have investigated the thermal degradation of nickel catalysts over time at different temperatures and in different atmospheres. However, these studies were limited: catalyst characterisation could only be done on already sintered material and there was no continuous characterization of the catalyst during the sintering process over the range of temperatures associated with the methanation reaction, i.e. no *in situ* characterisation.

Also, nickel is pyrophoric, which implies that it can ignite spontaneously or react violently when exposed to air, resulting in a dramatic change in its physico-chemical properties. It has also been noted that the methanation reaction occurs at elevated pressures. It is then important to be able to conduct these sintering experiments at pressures relevant to these conditions. This increases the difficulty of its characterisation during experimental investigations. *In situ* characterisations may be used in order to allow for the investigation of changes of the catalyst structure/phase and its performance during the experimental process.

The main objective of this study was to investigate the effects of nickel crystallite size on thermally induced sintering using a unique *in situ* magnetometer, developed at the University of Cape Town. The sintering studies were conducted on γ-alumina supported nickel nanoparticles in an inert atmosphere and also in a steam and hydrogen atmosphere. It is expected that small crystallites will be more likely to sinter at elevated temperatures than larger crystallites. Water vapour will accelerate the sintering process for both small and larger crystallites.

When conducting size investigations, model catalysts are essential. In order to produce these model catalysts, the application of the microemulsion technique in the synthesis of nickel catalysts was investigated. This was achieved by the synthesis of

nickel nanoparticles in the 2 – 15 nm size range with a narrow size distribution. The microemulsion technique has been identified as a technique which allows for this crystallite size control. A number of parameters may have an influence on particle size, however the effects of varying the water/surfactant ratio in an attempt to synthesise nickel nanoparticles of different sizes has not as yet been well established. It is hypothesised that varying the water/surfactant ratio will allow for the synthesis of a range of nickel nanoparticles in the 2 – 15 nm size range with a very narrow size distribution.

Preparation of supported samples was then also required in order to conduct sintering studies on alumina supported nickel samples at temperatures ranging up 650 °C. This required an investigation into the different catalyst preparation methods associated with the microemulsion technique.

4. Research approach and methodology

The reverse micelle technique was used for the synthesis of the unsupported and supported material. Both the unsupported and the supported material was characterised using transmission electron microscopy (TEM) and powder X-ray diffraction (PXRD). Furthermore, the supported material was characterised using *in situ* PXRD and the *in situ* magnetometer. Brunauer–Emmett–Teller (BET) was used in order to characterise the support material. Outlined below is a comprehensive description of the techniques employed in the characterisation of the unsupported and supported material.

4.1. Synthesis of unsupported nickel oxide nanoparticles

The method for the preparation of nickel oxide nanoparticles of various sizes was as outlined by Mabaso (2005), who proved the method successful for the synthesis of iron oxide nanoparticles. The water-in-oil microemulsion system consisted of water as the polar phase, Berol 050 (Pentaethylene glycol dodecylether, Akzo Nobel) as the surfactant and n-hexane (AR grade, Kimix) as the oil phase. This ternary system is depicted in Figure 4.1. The stability region for this system was first introduced by Abrevaya & Targos (1987) and later confirmed by Mabaso (2005) who conducted a titration of Berol 050 and n-hexane mixtures with water in a thermostatic bath heated to 25 °C in order to determine the area where the ternary system was stable and optically transparent. Fischer (2011) also investigated the effect of temperature on the stability region of the reverse micelle by combining over 100 mictures of n-hexane, surfactant and water and equilibrating these mixtures in a temperature controlled batch at 10, 25 and 40 °C. Fischer (2011) reported that the stability region decreases with increasing temperature.

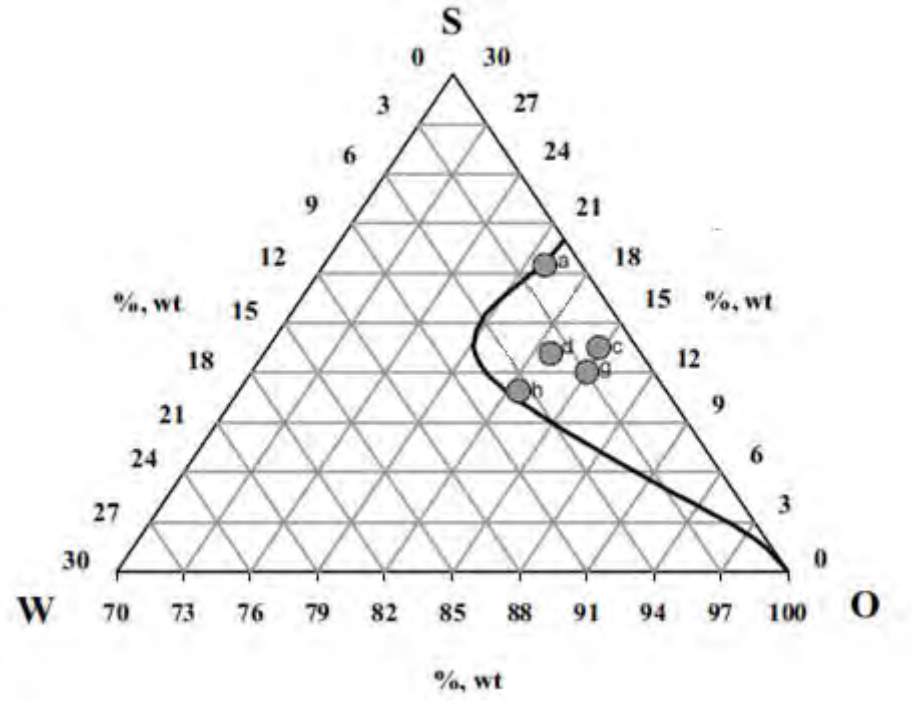

Figure 4.1. Ternary diagram of water-in-oil microemulsion system (W: water, O: oil (n-hexane), S: surfactant) with marked stability region with water/surfactant ratios (g/g) (a) 5:40 (c) 5:58 (d) 12:40 (g) 9:35 (h) 20:33

The water-in-oil microemulsion technique via precipitation of nickel hydroxide from aqueous nickel (II) nitrate hexahydrate ($Ni(NO_3)_2.6H_2O$,>97%,Sigma-Aldrich Inc.) with ammonium carbonate ($NH_4HCO_3.NH_2$, Merck Chemicals) was used to synthesise nickel oxide crystallites of different sizes. The salt solution concentration was kept constant at 0.5 M. In order to synthesise different crystallite sizes, the amount of the oil phase (n-hexane) was kept constant at 250 g and the water/surfactant ratio varied. Two identical microemulsions were prepared by mixing specific volumes of Berol 050 (outlined in Table 4.1) with n-hexane. These microemulsions were then allowed to equilibrate for 24 hours and then filtered to remove the white residue which formed. Thereafter, the required mass of an aqueous solution of nickel nitrate was added to one microemulsion and an aqueous solution of ammonium carbonate to the second microemulsion. A 4:1 molar ratio of $[(NH_4)_2CO_3]$: $[Ni^{2+}]$ was used in order to achieve complete precipitation of the 0.5 M nickel nitrate solution. The amounts used are recorded in Table 4.1.

Table 4.1. Water/surfactant ratios used to synthesise nickel oxide nanocrystallites of different sizes

Sample code	m_{oil} (g)	water/surfactant ratio (g/g)
A	250	5/40
C	250	5/58
D	250	12/40
G	250	9/35
H	250	20/33

The two microemulsions were mixed using a magnetic stirrer under a constant stirring speed of 800 rpm for three hours. Pileni (1993) postulated that the reverse micellar aggregates are subject to Brownian motion as a direct consequence of their small size. Consequently the droplets collide and coalesce, resulting in contact between the reactants which will then react and form a precipitate. The precipitate will remain confined to the interior of the microemulsion droplet. The microemulsions were blue in colour. There was a correlation between the colour of the microemulsion and the water/surfactant ratio: the higher the water/surfactant ratio, the darker the microemulsion. A nanoparticle-containing microemulsion is stable. In order to separate the particles from the constituents of the microemulsion a solvent needs to be added to compete with the surfactant molecules adsorbed onto the particle in order to destabilise the suspension (Eriksson, *et al*., 2004). For this system, acetone (AR grade, Kimix) acts as the destabilising agent. The precipitate was liberated from the liquid phase by flocculating with acetone followed by washing with acetone in order to remove the surfactant. Thereafter, the precipitate was dried at room temperature for three hours, then at 120 °C in an oven for 24 hours and finally calcined at 300 °C in a furnace for three hours, all in air.

A schematic representation of this experimental procedure is shown in Figure 4.2 below:

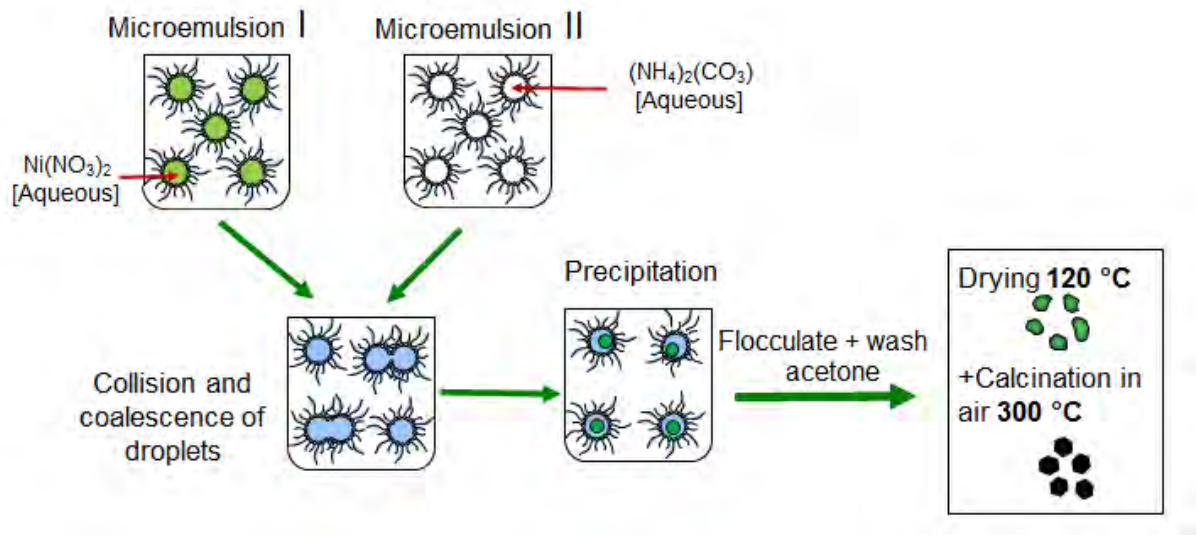

Figure 4.2: Schematic representation of synthesis of nickel nanocrystallites using a microemulsion via precipitation technique

4.2. Synthesis of supported nickel oxide nanoparticles

γ-alumina (Puralox SCCa 5-150, Sasol Technology) was the support material used in this study. The support was pre-treated prior to its use by calcining it at 450 °C in a furnace for 5 hours (heating rate: 10 °C/min). Thereafter it was stored in an oven at 120 °C. Two methods were used to synthesise supported nickel oxide nanoparticles: Method 1 as outlined by Mabaso (2005) and Method 2 as described by Fischer (2011).This then allowed for the determination of the most appropriate preparation method to synthesise model catalysts with a narrow size distribution and which display sufficient magnetic behaviour on reduction in order to be able to conduct an *in situ* magnetic study on the thermal degradation of nickel catalysts in an inert and steam and hydrogen atmosphere.

4.2.1. Synthesis of supported nickel oxide nanoparticles Method 1

The same procedure as outlined in Section 4.1 was used to prepare the supported nickel oxide nanoparticles. The only additional step was the addition of the alumina

support to the microemulsion before flocculation with acetone. A metal loading of 10 wt.% was targeted during the synthesis of the supported nickel oxide nanoparticles. Thereafter the sample was calcined in a fluidised bed reactor at 350 °C (heating rate: 10 °C/min) in argon (60 mL (NTP)/min/g_{cat}) for 16 hours. Figure 4.3 below is a graphical representation of the synthesis of supported nickel oxide nanocrystallites using Method 1.

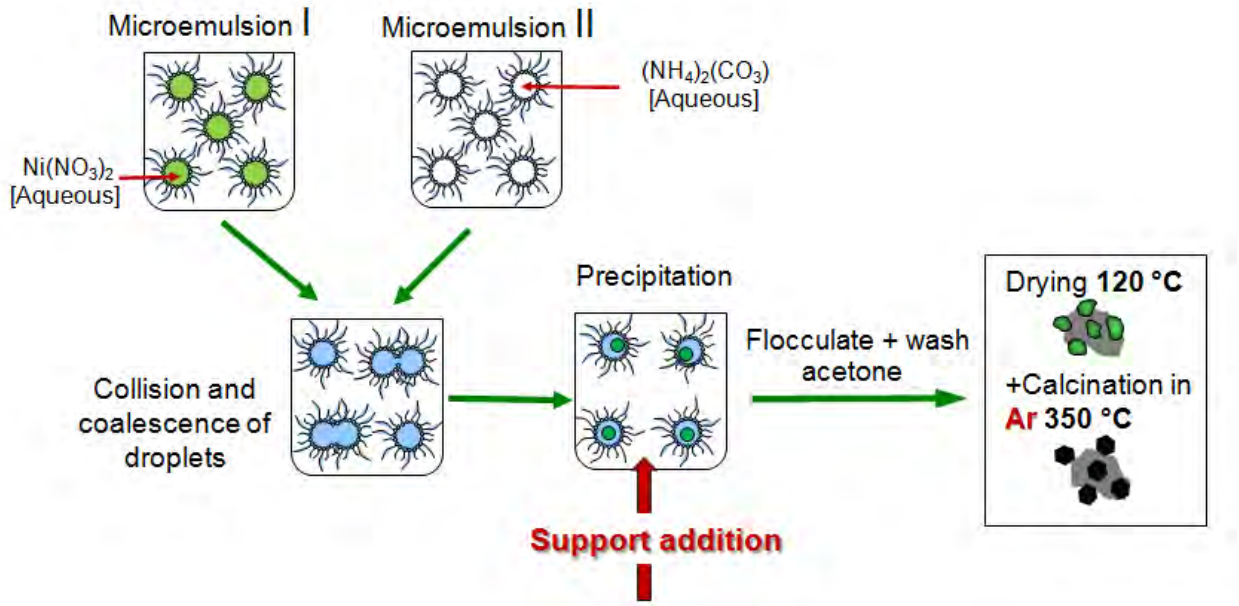

Figure 4.3: Schematic representation of synthesis of supported nickel nanocrystallites using a microemulsion technique

4.2.2. Synthesis of supported nickel oxide nanoparticles Method 2

In order to synthesis supported nickel oxide nanoparticles using Method 2 the procedure outlined in Section 4.1 above was used to first synthesise unsupported nickel oxide nanoparticles. These particles were resuspended in water by ultrasonicating the mixture with a sonication probe (Bandelin Sonoplus, 20 kHz, 200W) for one hour. The support material was then added to the suspension and the mixture was sonicated in an ultrasonic bath for one hour followed by stirring at 400 rpm overnight. The sample was then dried by gently heating at 100 °C with stirring in

three-necked round-bottomed flask placed in a silicon oil bath under an inert atmosphere of nitrogen. This procedure is illustrated in Figure 4.4.

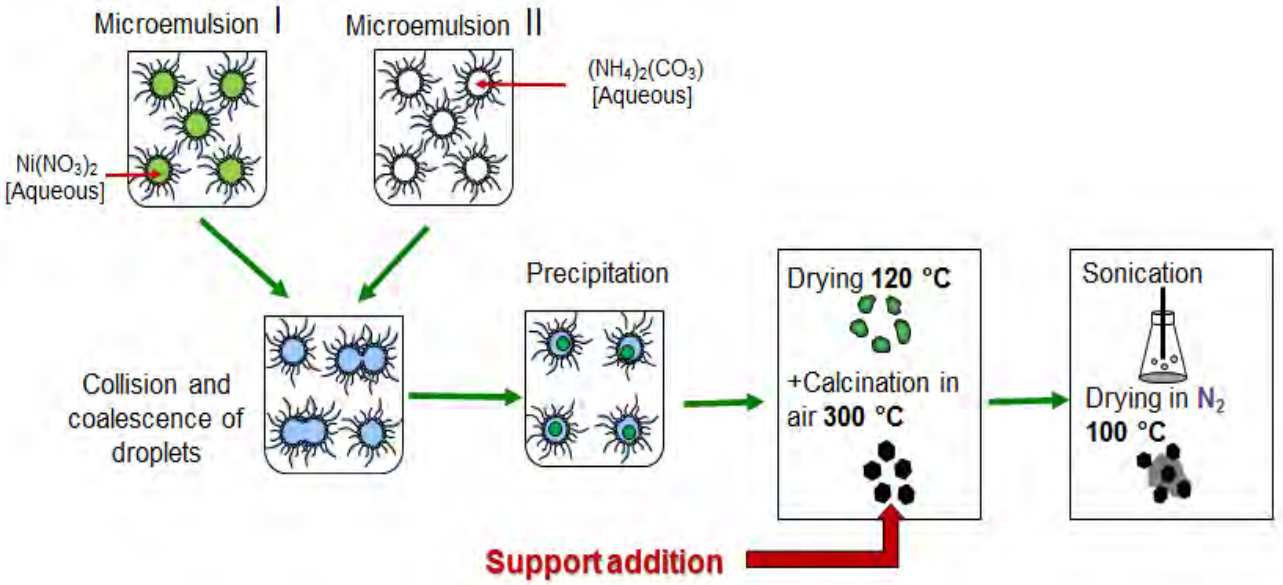

Figure 4.4: Schematic representation of synthesis of supported nickel nanocrystallites with support addition to NiO nanoparticles

4.3. Characterisation of nickel nanocrystallites and model catalysts

4.3.1. Transmission Electron Microscopy (TEM) and Scanning Transmission Microscopy (STEM)

In order to determine the morphology as well as size and size distribution of the nickel oxide nanoparticle samples synthesised by varying the water/surfactant ratio, Transmission Electron Microscopy (TEM) was used. For the supported material, TEM was also used to determine how well dispersed the nanoparticles were on the support. Acetone was first added to the powder sample under investigation and the mixture was sonicated in an ultrasonic bath for 10 minutes in order to obtain a suspension. A droplet of the suspension was then transferred on to a carbon coated copper grid. The grids were then allowed to air dry before analysis in a Tecnai F20 Transmission Electron Microscope operated at 200 kV.

Scanning Transmission Electron Microscopy (STEM) was also used to characterise the model catalysts after exposure to elevated temperatures and a steam in hydrogen atmosphere. This analysis was performed using a field emission FEI Tecnai F20 microscope, operated at 200 kV, and equipped with a high-angle annular dark-field (HAADF) detector for Z-contrast imaging. Before conducting any measurements, the powder samples under investigation were sonicated in ethanol and the suspension supported onto lacey carbon coated copper grids (SPI Supplies, 200 mesh).

The TEM and STEM micrographs were then analysed using the freeware ImageJ in order to obtain particle size distributions. An attempt was made to measure at least 300 particles in order to obtain statistically relevant size data. The results obtained were a number based average. A volume based average was, however, required in order to compare meaningfully the results obtained from TEM with those obtained from PXRD and magnetic readings, which report average crystallite size on a volume based average. In order to convert a number based average to a volume based average, Equation 7 was used:

$$\overline{d_p} = \frac{\Sigma n_i d_p^{\,4}}{\Sigma n_i d_p^{\,3}} \qquad \text{Equation 7}$$

4.3.2. Powder X-ray Diffraction (PXRD)

Powder X-ray Diffraction (PXRD) is a characterization tool which provides information which can be used to identify crystalline phases present in a powder sample, as well as average crystallite size. PXRD measurements were conducted on the unsupported and supported material using a Bruker D8 Advance X-ray diffractometer with a cobalt source (Co-K_α radiation of wavelength 1.79 Å) and a position sensitive detector (Bruker Vantec). The scan range was 20 ° < 2θ < 130 ° in the step-scan mode with a step-size of 0.01 ° and a scan rate of 0.025 °/s (scan time: 1 hour 13 minutes). In order to identify the different crystalline phases the peak positions as well as the relative intensities in the diffractograms were compared with the peak positions and relative intensities recorded in the ICDD database.

Rietveld refinement using TOPAS (Appendix C) was used to determine average crystallite size where a crystal structure and instrumental and microstructural information was utilised in order to generate a diffraction pattern which is then fit to the actual pattern by making use of a least squares method to minimize the differences. The fit of the calculated pattern can be improved by refining certain parameters. This technique also allows for a quantification of the phase compositions in the sample.

4.3.3. *In situ* Powder X-ray Diffraction Temperature Programmed Reduction (*In situ* PXRD TPR)

The reduction behaviour of the model catalysts was also investigated using *in situ* PXRD which allowed for the simulation of the precise reduction conditions the catalysts were exposed to during catalyst sintering tests. A novel *in situ* capillary cell, developed at the University of Cape Town (Fischer, *et al*., 2014), was used in this investigation and is depicted in Figure 4.5. The cell allows for the *in situ* determination of crystallite size changes taking place under the required reaction conditions. It has a maximum operating temperature and pressure of 500 °C and 25 bar respectively. The catalyst sample was placed into a Kapton capillary (3" long, OD = 0.0400", ID = 0.0360", wall = 0.00200", Cole-Parmer ®). Although use of the polyimide Kapton is limited to temperatures below 400 °C, it does not block X-rays thus making it highly suitable for use in PXRD studies. The capillary was inserted into the *in situ* XRD cell which was then mounted on to the Bruker D8 Advance X-ray diffractometer with a cobalt source (Co-K_{α} radiation of wavelength 1.79 Å). 400 ml/min/g_{cat} hydrogen was allowed to flow through the capillary which was heated to 380 °C (heating rate: 1 °C/min).The scan range was 40 ° < 2θ <80 ° (scan time: 16 minutes). Scans were recorded at 50 °C, 100 °C and then every 40 °C up to 380 °C. The temperature was kept constant for the duration of each scan.

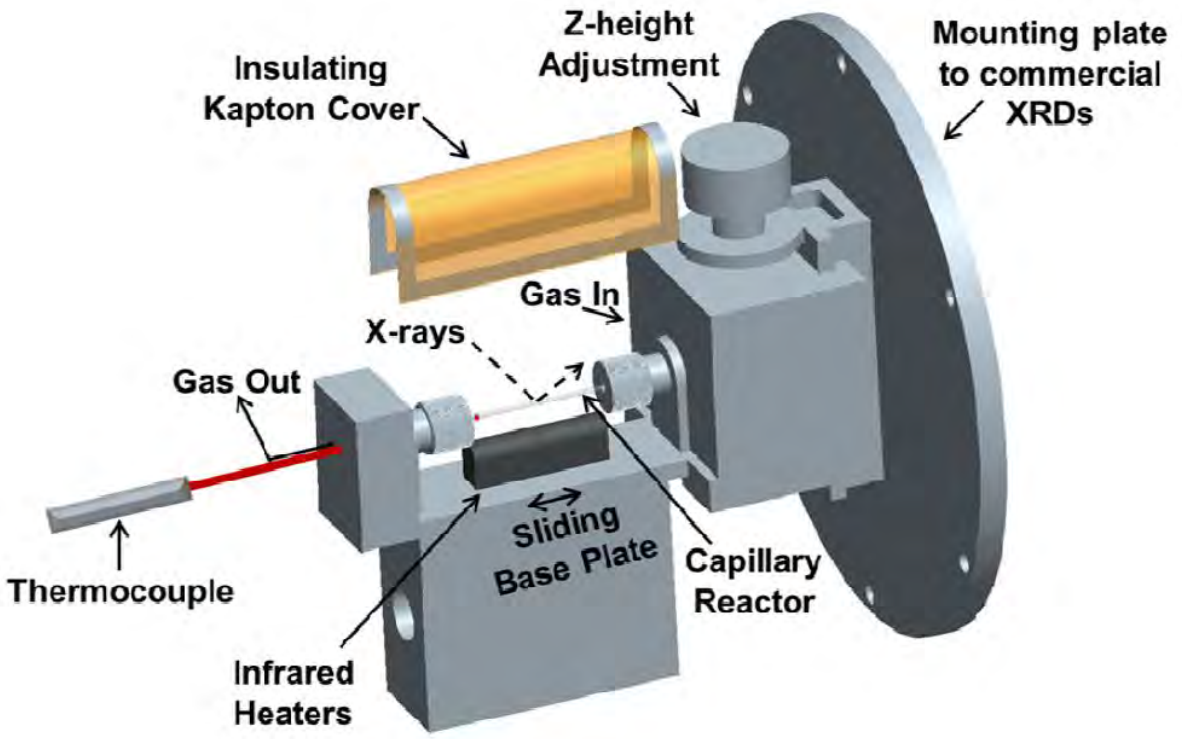

Figure 4.5. Design of the *in situ* capillary cell reactor

Adapted from Fischer, et al. (2014)

4.3.4. Temperature Programmed Reduction (TPR)

Temperature Programmed Reduction (TPR) was used to determine the reduction behaviour of the supported samples. The reduction was carried out in a U-type quartz reactor on a MicromeriticsAutoChem 2910 where a thermal conductivity detector (TCD) was used to measure hydrogen consumption. 100 mg of the supported sample was first dried by flowing argon (10 mL (NTP)/min) through the system and heating to 110 °C (heating rate: 10 °C/min) and holding for 60 minutes. The system was then cooled to 60 °C. 5 % hydrogen in argon (50 mL (NTP)/min) was allowed to flow through the sample and the system was heated to 900 °C (heating rate: 5 °C/min).

4.3.5. Atomic Absorption Spectroscopy (AAS)

In order to determine the metal loading of nickel on the γ-alumina, Atomic Absorption Spectroscopy (AAS) was used. The supported samples were digested in a mixture of acids (6 mL concentrated hydrochloric acid (HCl), 2 mL concentrated hydrofluoric acid (HF), 2 mL concentrated nitric acid (HNO_3)) on a MARS-5 Microwave digester. AAS analysis was then carried out on a VarianSpectraAA 110 instrument.

4.3.6. Brunauer–Emmett–Teller (BET)

Brunauer-Emmett-Teller (BET) analysis was conducted on the support material, γ-alumina, using a BET Micrometrics TriStar 3000 which makes use of the principles associated with physical adsorption and capillary condensation. The sample, which is placed in an evacuated tube, is first cooled to cryogenic temperature. The sample is then allowed to come into contact with nitrogen at a series of precisely controlled pressures. As the pressure increases, so too does the number of gas molecules adsorbed on the surface. The equilibrated pressure (P) and the saturation pressure (P_0) are determined in order to obtain the relative pressure ratio (P/P_0) which is then recorded, together with the quantity of gas adsorbed by the sample at each equilibrated pressure.

4.3.7. Magnetic measurements

Nickel is ferromagnetic. Hence, magnetic measurements can be used in order to study its behaviour. Measurement of the total magnetisation (M) of a catalyst sample can give insight into catalyst composition, crystallite size and size changes of the ferromagnetic fraction. According to Serway & Jewett, Jr. (2014), ferromagnetic materials have permanent atomic magnetic moments that have a tendency to align parallel to one another when placed in an external magnetic field (H). Once this alignment has taken place, the material remains magnetised even after the external

field is removed and this magnetisation is termed remnant magnetisation (M_r). This phenomenon is as a result of of the strong coupling between neighbouring moments. Ferromagnetic materials consist of microscopic regions termed domains, regions wherein all magnetic moments are aligned (Serway & Jewett, Jr., 2014). When the ferromagnetic sample is unmagnetised, the magnetic moments in the domains have a random orientation. This them implies that the net magnetic moment is zero.

The Curie temperature (T_C) is the critical temperature beyond which the ferromagnetic substance loses its residual magnetization. Below this Curie temperature, the magnetic moments of each domain are aligned and the substance will display ferromagnetic behaviour. Above the Curie temperature, thermal agitation becomes large enough to cause the randomisation of the magnetic moments and no magnetisation can be measured. The Curie temperature of nickel is 358 °C (Serway & Jewett, Jr., 2014).

Superparamagnetism, a special case of ferromagnetism usually in the nanometre regime where the crystallite size is below or at the size of the magnetic domain, is a term applied to crystallites which assume the behaviour of dipoles. In the presence of an external magnetic field, their magnetic moments align parallel to one another. However, on removal of the external field, the magnetic moments again assume a random orientation. The external field strength required for the alignment of superparagmagnetic material is strongly dependent on crystallite size. At low field strengths, the larger magnetic domains will align in the direction of the external field and the magnetisation observed will be mainly as a consequence of larger crystallites. At high field strengths, even the very small magnetic domains will align in the direction of the external field and the magnetisation will be as a result of the smallest crystallites. This trend is depicted in Figure 4.6. The saturation magnetisation (M_s) is the magnetisation at which the magnetic domains of all the crystallites align in the direction of the external field.

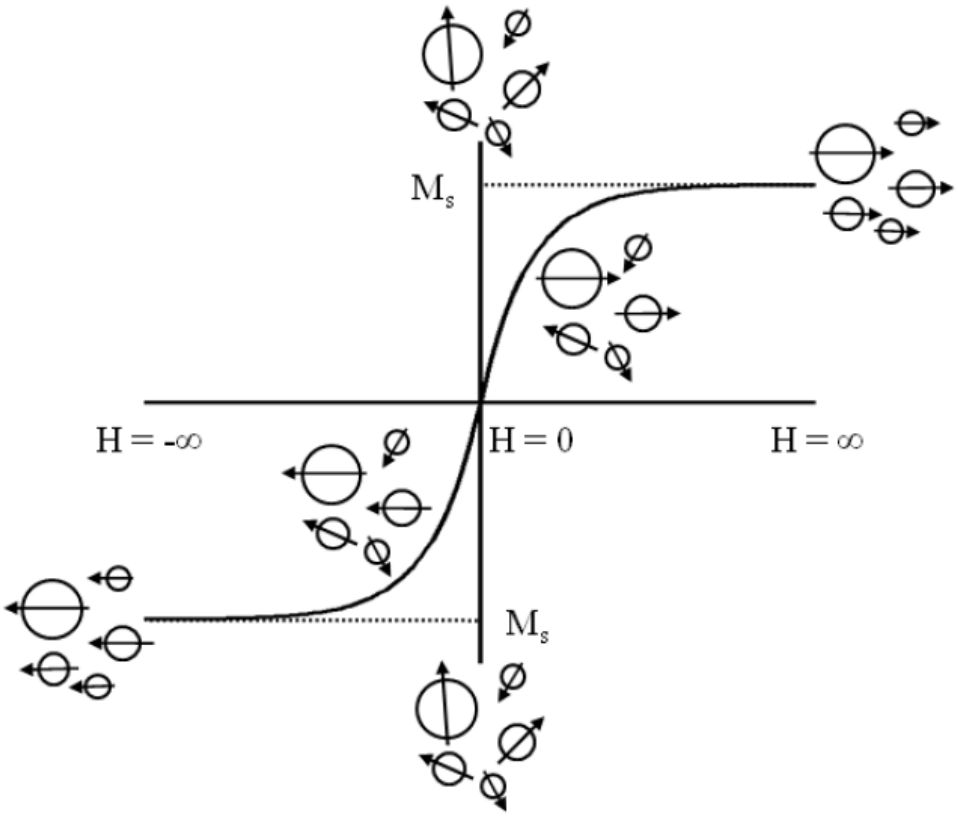

Figure 4.6. Schematic representation of the behaviour of superparamagnetic particles in an external magnetic field

Adapted from Dalmon (1994)

This phenomenon can be used in order to extract information about crystallite size from superparamagnetic samples. The Langevin function, expressed according to Equation 8, can be used in order to determine crystallite size at different temperatures.

$$\frac{M}{M_S} = \coth\left(\frac{\rho \cdot \sigma_S \cdot \frac{\pi}{6} \cdot d^3 \cdot H}{k \cdot T}\right) - \left(\frac{k \cdot T}{\rho \cdot \sigma_S \cdot \frac{\pi}{6} \cdot d^3 \cdot H}\right) \qquad \text{Equation 8}$$

$\frac{M}{M_S}$ is the ratio of sample magnetisation to saturation magnetisation, ρ is the density of the magnetic material, σ_s the mass specific magnetisation, d the crystallite diameter, H the external applied field, T the temperature and k Boltzmann constant. The

critical size of nickel, which is the diameter below which crystallites will exhibit superparamagnetic behaviour, is reported to be 55 nm (Chernavskii, *et al*., 2009).

An indication of crystallite size could also be obtained from the change in the percentage of ferromagnetic material (γ). It is described by Equation 9.

$$\gamma(wt\%) = \frac{2M_r}{M_S} \qquad \text{Equation 9}$$

where γ is the percentage of ferromagnetic material, M_r the remnant magnetisation and M_s the saturation magnetisation.

Paramagnetic materials have a weak magnetism. In the presence of an applied field, the atomic moments of paramagnetic materials line up with the field. However, this process is mitigated by thermal motion leading to magnet moments with random orientations (Serway & Jewett, Jr., 2014). NiO and the carrier, γ-Al_2O_3, exhibit paramagnetic behaviour.

Magnetic measurements were conducted in an *in situ* magnetometer developed at the University of Cape Town. The magnetometer (Figure 4.7) allows for the investigation of ferromagnetic catalyst samples at high temperatures of up to 650 °C, and pressures of up to 50 bar which in turn means that catalyst samples can be characterised *in situ* at industrially relevant conditions (Fischer, *et al*., 2014; Claeys, *et al*., 2010).

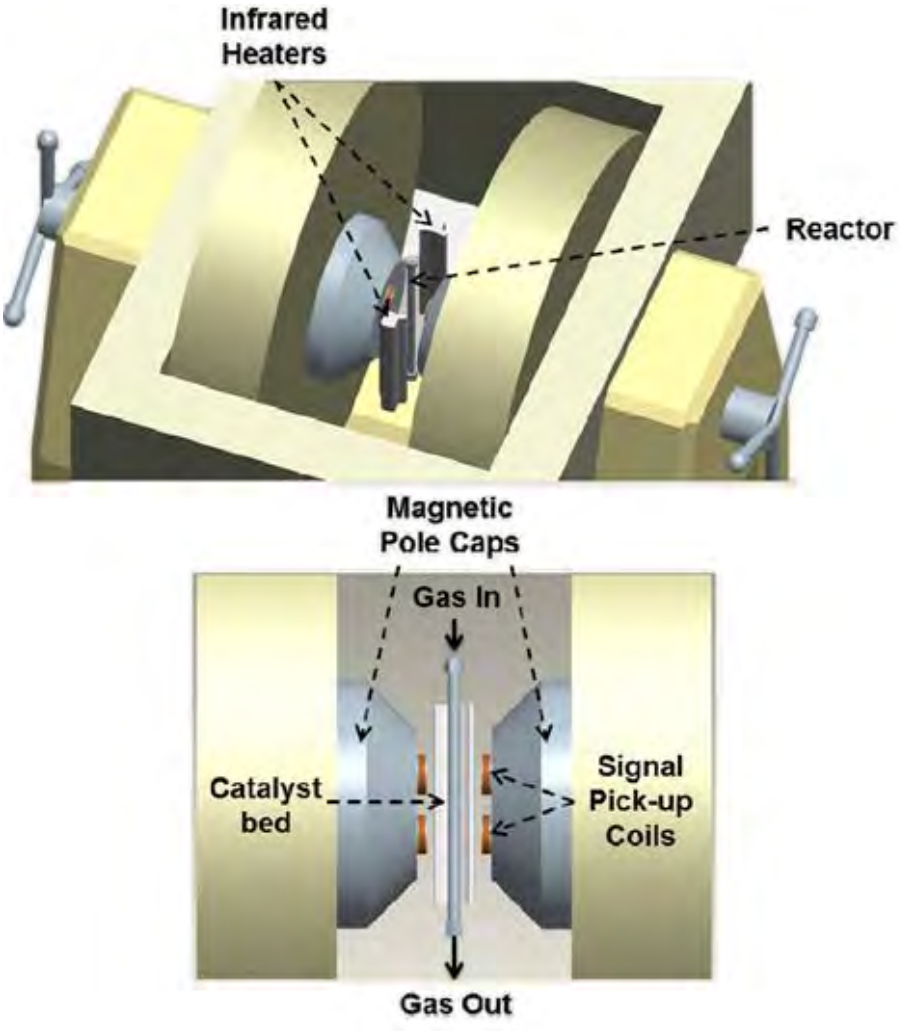

Figure 4.7. Design of *in situ* magnetometer with a maximum operating field of 20 kOe, maximum temperature of 650 °C and maximum pressure of 50 bar

Adapted from Fischer, et al. (2014)

4.3.7.1. Experimental set-up

Figure 4.8 is a schematic representation of the physical setup of the equipment used for the experiments conducted on the *in situ* magnetometer. The setup includes the *in situ* magnetometer configuration which is depicted in Figure 4.9. Gases are supplied from cylinders. During the sintering experiments, argon, hydrogen and carbon dioxide (for the passivation of the spent catalyst) were controlled using mass flow controllers MFC5, MFC3, MFC1 respectively. Gas flow to the reactor was

controlled using valves 3WV4 and 3WV5. An HPLC pump (P) supplied water to the water vaporizer through valve 3WV1 whilst gas flow to the water vaporizer was controlled using valves 3WV2 and 3WV3. The water from the water co-feeding sintering experiments was collected in the cold trap. The temperature of the water vaporizer as well as the lines was maintained at 180 °C. The back pressure regulator (BPR) was used to control the total pressure of the system: during the investigation of the effect of elevated temperatures on sintering, a system pressure of 1 bar was used. During exposure of the model catalysts to steam and hydrogen, the system pressure was maintained at 10 bar.

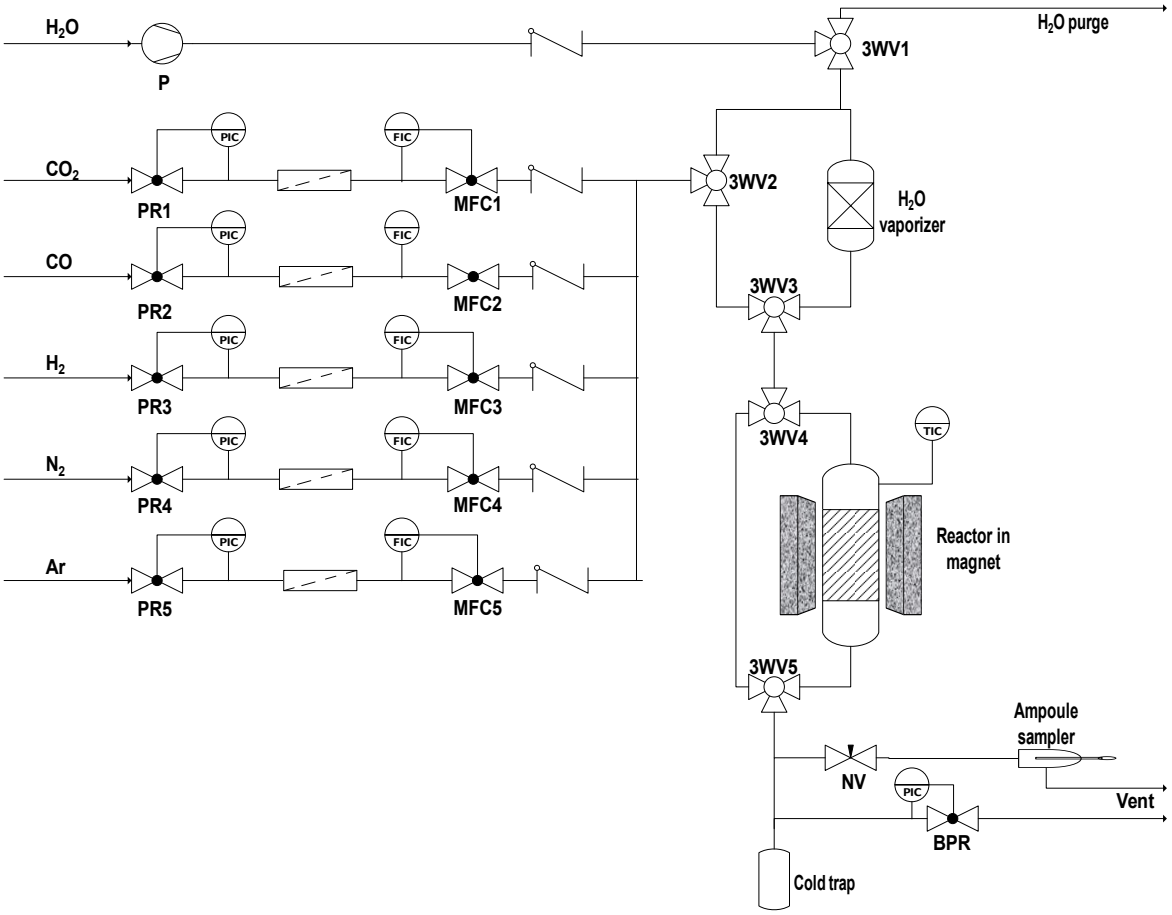

Figure 4.8. In-situ magnetometer experimental setup PR_1-5: Pressure regulators, MFC_1-5: Mass flow regulators/controllers, 3WV_1-5: three way valves, NV: Needle valve, BPR: backpressure regulator, PIC: Pressure indicator and control, FIC: Flow indicator control, TIC: temperature indicator and control.

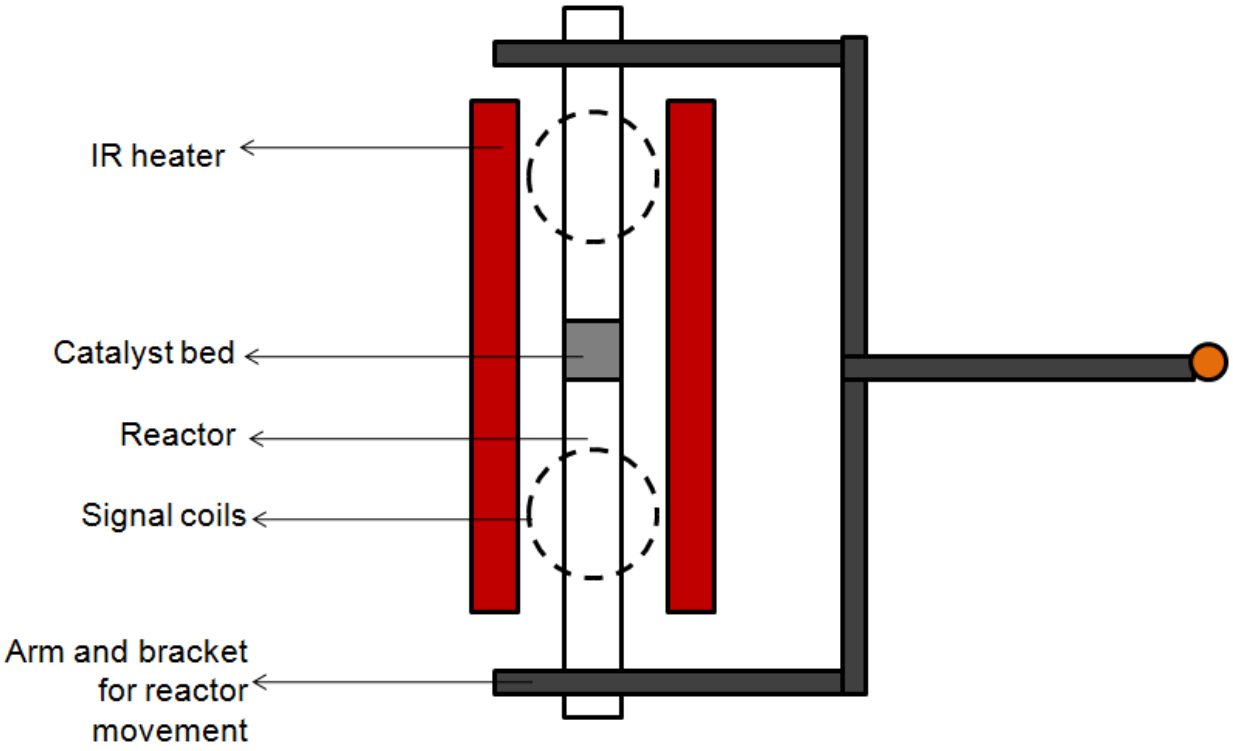

Figure 4.9. Side view In-situ magnetometer set up

4.3.7.2. Reactor set-up

As depicted in Figure 4.10 below, a stainless steel reactor (O.D. 0.5", I.D. 9.7 mm) was used. It has a non-magnetic brass frit to support the catalyst bed and prevent catalyst loss through the reactor. 1.5 g of the model catalyst was loaded into the reactor between two thin layers of glass wool. The loaded reactor was then secured in the aluminium holding bracket which places the reactor equi-distant from the infrared heaters and between the two magnetic coils. A non-magnetic thermocouple was then inserted into the reactor and the rest of the reactor filled with silicon carbide. A computer controlled electromotor is used to move the reactor axially in order to induce a magnetic signal from the sample.

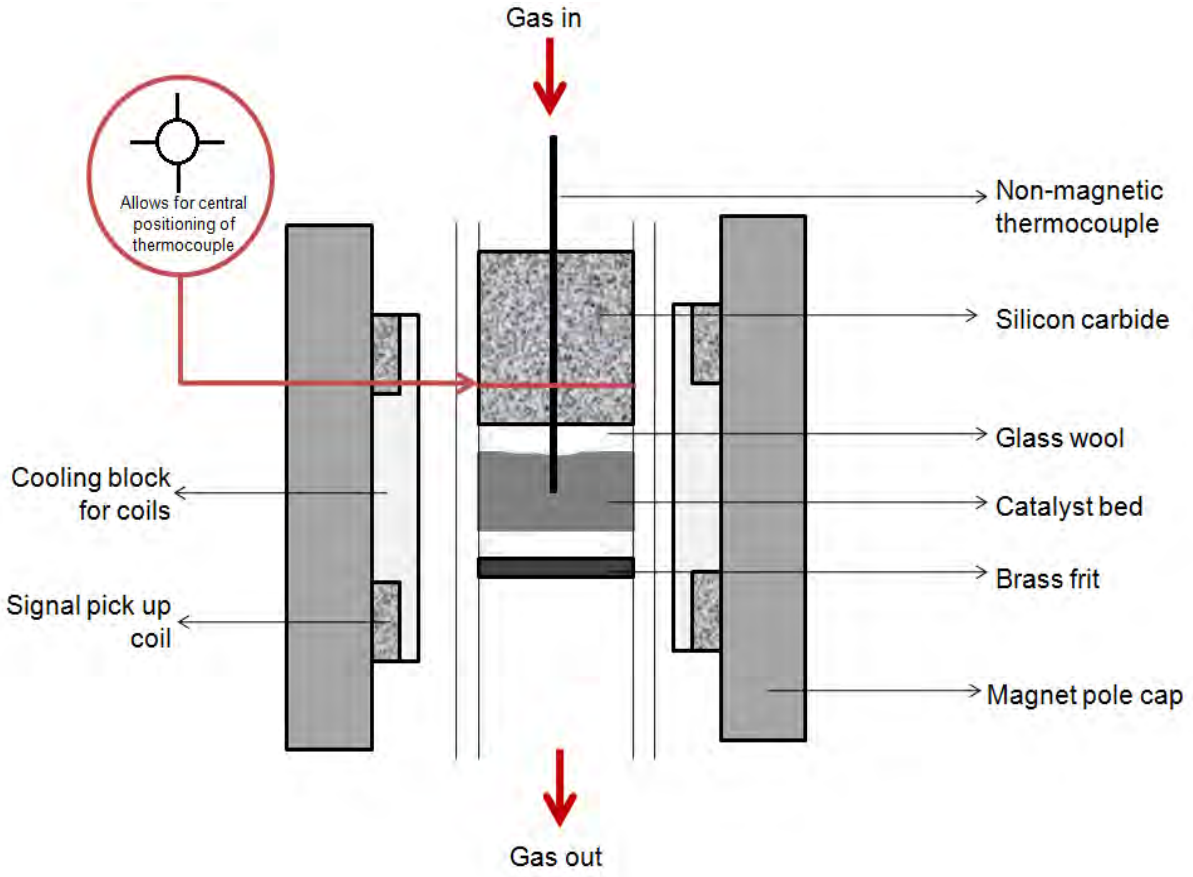

Figure 4.10. Schematic of fixed bed reactor configuration used for *in-situ* magnetometer experiments

4.3.7.3. Experimental procedure

4.3.7.3.1. *In situ* reduction

The model catalysts were activated *in situ* before investigating the effects of crystallite size on thermally induced sintering at different temperatures under inert conditions and in the presence of water vapour. The model catalysts were reduced at atmospheric pressure by flowing 200 mL (NTP)/min of hydrogen and heating the reactor from room temperature to 250 °C (heating rate: 1 °C/min) and holding for 80 minutes. The sample was then cooled to 150 °C (cooling rate: 10 °C/min) under argon (100 mL (NTP)/min).

4.3.7.3.2. Thermal sintering tests in an inert atmosphere

The effects of elevated temperatures on crystallite growth were investigated by exposing the catalysts to temperatures ranging from 300 °C to 650 °C. These conditions were chosen because temperature at the inlet of the methanation reaction is typically in the range of 300 °C. Due to the exothermicity of the methanation reaction, temperatures may increase beyond 650 °C.

The temperature tests were conducted under argon (100 mL (NTP)/min). After reduction, the sample under investigation was heated to 250 °C (heating rate: 5 °C/min) and then to 300 °C (heating rate: 1 °C/min) and held at 300 °C for 1 hour. The Curie temperature of nickel is 358 °C and above this temperature nickel samples will not display any magnetisation. In order to obtain meaningful magnetic data, measurements had to be taken at a temperature well below this temperature. Hence, the reactor was cooled down to 150 °C (cooling rate: 10 °C/min). The reactor was then heated to 300 °C (heating rate: 5 °C/min) and then to 350 °C (heating rate: 1 °C/min). It was then held at 350 °C for an hour after which it was cooled to 150 °C (cooling rate: 10 °C/min). Temperature tests were conducted in this manner up to 650 °C increasing the temperature in increments of 50 °C for each subsequent test.

After the temperature tests, the reactor was allowed to cool to room temperature under argon (100 mL (NTP)/min). Carbon dioxide was then flowed through the reactor for one hour in order to passivate the catalyst for further characterisation.

4.3.7.3.3. Thermal sintering tests in a steam/hydrogen atmosphere

The effect of water vapour on crystallite growth in the model catalysts was investigated by co-feeding water and hydrogen to the reactor at temperatures ranging between 250 °C and 650 °C.

After reduction of the catalyst sample and cooling to 150 °C, the system was then pressurised to 10 bar using 100 mL (NTP)/min of argon. Thereafter, the reactor was bypassed (valves 3WV4 and 3WV5) and the gas was allowed to flow through the

vaporiser (valves 3WV2 and 3WV3). The HPLC pump was then used to pump 0.10 mL/min of water to the water vaporizer (3WV1). The gas was changed from argon to hydrogen (25 mL (NTP)/min) allowing for a steam/hydrogen partial pressure ratio of $P_{H_2O}/P_{H_2} = 5$.In the absence of side reactions, this water to hydrogen partial pressure corresponds to a conversion of 94 % in the methanation reaction. This condition thus simulates the effects of water vapour at the high conversions associated with the methanation process. The reactor was then heated to 250 °C (heating rate: 5 °C/min) and then to 300 °C (heating rate: 1 °C/min). At 300 °C, gas flow was allowed back through the reactor (valves 3WV4 and 3WV5). The reactor temperature was held for one hour at 300 °C with hydrogen and water vapour flowing through the vaporizer and reactor. After an hour the gas was changed from hydrogen back to argon (100 mL (NTP)/min) and the reactor cooled to 150 °C (cooling rate: 10 °C/min). The water vaporizer was bypassed using valves 3WV2 and 3WV3. The water from the HPLC pump was diverted away from the water vaporizer to the purge (valve 3WV1). The system was then depressurised back to atmospheric pressure.

This process was repeated at 350 °C, 450 °C, 550 °C and 650 °C with the same heating procedure as outlined in Section 4.4.3 above.

After the water co-feeding experiments, the reactor was cooled to room temperature under argon. Nickel is pyrophoric which implies that it can ignite spontaneously or react violently when exposed to air, resulting in a dramatic change in its physico-chemical properties.Thus, the spent catalyst samples were passivated by flowing carbon dioxide through the reactor for one hour, prior to unloading, in preparation for further characterisation.

4.3.8. Magnetic measurement procedure

4.3.8.1. Reduction

The magnetisation of the catalyst sample was measured at an external applied field of 20 kOe and 0 kOe every 5 minutes during the reduction of the sample as well as

the subsequent cooling of the reduced catalyst to 150 °C. Readings at 20 kOe give an indication of the magnetisation of the sample whilst the reading at 0 kOe gives an indication of the fraction of the sample which displays remnant magnetisation. At 150 °C, a full hysteresis (38 minutes) was run: 65 magnetisation readings taken at and between external applied fields of 20 kOe and -20 kOe. Crystallite size data for superparamagnetic samples can be extracted from hysteresis measurements by making use of the Langevin equation (Equation 8) (Appendix D). The magnetisation of the sample was again measured at an external applied field of 20 kOe and 0 kOe whilst the sample was first heated to 250 °C (heating rate: 5 °C/min) and then cooled to 50 °C (cooling rate: 10 °C/min).

4.3.8.2. Thermal sintering tests in an inert atmosphere

During all temperature tests, the magnetisation of the sample was measured at an external field of 20 kOe and 0 kOe every five minutes during the heating stage, holding, as well as during the cooling back to 150 °C. At 150 °C a full hysteresis was run before conducting the next temperature test.

4.3.8.3. Thermal sintering tests in a steam/hydrogen atmosphere

The magnetisation of the catalyst sample was measured during the heating of the reactor as well as when it was cooled to 150 °C every five minutes at external fields of 20 kOe and 0 kOe. After each sintering test in the steam/hydrogen atmosphere, argon was allowed to flow through the reactor for an additional 30 minutes in order to ensure that all hydrogen was removed from the system. Hydrogen may cause magnetic decoupling which may diminish the magnetic signal (Chernavskii, *et al*., 2009).Thereafter, before conducting the subsequent water test, a full hysteresis was run.

4.3.9. External reduction and passivation

The model catalysts were also reduced in a fixed bed glass tube reactor (Figure 4.11). 200 mL (NTP)/min of hydrogen was allowed to flow through the sample whilst heating the reactor from room temperature to 250 °C (heating rate: 1 °C/min) and holding for 80 minutes. The sample was then cooled to 30 °C (cooling rate: 10 °C/min) under argon (100 mL (NTP)/min). Carbon dioxide was then allowed to flow through the sample in order to passivate it.

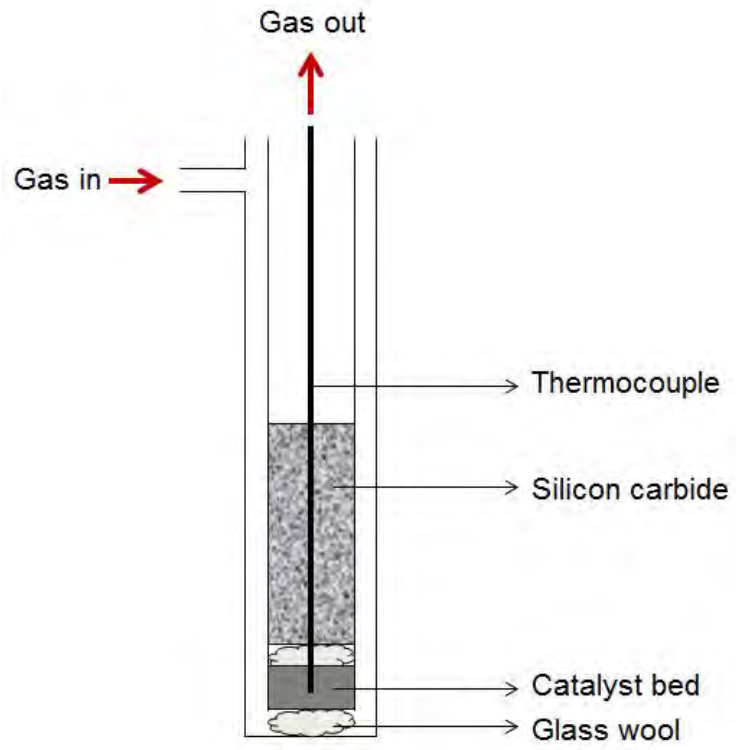

Figure 4.11 Schematic of fixed bed reactor configuration used for external reduction and passivation of model catalysts

5. Results and discussion

5.1. Characterisation of unsupported nanocrystallites

Unsupported nickel nanoparticles were synthesised according to the reverse micelle technique as outlined in Section 4.1. These nanoparticles were characterised using PXRD and TEM.

5.1.1. PXRD analysis

PXRD analysis was conducted in order to identify the different phases present in the nanoparticle samples as well as to determine the composition of the samples and the average crystallite size of the nanocrystallites. Figure 5.1 below contains the diffractograms obtained for the five samples prepared using the microemulsion technique. The figure also contains the standard diffraction peak positions for Ni and NiO as recorded in the ICDD database. According to Figure 5.1, all the samples contained NiO. The characteristic NiO peaks appeared to increase in peak width with a decrease in water/surfactant ratio. Peak broadening is an indication of decreasing average crystallite size. This seems to suggest that varying the water/surfactant did have an impact on average NiO crystallite size and that as water/surfactant ratio decreased, so too did the average crystallite size. From Figure 5.1 it can also be noted that samples A, G, D and H also contained metallic Ni. These characteristic Ni peaks were sharper than the corresponding NiO peaks, suggesting that the Ni crystallites in each sample were much larger than the NiO crystallites. What could also be noted was that the relative peak intensities of the Ni increased for each subsequent sample indicating an increase in the relative amount of Ni in each sample. This in turn suggests that the amount of Ni formed increased with increasing water/surfactant ratio. TOPAS was used to determine the average crystallite size of the NiO and Ni in the five samples, as well as to quantify the relative amounts of each (Appendix C). This data is recorded in Table 5.1. The R_{wp} value gives an

indication as to how well the proposed pattern fits the actual diffractogram. An R_{wp} value below 10 is indicative of a sufficiently good fit.

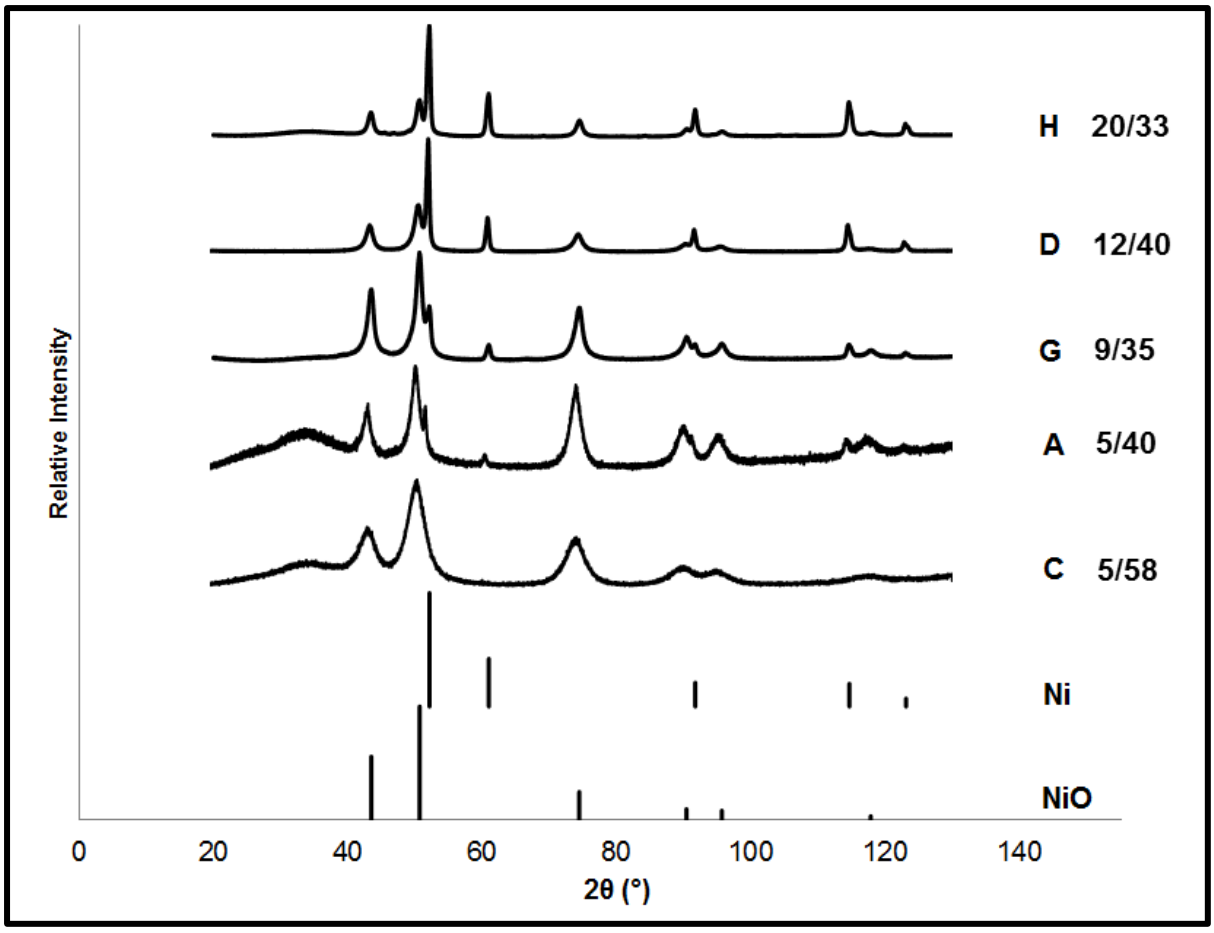

Figure 5.1. PXRD diffractograms unsupported nickel nanocrystallites

Table 5.1 confirms that as the water/surfactant ratio increased, so too did the average crystallite size. This then confirms that varying the water/surfactant ratio can be used in order to synthesise crystallites of different sizes. What was also noted was that the relative amount of Ni in the samples also increases with increasing water to surfactant ratio from 0.00 % in Sample C to 41.31 % in Sample H. The resultant Ni crystallite size is also much larger than the corresponding NiO.

Table 5.1. Average crystallite size and composition unsupported NiO nanoparticles as determined from PXRD

Sample code	ω[i]	d_{NiO} (nm)	d_{Ni} (nm)	NiO (wt.%)	Ni (wt.%)	R_{wp}
C	5/58	3.9	-	100.00	0.00	8.4
A	5/40	5.3	24.1	94.48	5.52	7.7
G	9/35	7.6	27.1	93.93	6.07	7.8
D	12/40	8.5	35.5	75.88	24.12	7.4
H	20/33	12.3	34.6	58.69	41.31	14.6

[i] water/surfactant ratio (g/g)

The presence of NiO in the calcined samples was to be expected. What was unexpected was the concurrent synthesis of Ni in an oxidising atmosphere. This suggests that during calcination of the amorphous samples, a reducing atmosphere was created which resulted in the reduction of the NiO. This may have been as a result of the thermal decomposition of the surfactant remaining after the washing and drying of the samples. The DOW Chemical Company (2013) has reported that ethoxylated anionic surfactants, such as the PEDGE used in this study, are prone to thermal decomposition when exposed to temperatures beyond 250 °C in the presence of air. During this thermal degradation, the ethoxylate chain is shortened resulting in the formation of volatile products including acetalaldehyde, formaldehyde, miscellaneous glycol ethers, ethylene glycols, 1,4dioxane, acetone, ethanol and the starting alcohol of the surfactant. Although the reduction of metal oxides by oxygenated hydrocarbons has not been extensively studied, a few authors have reported on this phenomenon. Cheng & Dupont (2013), Ayyappan, *et al*. (1997) and Kondrat, *et al*. (2011) all found that the auto-reduction of metal oxides could indeed be achieved with oxygenated hydrocarbons. The relative amount of Ni in each sample also seems to increase with increasing water to surfactant ratio. This may have as a consequence of the average crystallite size of the NiO in each sample or the amount of surfactant available in each sample. As water/surfactant ratio increased, less extensive washing was necessary during the nanoparticle preparation and thus more surfactant may have been available to facilitate the auto-reduction process. Furthermore, the size of the Ni in each sample is much larger

than the corresponding NiO nanocrystallites indicating that severe sintering occurs during this auto-reduction process.

5.1.2. TEM analysis

Figure 5.2 contains the TEM micrographs obtained for the five different unsupported samples prepared by varying the water/surfactant ratio. TEM was used in order to determine the morphology of the particles as well as to determine average particle size as well as size distributions. When considering Figure 5.2, it can be seen that the particles for all samples appeared to have a mostly spherical morphology. Samples C, A and G appeared to have more uniformity amongst the particles whilst D and H displayed some deviation from this spherical morphology. The nanoparticles also displayed a strong tendency to aggregate despite extensive sonication prior to analysis.

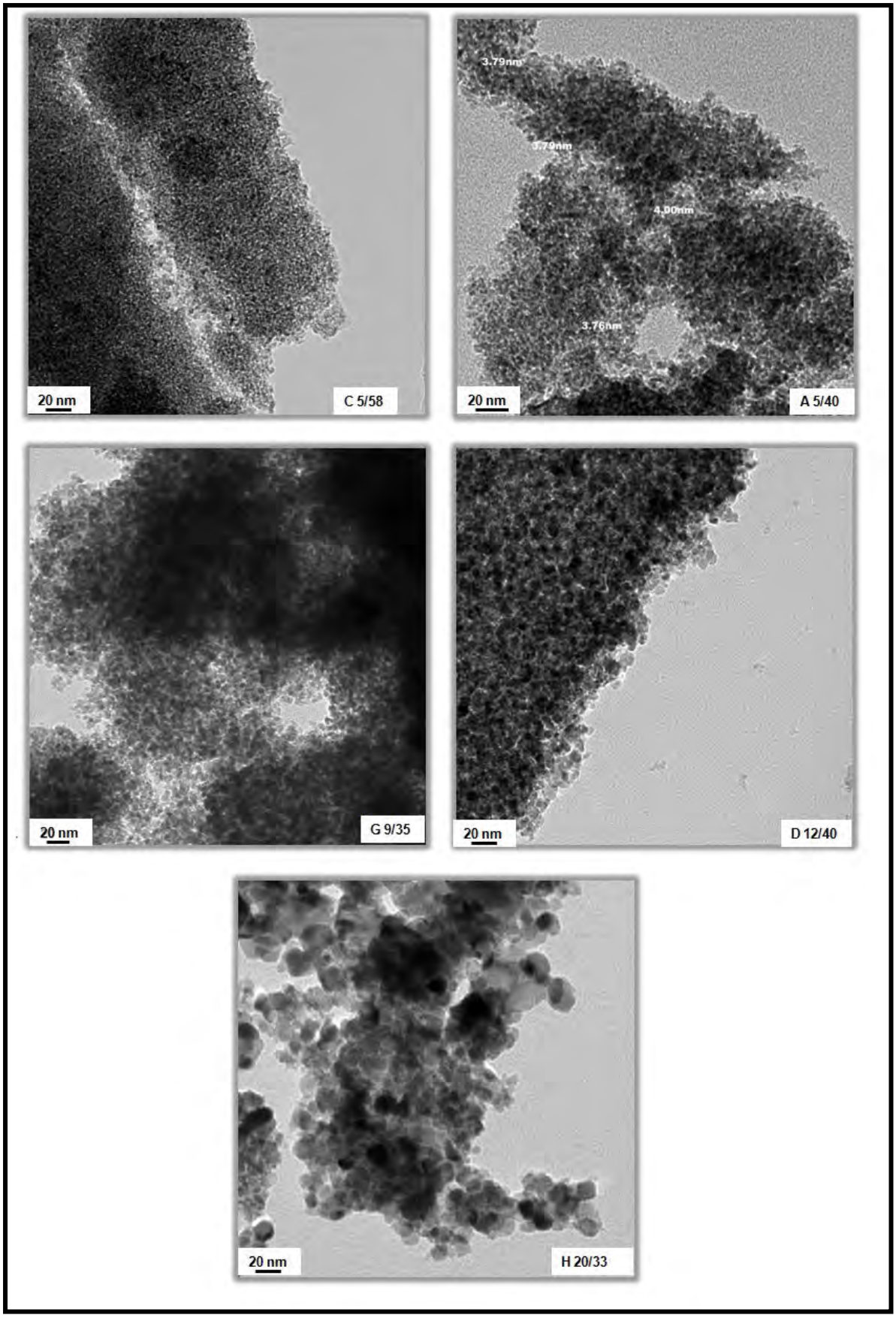

Figure 5.2. TEM images unsupported NiO nanoparticles

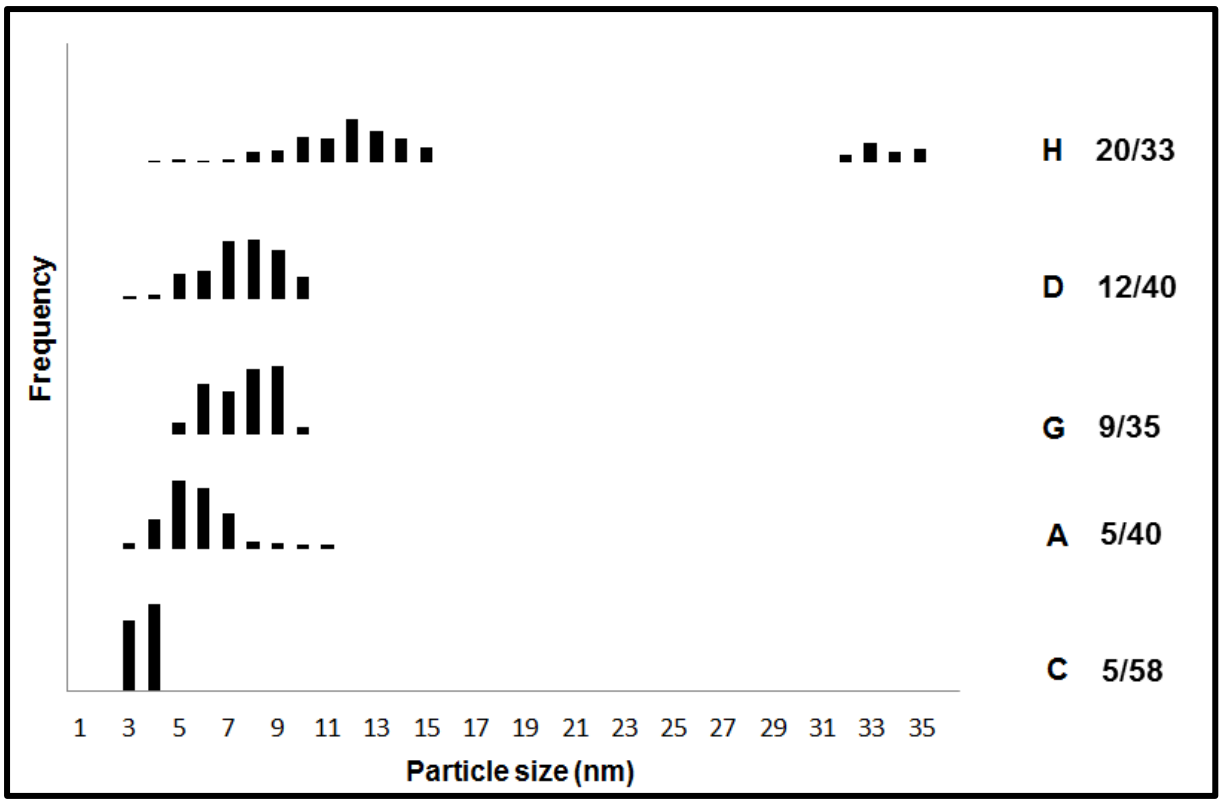

Figure 5.3. Size distributions for unsupported nanoparticles as obtained from TEM analysis

Figure 5.3 gives an indication of the number based size distributions obtained for the unsupported nickel nanoparticle samples. Table 5.2 contains the average particle size and standard deviations of the unsupported nickel samples (volume based) as determined from analysing a minimum of 300 particles. This data again seems to suggest that varying the water/surfactant ratio does indeed result in particles of different sizes. As the water/surfactant ratio increased, so too did the average particle size. The particles also displayed a relatively narrow size distribution. However, as the water to surfactant ratio increased, and as the average particle size increased, so too did the size distribution. Lopez-Quintela & Rivas (1993) and (Mabaso, 2005) have confirmed that the size of the microdroplets in the microemulsioncontrol the final size of the particles. According to Blanco & Lopez-Quintela (1997) the size of these microdroplets is proportional to the mole ratio [H_2O]/[surfactant] and thus the size of these water cores can be adjusted by varying the water/surfactant ratio and, in turn, water droplets of different sizes can be used to

influence particle growth. Blanco & Lopez-Quintela (1997) also noted that the small droplet range, particle size could be tightly controlled. However, in the large droplet range, some of this control is lost. They suggest that in large droplets the water/surfactant ratio gives way to reagent concentration as the controlling factor in controlling particle size. Eastoe, *et al*. (2006) report that at low water/surfactant ratios,there is less intermicellar exchange resulting in a decreased growth rate. As this ratio increases, the film surrounding the micelles becomes more fluid, allowing for greater intermicellar exchange and an increased growth rate, which may contribute to the wider size distribution.

When considering the size distributions for sample H, two populations in terms of size can be identified: small particles below 15 nm and much larger particles beyond 30 nm in size. From the PXRD data (Section 5.1.1), sample H contained NiO crystallites with sizes in the less than 15 nm range, and Ni nanocrystallites with average sizes beyond 30 nm. Sample H also contained a significant amount of Ni (41.3 %) which would explain why the size distributions for this sample was more significantly impacted than samples A, G and D which also contained some Ni but a comparatively small amount (5.5 %, 6.1%, and 24.1 % respectively). These different populations were thus treated individually, determining an average particle size and standard deviation for each. The average particle size data as obtained from the TEM analysis is recorded in Table 5.2.

Table 5.2. Average particle size (volume based) and standard deviation of unsupported NiO nanoparticles as obtained from TEM analysis

Sample code	ω[i]	d_{NiO} (nm)	σ_{NiO} (nm)	d_{Ni} (nm)	σ_{Ni} (nm)
C	5/58	3.1	0.6	-	-
A	5/40	5.2	1.3	-	-
G	9/35	7.6	1.2	-	-
D	12/40	8.1	1.5	-	-
H	20/33	12.9	3.0	33.9	1.0

[i] water/surfactant ratio (g/g)

The very large particles which, based on PXRD data, were postulated to be metallic Ni, were much larger than the NiO. The severe clustering of the particles may have created an environment which promoted the sintering of the metallic Ni which formed.

The size data obtained from PXRD and TEM analysis for the NiO nanoparticles was combined in order to construct Figure 5.4 which allows a comparison of the average particles sizes obtained using the two methods.

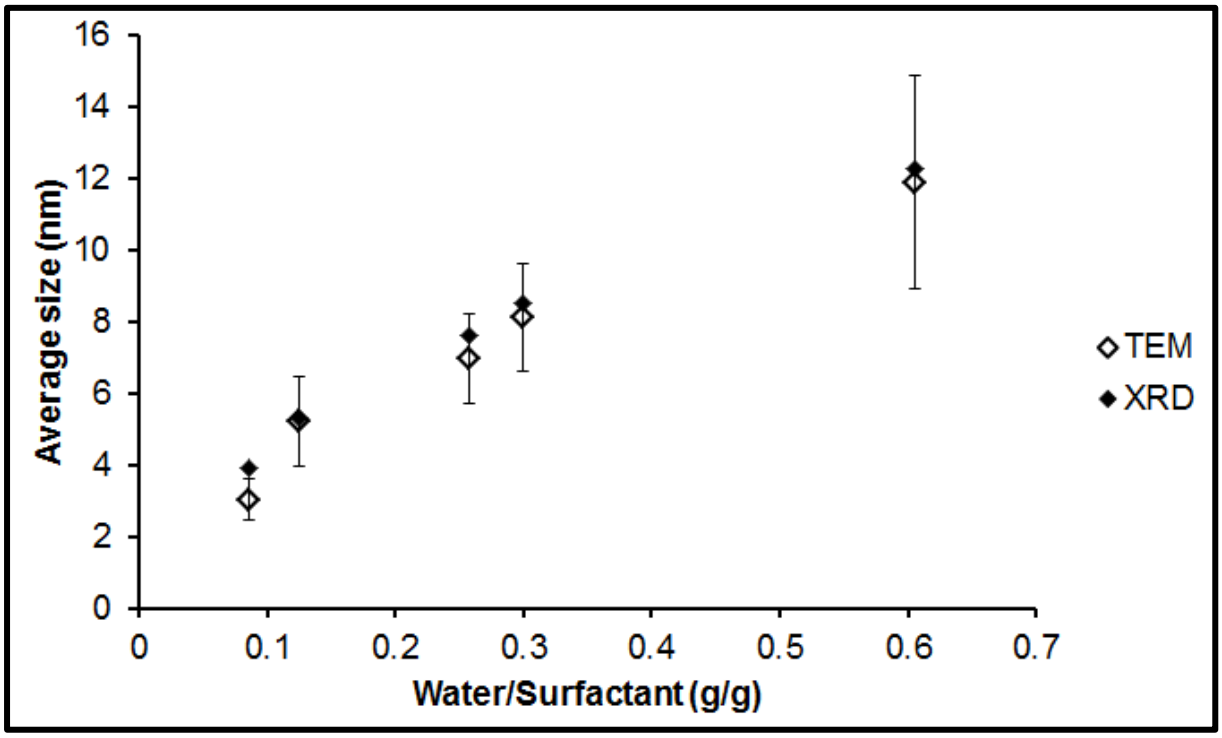

Figure 5.4. Comparison of PXRD and TEM size results and dependency on water/surfactant ratio for unsupported NiO nanoparticles

There was very good agreement between the results obtained from PXRD and TEM. Results obtained from both techniques indicate that average crystallite size of the NiO particles is linearly dependent on the water to surfactant ratio. A similar result was reported by Mabaso (2005) (iron system) and Robinson, *et al*. (1991) (cadmium system). Robinson, *et al*. (1990) proposed that this phenomenon may have been as

a result of the linear dependency of the corresponding droplets in the microemulsion prior to precipitation.

5.1.3. Summary

The reverse micelle technique was successfully employed to synthesise NiO nanoparticles with a narrow size distribution, where the size of the particles was linearly dependent on the water/surfactant ratio. An additional parameter should be investigated for larger particles as increasing the water/surfactant ratio corresponded with an increase in the size distribution. Some metallic Ni was formed during the calcination of the amorphous material, with the relative amount increasing with increasing water/surfactant ratio and average particle size. It was likely that at 300 °C, the surfactant decomposed, creating a reducing atmosphere. The tendency of the particles to aggregate then created an environment which promoted the sintering of the resultant Ni.

5.2. Characterisation of supported nanocrystallites

Supported nanocrystallites were synthesised according to the two methods described in Section 4.2. Method 1 involved the addition of the support material, γ-alumina (BET surface area = 146 m^2/g, adsorption average pore width = 117 Å), during the preparation of the microemulsion. Method 2 included the addition of the support to nanoparticles which were synthesised according to the method described in Section 4.1. These supported samples were then fully characterised using PXRD, TEM, TPR and magnetic measurements. Cat C Meth 1 and Cat H Meth 1 were synthesised using Method 1 and Cat C Meth 2 and Cat H Meth 2 were prepared according to Method 2. Based on the results obtained with the unsupported particles it was anticipated that this would yield supported catalysts with the smallest and largest particles obtainable.

5.2.1. PXRD analysis of supported nanoparticles

PXRD was used to characterise the supported nickel nanoparticles. It was used to determine the phases present in the samples and the average crystallite size of the nanocrystallites. The results for this analysis are graphically represented in Figure 5.5. The diffraction patterns obtained for the samples prepared using Method 1 (Cat C Meth 1 and Cat H Meth 1) were dominated by the diffraction pattern for the support, γ alumina, with no peaks visible which could be attributed to NiO or Ni. This made it difficult to discern any information relating to crystallite size for these samples using PXRD.

The diffraction patterns for the samples prepared using Method 2 showed characteristic NiO peaks and also, in the instance of Cat H Meth 2, characteristic Ni peaks. These samples could then be analysed using TOPAS in order to determine average crystallite size, as recorded in Table 5.3.

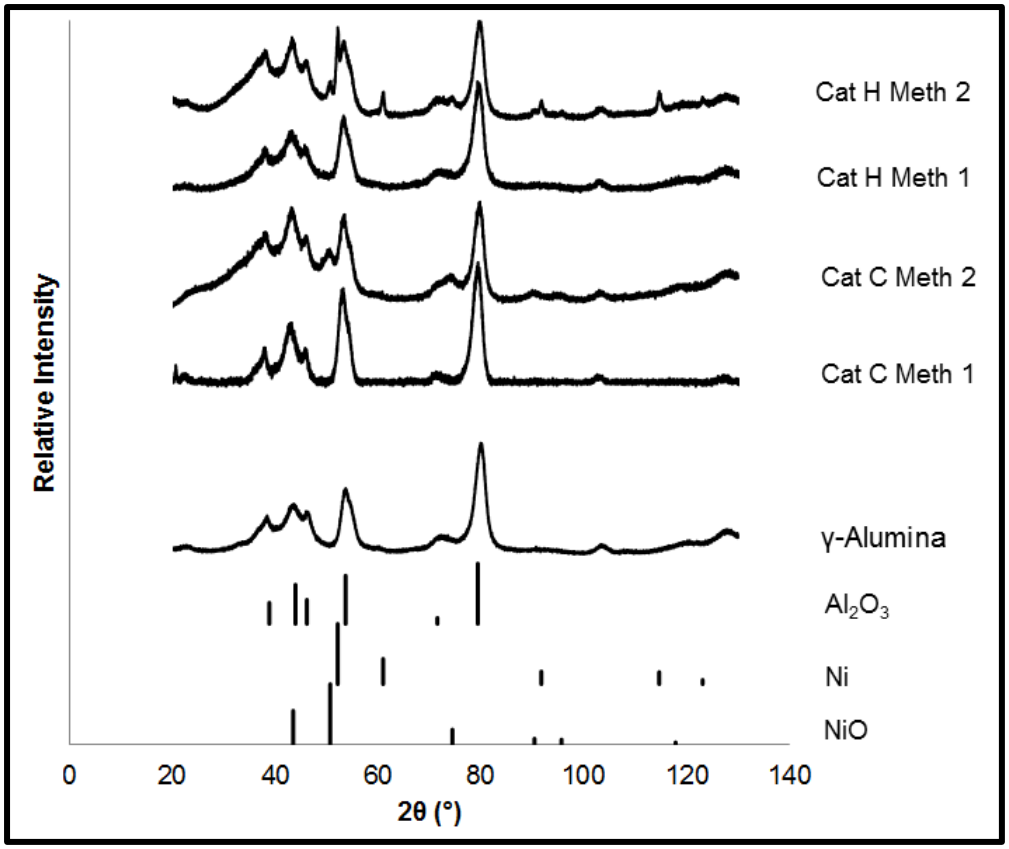

Figure 5.5. PXRD diffractograms of supported nanoparticles

Table 5.3. Average crystallite size of supported nanoparticles prepared using two different methods as determined from PXRD

Sample code	d_{NiO} (nm)	d_{Ni} (nm)	R_{wp}
Cat C Meth 1	-	-	
Cat C Meth 2	3.9	-	6.8
Cat H Meth 1	-	-	
Cat H Meth 2	12.3	34.5	8.6

5.2.2. AAS of supported nanoparticles

The four samples were digested in an acid mixture in preparation for AAS analysis in order to determine the Ni content of the samples. The aim during synthesis of these supported samples was to obtain a metal loading of 10 wt.% Ni on γ alumina. The AAS data is recorded in Table 5.4 below.

Table 5.4. Metallic loading of supported nanoparticles prepared according to two different methods

Sample code	Ni loading (wt.%)
Cat C Meth1	5.3
Cat C Meth2	9.7
Cat H Meth 1	5.0
Cat H Meth 2	10.2

Cat C Meth 1 and Cat H Meth 1 had lower than anticipated loadings of 5.3 wt.% and 5.0 wt.% respectively. Conversely, Method 2 produced samples with far more accurate metal loadings of 9.7 wt.% and 10.2 wt.% for Cat C Meth2 and Cat H Meth 2 respectively. Method 2 is based on the addition of the support to the already synthesised nanoparticles and so an accurate analysis of the amount of support necessary for a 10 wt.% metal loading can be done. Unfortunately, Method 1 relies on a theoretical determination of the amount of supported to be added based on the

reaction going to completion during the microemulsion preparation step. Furthermore, losses of nickel incurred during the vigorous washing step may have also contributed to the reduced metal content.

5.2.3. TEM analysis of supported nanoparticles

Figure 5.6 contains the TEM micrographs obtained for four samples of supported NiO nanoparticles. TEM was again used in order to determine the morphology of the supported particles as well as to determine average particle size and size distributions of the nanoparticles on the support as well as to qualitatively determine how well dispersed the particles were on the support. When considering Figure 5.6a and c, the TEM micrographs for the supported samples prepared according to Method 1, it can be noted that there was very poor contrast between the γ-alumina support and the particles. Size determination using TEM analysis was thus not a viable option. Furthermore, no qualitative information could be gained on the dispersion of the particles. This poor contrast between the support and the particles may have been as a result of the incorporation of nickel into the support matrix.

According to Figure 5.6b and d, however, the samples prepared using Method 2 did show sufficient contrast between the particles and the support. From these micrographs it could be observed that the nanoparticles retained their spherical morphology on addition of the support material. Unfortunately, this preparation method also resulted in very poor dispersion of the particles, as evidenced by the clustering of the particles on the support. This may have been as a direct consequence of the tendency of the unsupported particles to aggregate, as discussed in Section 5.1.2.

Figure 5.7 gives an indication of the size distributions obtained for the supported nickel nanoparticles. Table 5.3 contains the average volume based particle size and standard deviation for the supported nanoparticles. The nanoparticles again exhibited a narrow size distribution despite the support addition. The smaller particles had a far narrower distribution than the larger particles. This phenomenon was fully discussed in Section 5.1.2.

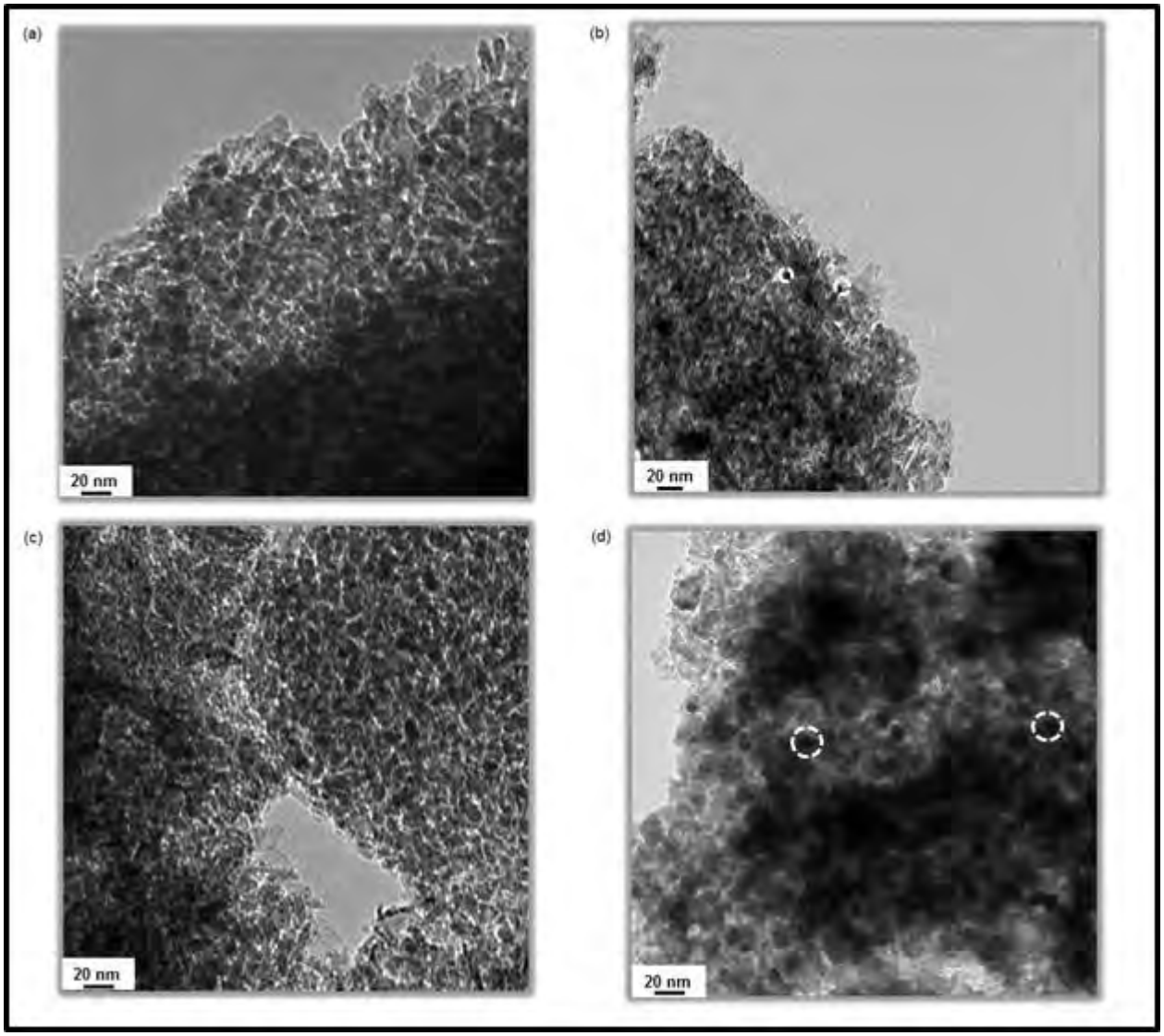

Figure 5.6. TEM micrographs of supported nanoparticles (a) Cat C Meth 1 (b) Cat C Meth 2 (c) Cat H Meth 1 (d) Cat H Meth 2

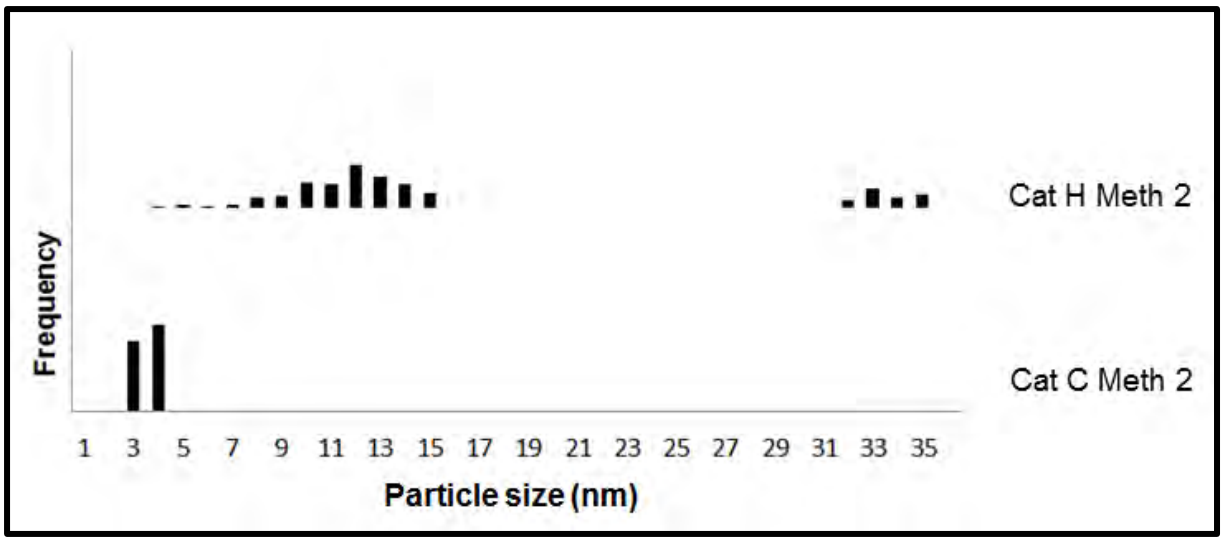

Figure 5.7. Size distributions for supported nanoparticles as obtained from TEM analysis

Table 5.5. Average particle size (volume based) and standard deviation of supported NiO nanoparticles as obtained from TEM analysis

Sample code	ω[I]	d_{NiO} (nm)	σ_{NiO} (nm)	d_{Ni} (nm)	σ_{Ni} (nm)
Cat C Meth 2	5/58	3.1	0.6	-	-
Cat H Meth 2	5/40	12.8	2.8	34.1	0.9

[I] water/surfactant ratio (g/g)

5.2.4. TPR of supported nanoparticles

In order to investigate the reduction behaviour of the supported samples, TPR was conducted in order to determine the hydrogen consumption as a function of temperature for the supported samples. The conversion of NiO to the catalytically active Ni is characterised by Equation 10.

$$NiO + H_2 \rightarrow Ni + H_2O \qquad \text{Equation 10}$$

TPR can be used to gain information regarding the reducibility of the samples, as well as give an indication of the extent of the interaction between the metal oxide

with the support (Holm & Clark, 1968).The reduction of γ alumina supported NiO in hydrogen is a well-studied process which should yield, in the absence of any strong metal support interactions, which typically inhibit this reduction process, a single peak indicative of the conversion of NiO to Ni. The reducibility may also be dependent on the preparation method (Li & Chen, 1995, Jasik, *et al*., 2005, Li, *et al*., 2006) as well as on metal loading (Rynkowski, *et al*., 1993) and particle size.

Figure 5.8 depicts the TPR profiles obtained for Cat C Meth1 and Cat H Meth1 prepared using Method 1 (Section 4.2.1) and Cat C Meth2 and Cat H Meth2 prepared using Method 2 (Section 4.2.2).

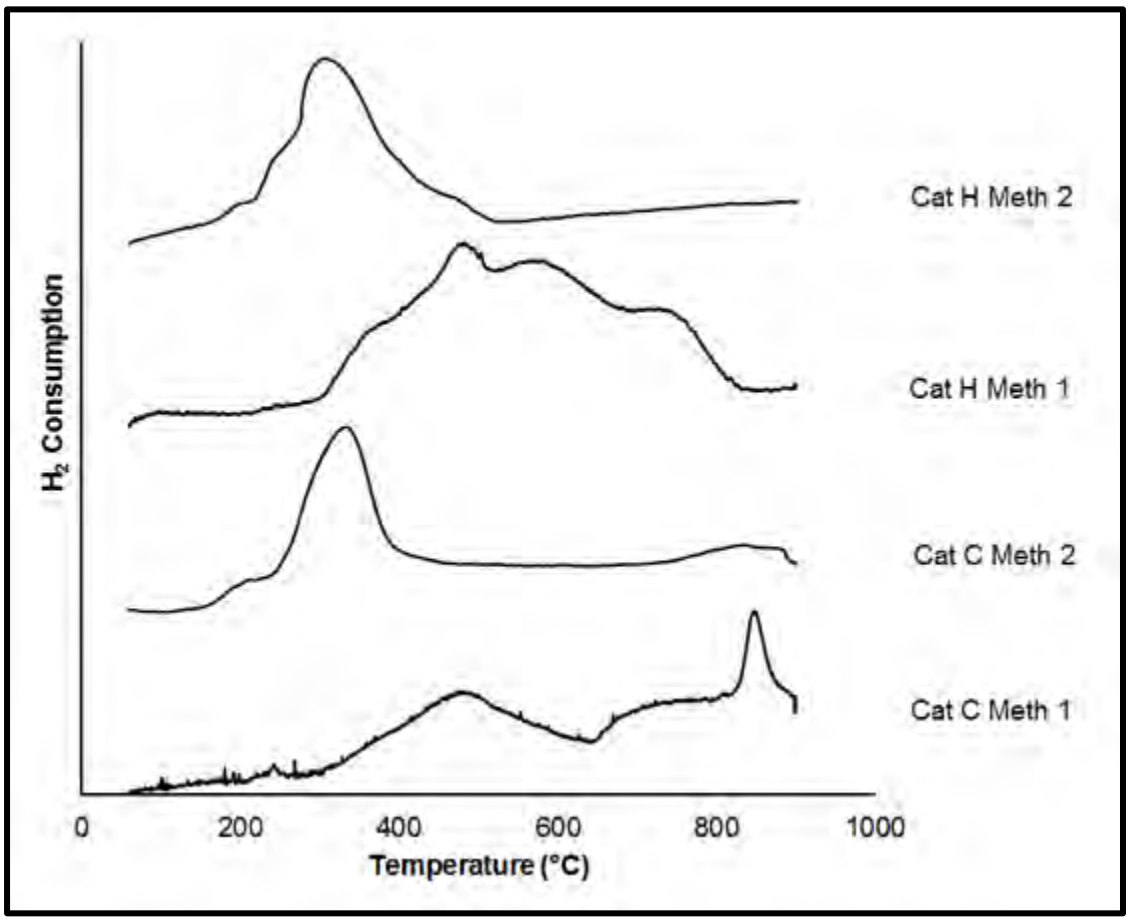

Figure 5.8. TPR profiles of supported NiO nanoparticles using two different preparation methods

The TPR profiles of the supported samples prepared using Method 1 were characterised by multiple broad peaks. The TPR profile of Cat C Meth 1 showed a broad peak with a maximum at 480 °C. There was also a shoulder between 650 °C and 820 °C followed by a sharp peak at 880 °C. Sharp peaks at these temperatures

are indicative of nickel aluminates. The profile for Cat H Meth 1 displayed multiple peaks between 300 °C and 800 °C.

In contrast, the TPR profiles for Cat C Meth 2 and Cat H Meth 2 showed single peaks for the reduction process as expected. This reduction, for both samples, started at approximately 220 °C, lower than the 300 °C observed for the catalysts prepared using Method 1. This seems to suggest that catalysts prepared by adding the support to the already synthesised nanoparticles results in catalysts with increased reducibility. Also, the reduction of the samples prepared using Method 2 was completed at 400 °C and 550 °C for Cat C Meth 2 and Cat H Meth 2 respectively, suggesting that the sample with smaller nanoparticles was easier to reduce than the one with larger particles.

The reduction behaviour displayed by the samples where the support was added during the microemulsion preparation seems to suggest that there may have been strong metal support interactions which decreased the reducibility of the samples. This may have been as a result of the incorporation of the nickel into the support matrix in the aqueous medium of the microemulsion. Addition of the support to already synthesised nanoparticles seemed to decrease these interactions, resulting in supported samples which were far easier to reduce. Fischer (2011) who also investigated the two preparation methods on a cobalt system, had similar findings where the supported material prepared according to Method 1 resulted in material which was difficult to reduce, indicative of the formation of cobalt aluminates. Fischer (2011) proposed that addition of the support during the microemulsion preparation stage may result in the incorporation of cobalt ions in the alumina matrix at the metal-support interface.

5.2.5. *In situ* magnetic measurements for supported nanoparticles

Cat C Meth 1 and Cat C Meth 2 was also reduced in the *in situ* magnetometer in order to use magnetic measurements to further investigate the reduction behaviour of the same catalyst prepared using two different methods. Based on the reduction obtained in Section 5.2.4, a reduction temperature of 550 °C was chosen. The

catalysts were both reduced at 550 °C (heating rate: 1 °C/min) in hydrogen and then the samples cooled to 50 °C under argon. This process is represented in Figure 5.9. Magnetic readings were taken at the maximum field strength obtainable with the magnetometer (20 kOe). When heating NiO supported on γ alumina, no magnetic signal will be observed because both NiO and γ-alumina are not ferromagnetic. Once the NiO is converted to Ni, the magnetic signal should increase because Ni is ferromagnetic. No change was observed in the magnetic signal of Cat C Meth 1 during the heating of the sample in hydrogen up to 550 °C. On cooling in argon however, a slight increase in the magnetic signal was observed, indicating that some of the NiO was reduced to the ferromagnetic Ni. When Cat C Meth 2 was heated in hydrogen, there was no change in magnetic signal up to 220 °C at which point the magnetic signal started to increase, indicating that at 220 °C, the transformation of NiO to Ni began. The signal increases until 310 °C where the signal starts to decrease. At 410 °C, no signal is observed. This is because the sample is now beyond the Curie temperature of nickel (358 °C, Serway & Jewett, Jr., 2014), beyond which no magnetic signal will be observed. On cooling in argon to 50 °C, there is a very sharp increase in the magnetic signal of the sample, much greater than that observed for Cat C Meth 1, indicating that more of the NiO was converted to ferromagnetic Ni.

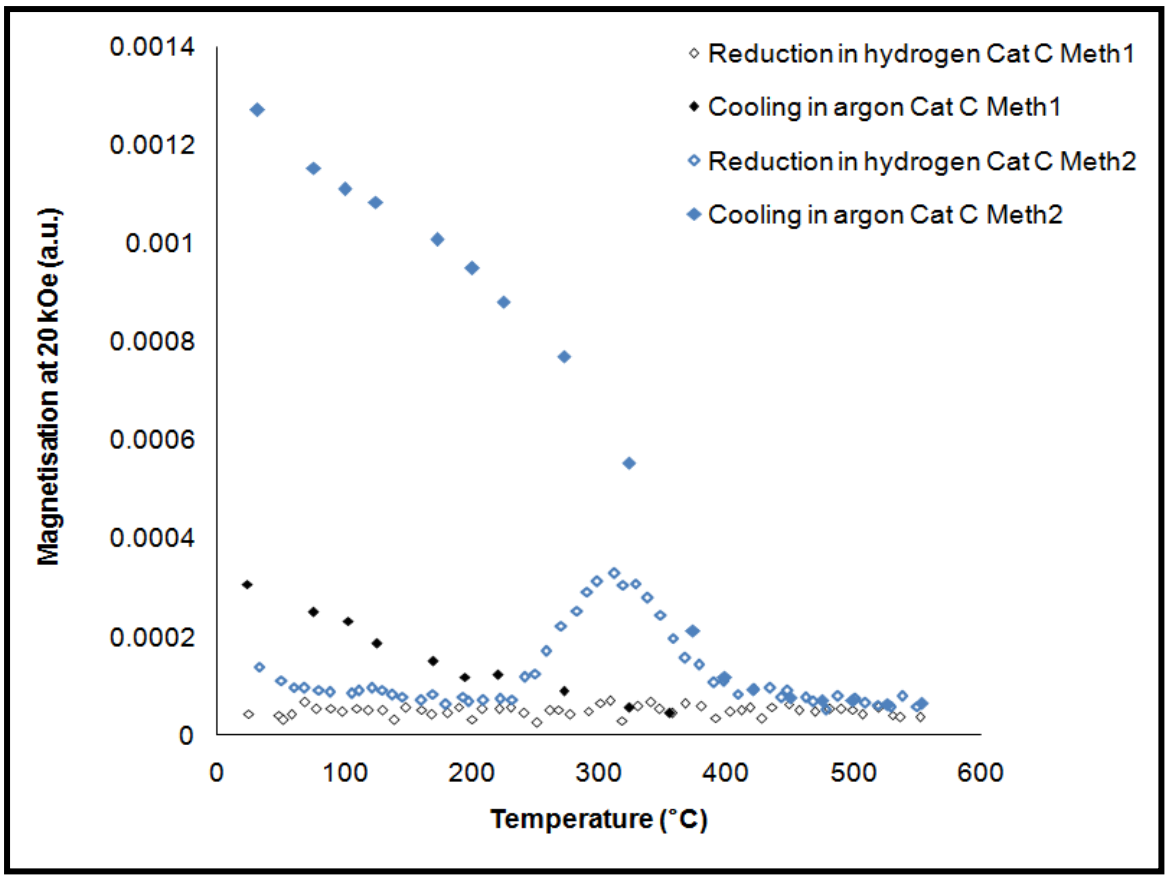

Figure 5.9. *In situ* reduction of Cat C prepared using two different preparation methods

The magnetic data thus seems to support the notion that the sample prepared using Method 2 was far easier to reduce than the one synthesised according to Method 2: when both samples were exposed to the same reduction conditions, there was a far greater relative increase in the magnetic signal indicating the conversion of a greater fraction of NiO to Ni in the sample prepared using Method 2.

Figure 5.10 is the hysteresis data obtained for Cat C Meth 1 and Cat C Meth 2. According to this figure, Cat C Meth 2 reached saturation after reduction, displaying hysteresis behaviour consistent with superparamagnetic material. Cat C Meth 1 failed to reach saturation. This further corroborates the magnetisation data in Figure 5.9 in that Cat C prepared according to Method 2 was reduced to a far greater extent than Cat C Meth 1.

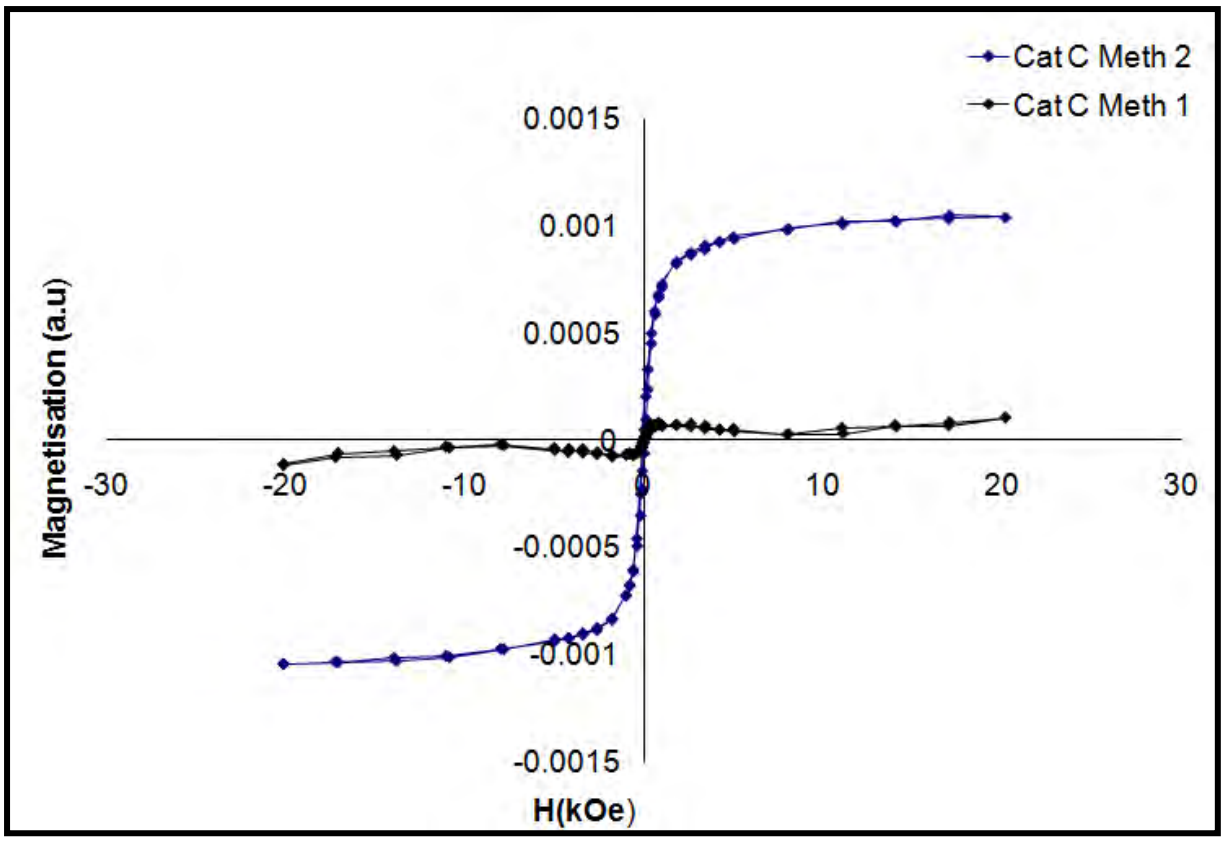

Figure 5.10. Hysteresis data obtained at 150 °C for Cat C prepared according to two different methods

5.2.6. Summary

Supported nanoparticles of different sizes were prepared using two different preparation methods. The samples prepared by support addition during the microemulsion preparation step could not be fully characterised using PXRD or TEM analysis: the diffraction patterns for these samples were dominated by the pattern for the support and there were no discernible NiO peaks. There was also very poor contrast between the support and particles. The required metal loading could also not be achieved using this method. These samples also displayed poor reducibility, making it difficult to use magnetic methods to characterise the samples.

The supported nanoparticles prepared by support addition to already synthesised and calcined nickel nanoparticles resulted in material which could be effectively characterised. PXRD was used to determine average size, which correlated well with

the average particle size and size distribution obtained from TEM analysis. The particles retained their narrow size distribution and spherical morphology on support addition. These samples also showed markedly improved reducibility, making them highly suitable for a magnetic investigation.

5.3. Model catalysts for sintering study

Model catalysts were synthesised using preparation Method 2 on nanoparticles which exhibited uniformity in morphology and a relatively narrow size distribution. According to the data obtained and analysed in Section 5.2, Method 2 resulted in catalysts where the loading could be targeted with great accuracy and which displayed increased reducibility and gave significantly more meaningful magnetic results, making this preparation method more suitable for the preparation of material required for an *in situ* magnetic study. However, Method 2 also resulted in poor dispersion with severe clustering of the nanoparticles on the support. When there is clustering it becomes difficult to discern whether the behaviour observed can be attributed to individual particles or the cluster. Furthermore it can be anticipated that sintering with such catalysts may be relatively facile. Thus, in an attempt to minimise clustering of nickel nanoparticles and in order to improve dispersion, the metal loading for the model catalysts was decreased from 10 wt.% to 4.0 wt.%.

5.3.1. Synthesis of model nickel catalysts

5.3.1.1. PXRD of synthesised model catalysts

The PXRD diffractograms obtained for the model catalysts ModCatC and ModCatH, recorded in Figure 5.11, allow for the determination of the phases present in the samples, as well as the average crystallite size of nickel. These diffraction patterns are again dominated by the diffraction pattern of the γ-alumina. However, characteristic nickel oxide peaks were observed for both model catalysts, indicating the presence of nickel oxide in the samples. There was also metallic nickel present

in ModCatH. This was a direct consequence of the metallic nickel particles which form during the synthesis of unsupported NiO nanoparticles (Section 5.1). The diffraction patterns, in conjunction with TOPAS, were used in order to extract average crystallite size data (Table 5.6). Two sizes were thus obtained for the sintering study: 5.3 nm and 12.3 nm.

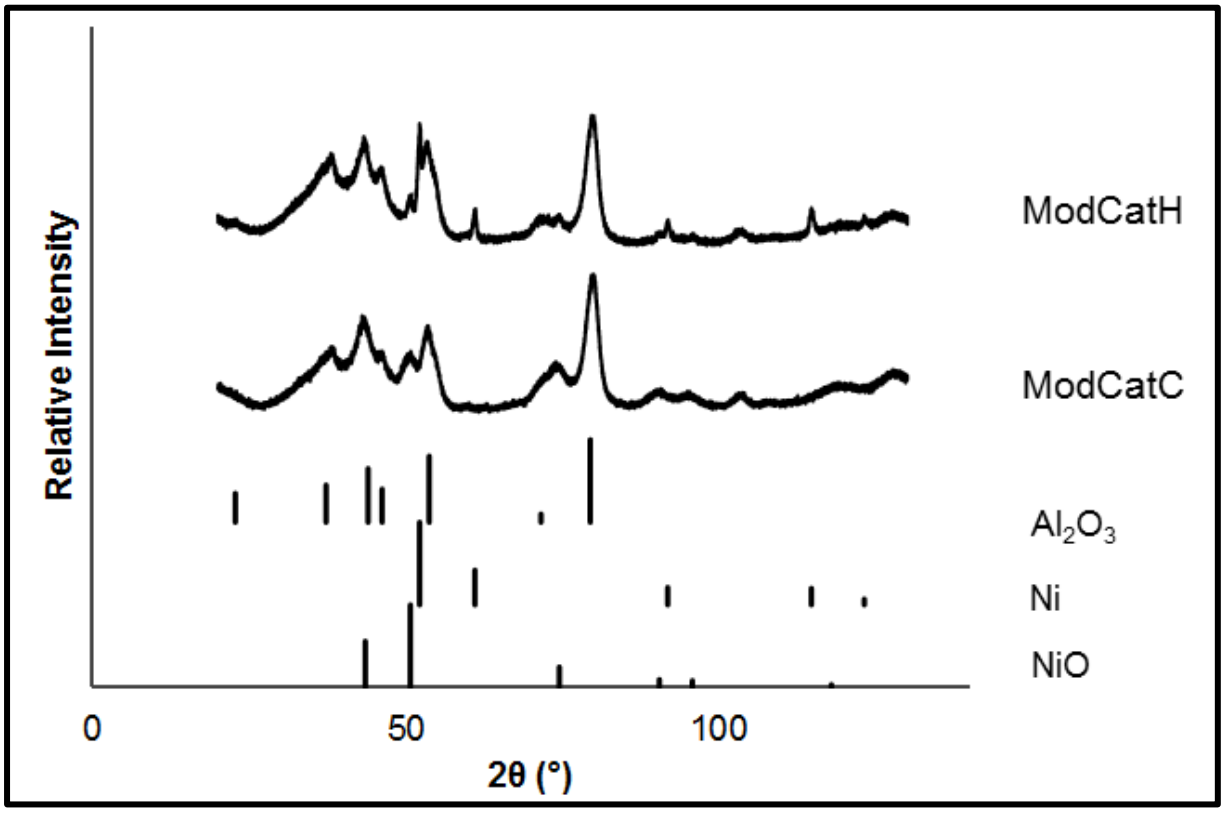

Figure 5.11. PXRD diffractograms of model catalysts

Table 5.6. Average crystallite size of model catalysts as determined from PXRD

Sample code	d_{NiO} (nm)	d_{Ni} (nm)	R_{wp}
ModCatC	5.3	-	8.7
ModCatH	12.3	34.5	8.6

5.3.1.2. TEM analysis of synthesised model catalysts

The TEM micrographs obtained for the model catalysts are depicted in Figure 5.12. From these micrographs it can be noted that the nanoparticles deposited on the support had a spherical morphology. The nanoparticles were also relatively well dispersed on the carrier as opposed to the severe clustering observed in Section 5.2. This suggests that decreasing the metal loading of the catalyst sample results in improved dispersion.

There was sufficient contrast between the metal nanoparticles and the support to allow for the determination of size distributions for the model catalysts (Figure 5.13) and the associated average particle sizes (Table 5.7).

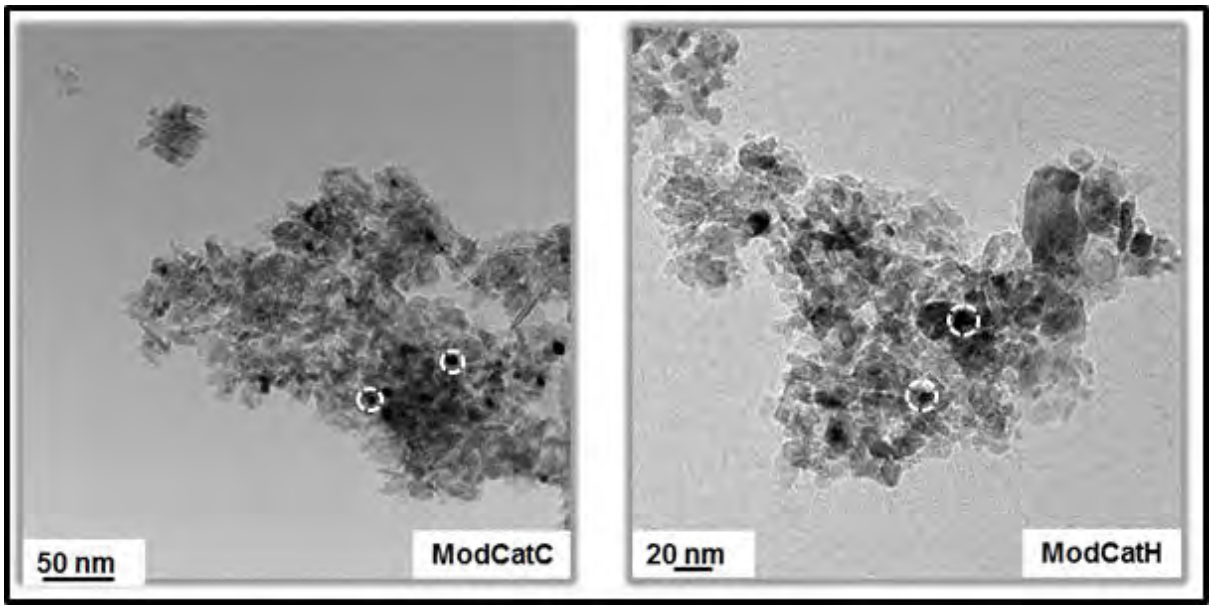

Figure 5.12. TEM micrographs of model catalysts

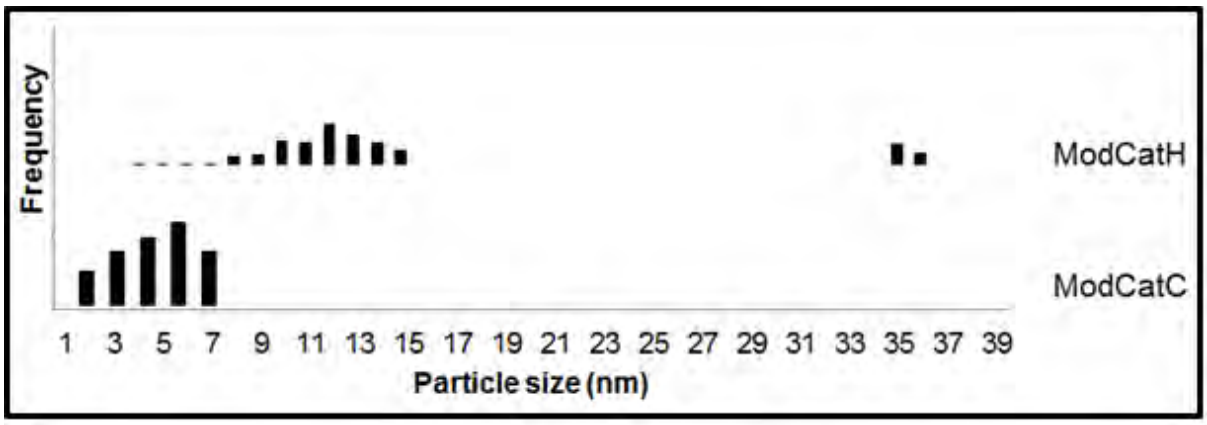

Figure 5.13. Size distributions for model catalysts as obtained from TEM analysis

Table 5.7. Average particle size (volume based) and standard deviation of model catalysts as obtained from TEM analysis

Sample code	ω^{i}	d_{NiO} (nm)	σ_{NiO} (nm)	d_{Ni} (nm)	σ_{Ni} (nm)
ModCatC	5/58	6.1	1.4	-	-
ModCatH	5/40	12.4	2.88	35.4	0.8

[i] water/surfactant ratio (g/g)

Both catalysts displayed a sufficiently narrow size distribution. The smaller particles had a far narrower distribution than the larger particles. This phenomenon was fully discussed in Section 5.1.2. ModCatH comprised of two different populations in terms of size. When considering the PXRD data described above, it could be hypothesised that the larger population is Ni.

Hence, model catalysts with sufficiently narrow size distributions were successfully synthesised. Two different sizes, required for the subsequent thermal sintering *in situ* investigations, were obtained.

5.3.2. AAS of model catalysts

The model catalysts were first digested in a mixture of acids. This was followed by AAS analysis in order to determine the metal content of the catalysts.

A metal content of 4.0 wt.% was required for the *in situ* magnetic study. In order to extract meaningful crystallite size data from magnetic measurements, it is important that crystallites are well distributed on the support in order to ensure that the crystallites behave as single domains. In an effort to improve dispersion on the model catalysts prepared according to Method 2, the metal loading was targeted at the relatively low amount of 4.0 wt.%.

Table 5.8. Metal loading of model catalyst samples

Sample code	Ni loading (wt.%)
ModCatC	4.29
ModCatH	4.32

The data in Table 5.8 again seems to indicate that preparation Method 2 (Section 4.2.2) allows for the achievement of accurate metal weight loadings.

5.3.3. *In situ* PXRD TPR

Prior to conducting a sintering study on the model catalysts, the supported NiO samples would have to be reduced to the catalytically active form of metallic Ni. However, in order to determine the conditions under which the catalysts were to be reduced, the precise reduction behaviour of the catalysts would have to be determined, and, as monitoring crystallite size changes is the cornerstone of the study, any size changes which may occur as a result of this reduction treatment would also have to be identified.

In order to determine the precise reduction behaviour of the model catalysts under investigation under the reduction conditions to be applied in the *in situ* magnetometer prior to sintering experiments, *in situ* PXRD TPR was conducted. The data obtained for the *in situ* PXRD TPR, in conjunction with TOPAS, allowed for the determination of any phase changes as well as any crystallite size changes, which then also allowed for the determination of the extent of any crystallite size growth during the reduction. The diffraction patterns obtained at each temperature during the reduction in hydrogen for both model catalysts are recorded in Figure 5.14, as well as the position of the characteristic peaks for nickel, nickel oxide and γ-alumina as given by ICDD database. The average crystallite size for the NiO and Ni during the activation of the model catalysts are recorded in Figure 5.15. ModCatH contained some nickel prior to reduction because the precursor nanoparticles contained a metallic nickel fraction. In order to deconvolute the size contribution of this nickel with the nickel formed as a result of the reduction of the NiO nanoparticles in the determination of average Ni crystallite size, a magnet was used to separate the two fractions of the supported material in order to obtain a small sample which was relatively free of metallic nickel. This then allowed for the investigation of any size changes induced as a result of the reduction conditions.

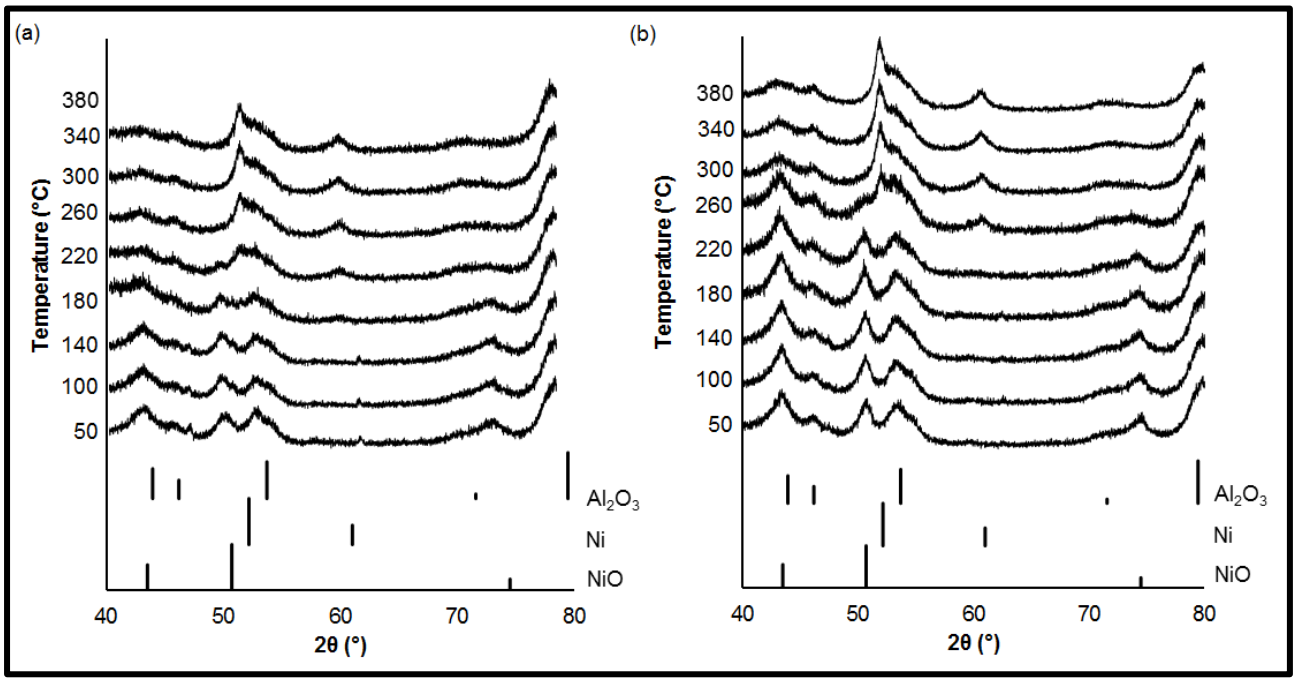

Figure 5.14. *In situ* PXRD TPR of model Ni catalysts (a) ModCatC (b) ModCatH

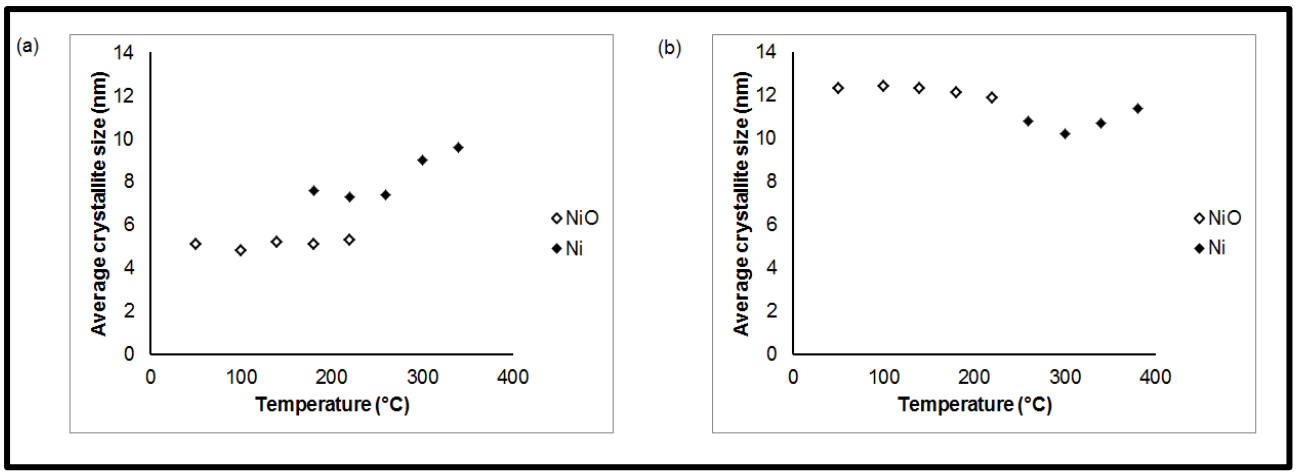

Figure 5.15. Average crystallite size (a) ModCatC (b) ModCatH during reduction using *in situ* PXRD

When considering Figure 5.14a, the first scan at 50 °C indicates a diffraction pattern which is dominated by the characteristic peaks of γ alumina. However, it is also possible to discern the characteristic nickel oxide peak. According to this scan, there was no Ni present in ModCatC at the start of the reduction. The scans recorded at 100 °C and 140 °C appeared to suggest that there was very little change in the relative intensity of the NiO peak. At 180 °C, there is a decrease in the relative intensity of the characteristic nickel oxide peak, as well as the emergence of a peak corresponding with the position of the characteristic nickel peak. At 220 °C, the nickel oxide peak was almost indiscernible whilst the intensity of the nickel peak had slightly increased. The scan at 260 °C shows no peak at the characteristic nickel oxide peak position. The nickel peak increased significantly in intensity. A further increase in the intensity of the Ni peak was observed at 300 °C and 340 °C.

Figure 5.14b is a collection of the scans obtained during the reduction of model catalyst ModCatH. At 50 °C, a strong characteristic NiO peak is observed, despite the dominance of the γ alumina. There is also some Ni present in the sample. However, the characteristic Ni peak has a very slight intensity. The relative intensities of the nickel oxide peaks remain fairly constant from 100 °C to 180 °C. At 220 °C, there is a slight decrease in the relative intensity of the characteristic nickel oxide peak. 260 °C sees the emergence of a characteristic nickel peak whilst the characteristic nickel oxide peak is now almost indiscernible. At 300 °C there is no

nickel oxide peak and the nickel peak has increased in relative intensity. There was then a slight increase in the relative intensity of the Ni peak at 340 °C and 380 °C.

The data from Figure 5.14a seems to indicate that the conversion of nickel oxide to nickel started between 140 °C and 180 °C and was fully reduced by 260 °. Figure 5.14b in turn indicate that the reduction of ModCatH commenced between 220 °C and 260 °C and was fully reduced at 300 °C. This seems to suggest that the catalyst sample consisting of smaller particles was easier to reduce than the model catalyst containing larger particles.

According to the size data recorded in Figure 5.15, the size of the resultant nickel crystallites which first appear at 180 °C were larger than the precursor nickel oxide nanocrystallites suggesting that there was some growth of the particles during the reduction step. Further growth was observed at 300 °C. Figure 5.15b indicates that the nickel which first appears is smaller than the NiO nanocrystallites, as to be expected upon the conversion of nickel oxide to nickel. Some growth was then observed for each subsequent scan as the reduction proceeded to 380 °C. In order to expose the model catalysts to the same pre-treatment conditions, 250 °C was chosen as the most appropriate reduction temperature. This temperature was both high enough to reduce the larger crystallites, whilst also being low enough to prevent extensive growth of the smaller crystallites.

5.3.4. *In situ* magnetic measurements for model catalysts

5.3.4.1. Reduction

Prior to sintering tests, ModCatC and ModCatH were reduced in the *in situ* magnetometer. The model catalysts were reduced at 250 °C in hydrogen, with a hold time of 80 minutes. After reduction the samples were cooled to room temperature under argon. This reduction and subsequent cooling is represented in Figure 5.16. Fresh ModCatC (Figure 5.16a) did not have any metallic Ni present. Hence, when heating ModCatC in hydrogen, no magnetic signal was observed initially. At 215 °C, the signal starts to increase, indicating the commencement of the conversion of nickel oxide to nickel. This signal continues to increase until it stabilises at the end of

the reduction. When ModCatC was cooled to room temperature after reduction, the signal had increased significantly. The paramagnetic nickel was reduced to ferromagnetic nickel.

ModCatH (Figure 5.16b) contained a fraction of nickel nanoparticles thus, at the beginning of the reduction, the signal was already significantly higher than that observed at the beginning of the reduction of ModCatC. At 220 °C, the signal starts to steadily increase, indicating the conversion of NiO to metallic Ni. The signal continues to increase until 250 °C. On cooling, the signal is higher than at the beginning of the reduction, confirming the conversion of nickel oxide to nickel.

This extent of the reduction as depicted in Figure 5.16 is quantified in Table 5.9 as degree of reduction (DOR). DOR was determined by making use of the calibration data recorded in Appendix A where a known mass of bulk nickel oxide was reduced. The DOR for ModCatH was determined by first considering the fraction of the sample which was present as metallic nickel prior to reduction. This ensured that the DOR was based only on the nickel oxide converted to nickel during the reduction process, allowing for a more accurate comparison between the DOR of the two model catalysts. According to the data in Table 5.9, the DOR for ModCatC was 77 % and 93 % for ModCatH. This suggests that ModCatH, under the same conditions, reduced to a greater extent than ModCatC. From the *in situ* PXRD TPR data (Section 5.3.3), it originally appeared as though ModCatC was easier to reduce than ModCatH.

Table 5.9. DOR for model catalysts after reduction at 250 °C

Sample code	DOR (%)
ModCatC	77
ModCatH	93

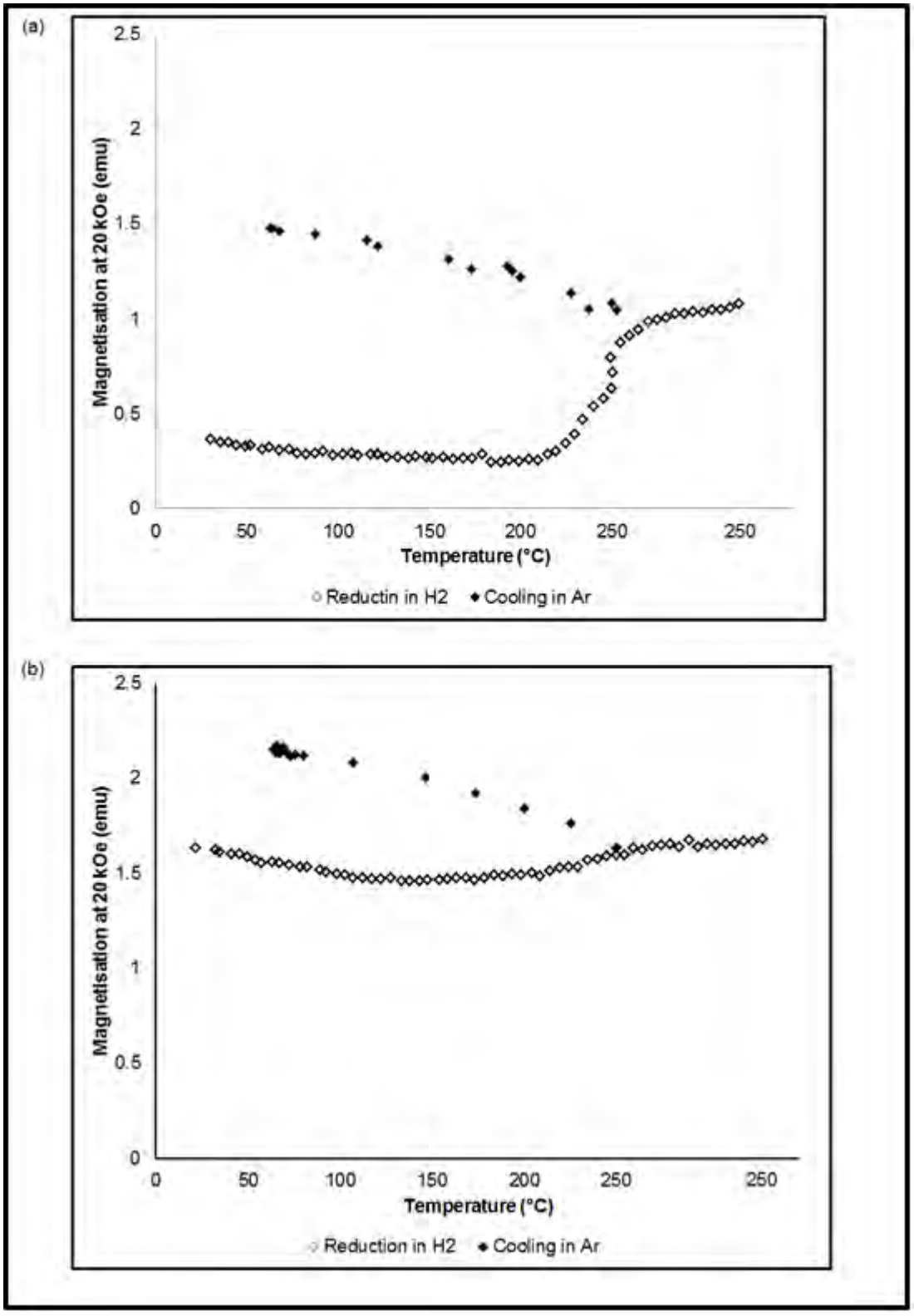

Figure 5.16. *In situ* reduction of model catalysts (a) ModCatC (b) ModCatH

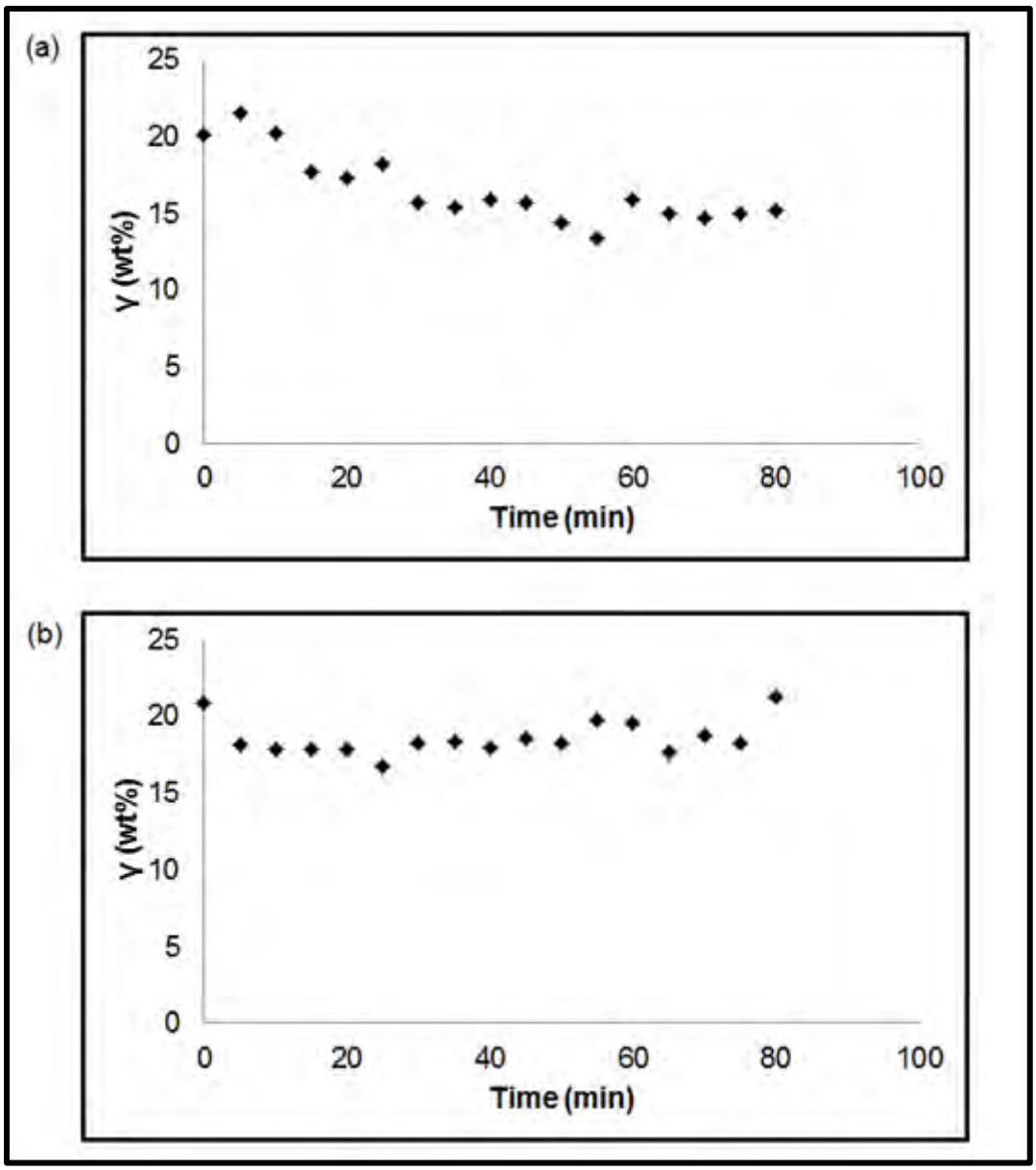

Figure 5.17. Weight percentage of nickel displaying remnant magnetisation during 80 minute holding time at 250 °C during reduction in H_2 for model catalysts (a) ModCatC and (b) ModCatH

Figure 5.17 is a representation of the percentage of ferromagnetic material, which can be used as semi-quantitative indicator of the amount of material in the ferromagnetic size regime. For both catalysts, this percentage remained fairly constant throughout this reduction, indicating that there was no extensive crystallite size change during this process.

5.3.4.2. Thermal sintering tests in an inert atmosphere

In order to investigate the effects of elevated temperature on particle sintering, the model catalysts were exposed to different temperatures for one hour, under argon. During these thermal sintering tests, magnetic readings were taken at 20 kOe and 0 kOe every 5 minutes. The magnetic data obtained during each test are recorded in Figure 5.18, as well as the Curie temperature for bulk Ni as given by Serway & Jewett, Jr. (2014). Hysteresis measurements were also recorded after each temperature test. This hysteresis data is recorded in Appendix B. The hysteresis data, when used in conjunction with the Langevin equation (Equation 8), was used in order to extract crystallite size distribution data (Appendix D). The crystallite size distribution data obtained after each subsequent temperature test for both model catalysts are recorded in Figure 5.19.

What Figure 5.18 seems to indicate is that the magnetisation of both samples was dependent on temperature: as temperature increased, the magnetisation decreased. This confirmed the work conducted by Amekura, *et al*. (2005) who suggested that the saturation magnetisation of nanoparticles decreases with temperature (Amekura, *et al*., 2005). This

The data recorded in Figure 5.18 also allows for a determination of the Curie temperature of the model catalyst samples, which is the point at which the material is no longer magnetic. For both samples, no signal was observed at temperatures greater than 420 °C. This temperature is much higher than the Curie temperature of bulk nickel. However, Amekura, *et al*. (2005) have suggested that superparamagnetic nickel nanoparticles, such as those under investigation in this study, will retain some magnetisation even above the Curie temperature of the bulk material.

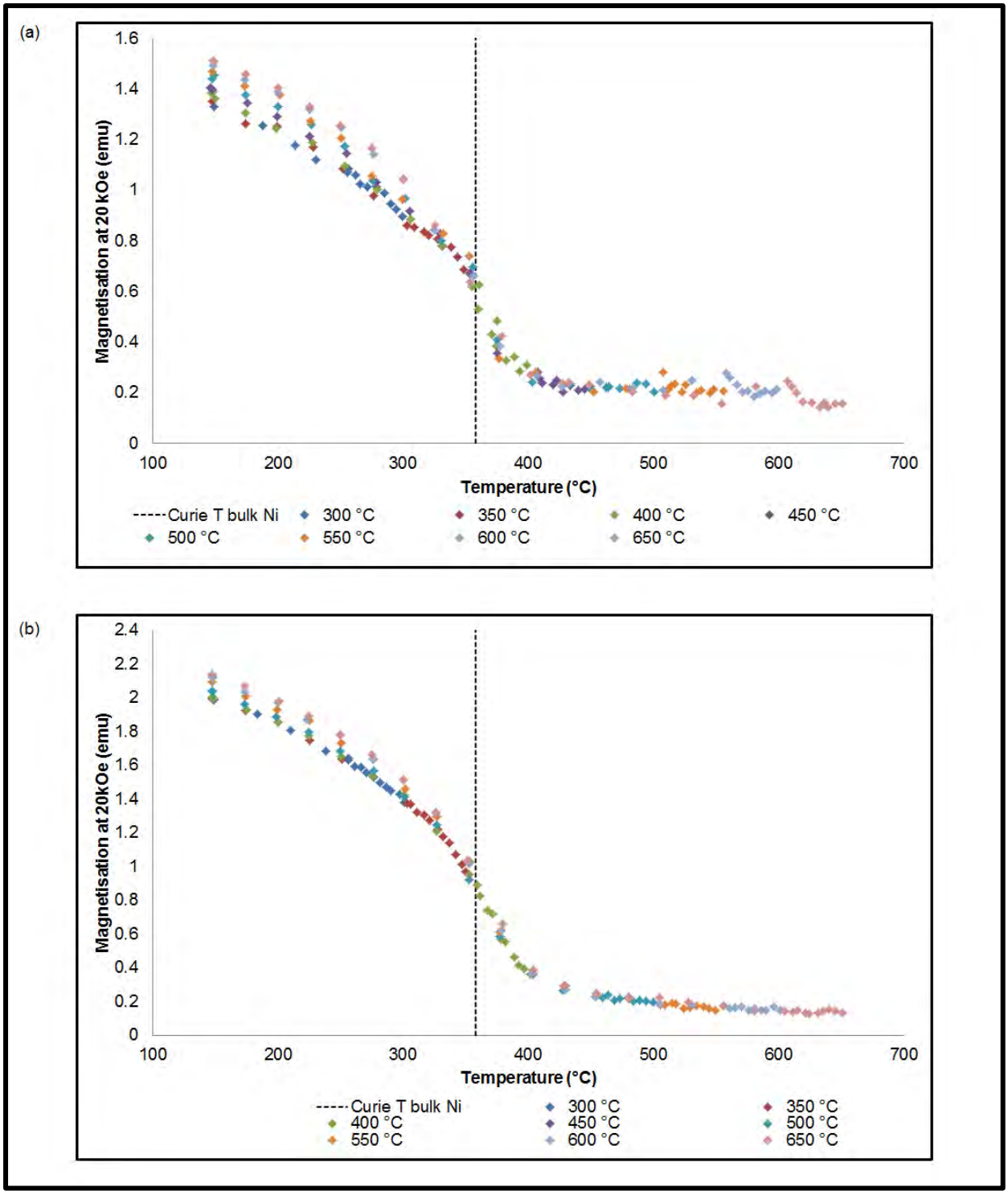

Figure 5.18. Magnetisation data at 20 kOe for model catalysts (a) ModCatC (b) ModCatH during thermal sintering investigation in an inert atmosphere

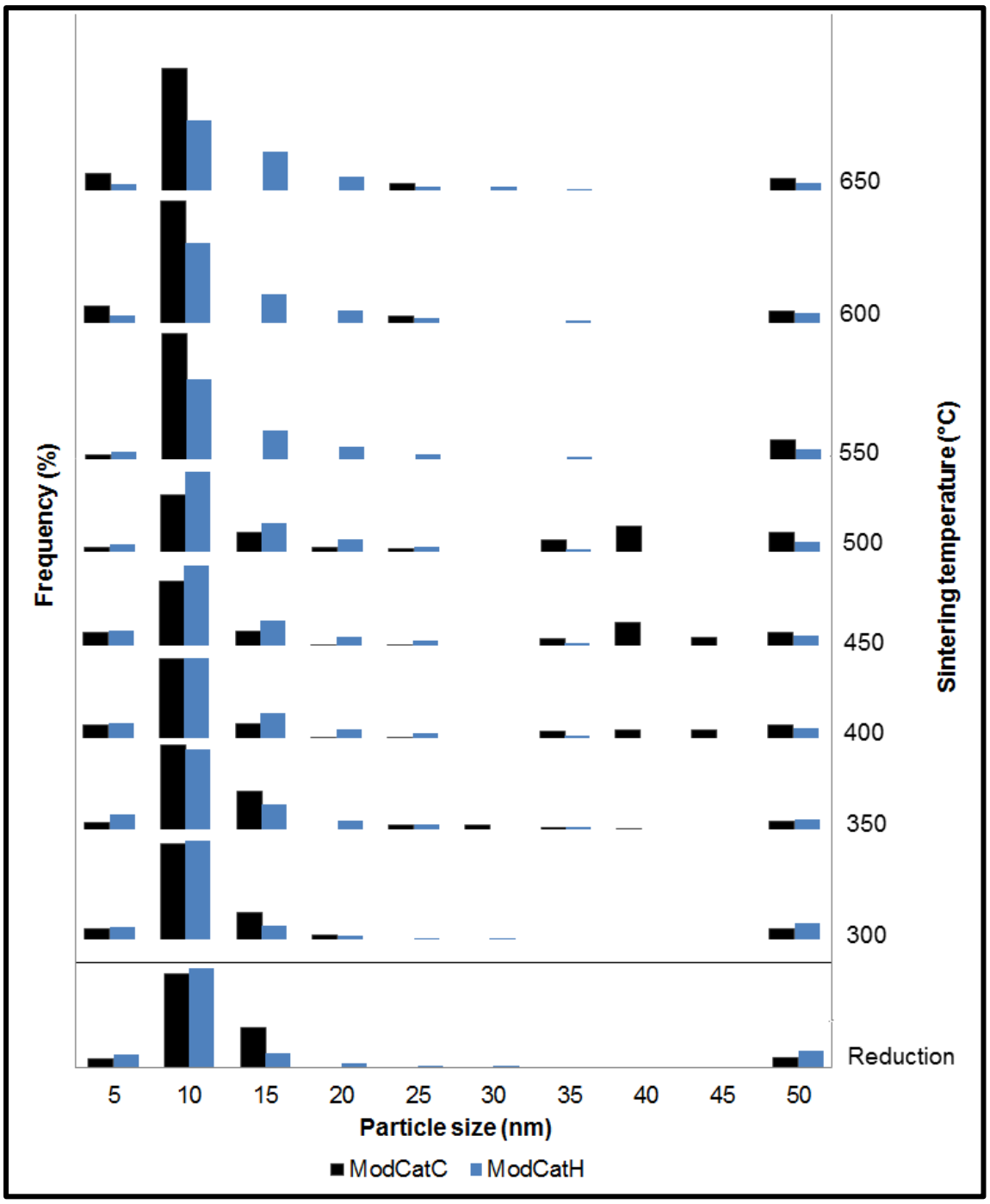

Figure 5.19. Size distribution data from *in situ* magnetometer for model catalysts after thermal sintering tests in an inert atmosphere

Figure 5.19 contains the size distribution data obtained during the thermally induced sintering tests for model catalysts ModCatC and ModCatH, as determined using the Langevin equation (Appendix D). After reduction, both catalysts displayed similar distributions with crystallites below 15 nm. This indicates that ModCatC, which had a

distribution for nickel oxide nanoparticles centred at 5 nm prior to reduction, sintered to a fairly large extent. Conversely, ModCatH was far more stable. There was only a slight shift in the size distribution during reduction. Despite the fact that both catalysts had similar size distributions after reduction, they exhibited different sintering behaviour with ModCatC showing a greater tendency for crystallite growth than ModCatH. During the thermal sintering, ModCatH again displayed superior stability. There was a minor widening in the size distribution to larger sizes during sintering tests and a very large fraction of crystallites remained less than 30 nm and centred at 15 nm. The size distribution for ModCatC, however, widened to larger crystallite sizes from 300 °C to 500 °C, indicating crystallite size growth. However, after 550 °C, the size distribution seems to indicate that all the particles in the catalyst sample are centred at 10 nm, suggesting that there was a significant decrease in crystallite size after exposure to 500 °C. However, when considering TEM (Figure 5.28b) and STEM (Figure 5.29a) images, it can be noted that ModCatC experienced particle size growth with a number of particles larger than the critical size of nickel (55 nm). There also appeared to be severe clustering of the particles on the carrier. The Langevin equation, used in the determination of crystallite size distributions, only applies for superparamagnetic particles below this critical size. Hence, the size distribution observed is for the fraction of superparamagnetic material remaining in the sample and is no longer a true representation of the entire sample. Furthermore, the clustering of the particles means that the particles no longer behave as single domains and may start to assume the behaviour of bulk nickel.

By considering the data from both Figure 5.18 and Figure 5.19, some tentative conclusions could be drawn on whether the Curie temperature is affected by crystallite size. According to this work, changes in crystallite size did not have an effect on the observed Curie temperature. There is some ambiguity as to the effect of crystallite size on the Curie temperature. Derouane, *et al*. (1978) found that the Curie point of dispersed Ni particles was not dependent on crystallite size for particles larger than 2.5 nm. Particles smaller than this may exhibit a slightly higher Curie temperature. In contrast, Nepijko & Wiesendanger (1995) and He & Shi (2012) reported a strong dependence of the Curie temperature on the crystallite size where the Curie temperature of the nickel nanoparticles decreases with crystallite size.

The hysteresis data was used to give a qualitative indication of crystallite growth. An increase in hysteresis behaviour is an indication of an increase in the amount of ferromagnetic material. The area between – 1 kOe and 1 kOe was considered in order to adequately compare the hysteresis behaviour of the catalysts after being exposed to different conditions. Figure 5.20 contains the hysteresis data recorded for the model catalysts. For both catalysts, the hysteresis behaviour remained fairly constant from after reduction to after the thermal sintering tests in an inert atmosphere. This indicates that there was not a significant increase in the amount of ferromagnetic material.

The magnetisation data, recorded at the maximum field strength of 20 kOe at various temperatures after reduction and after the thermal sintering tests conducted in an inert atmosphere is recorded in Figure 5.21. According to Figure 5.21 the magnetisation of ModCatC and ModCatH increased from after reduction to after the sintering tests. The DOR also increases for both catalysts from 77 and 93 % (Table 5.9) to 82 and 100 % (Table 5.10) for ModCatC and ModCatH, respectively. This indicates that some of the nickel oxide which remained unreduced after reduction was converted to metallic nickel during the sintering tests. This is unexpected as the thermal sintering tests were conducted in argon, a non-reducing atmosphere.

Table 5.10. DOR for model catalysts after thermal sintering tests in an inert atmosphere

Sample code	DOR (%)
ModCatC	82
ModCatH	100

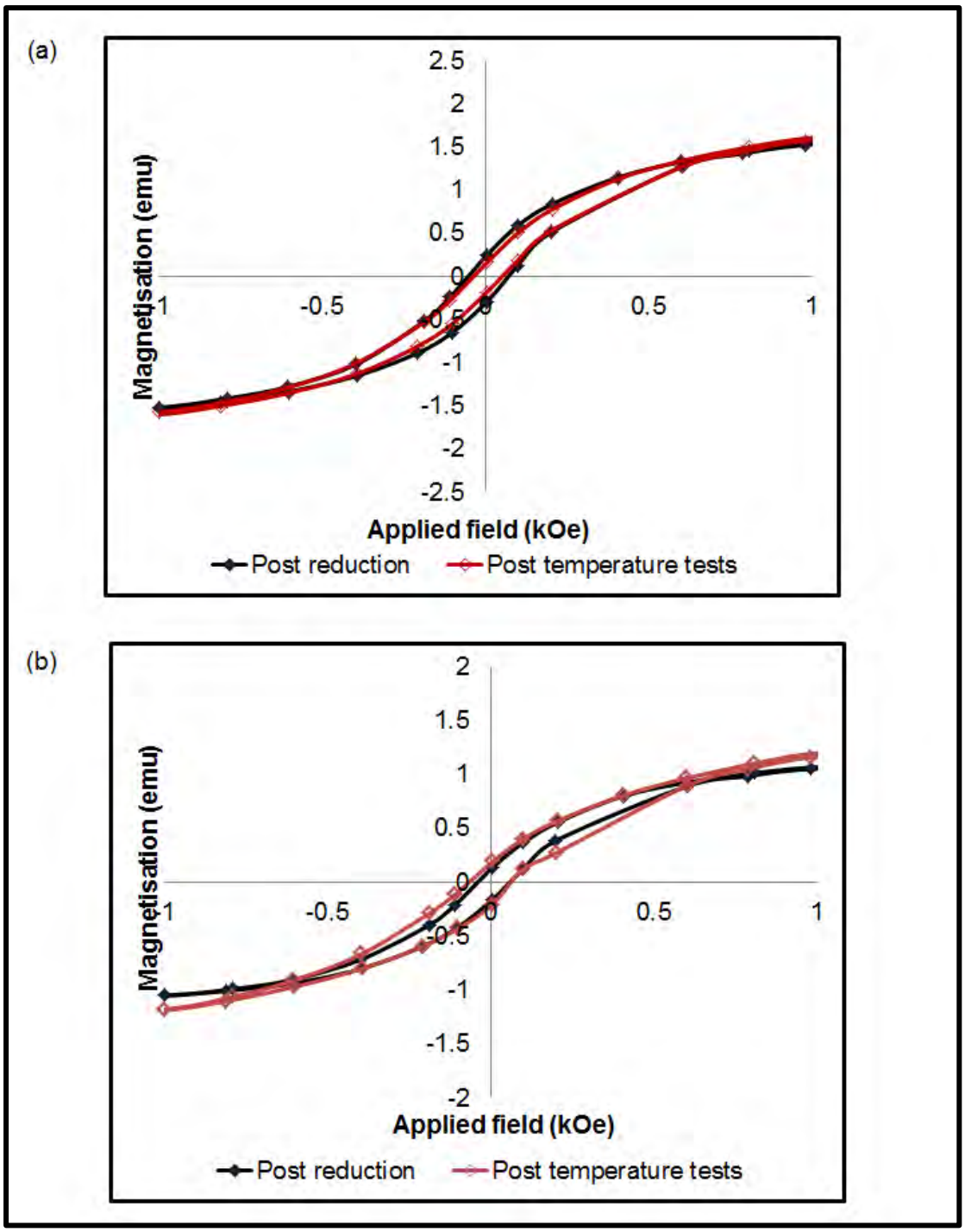

Figure 5.20. Hysteresis data recorded at 150 °C in Ar after reduction and thermal sintering tests in an inert atmosphere for (a) ModCatC and (b) ModCatH

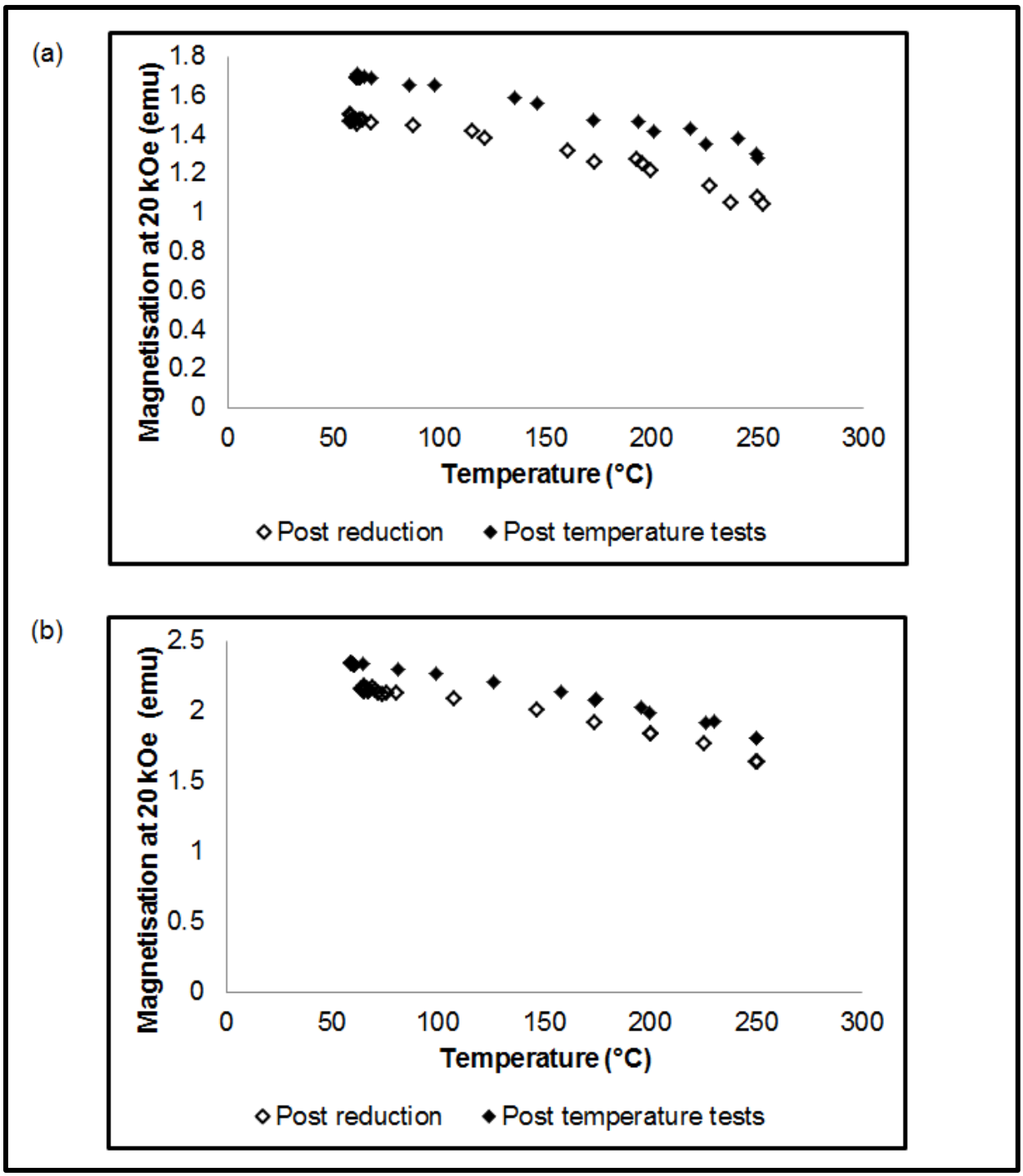

Figure 5.21. Magnetisation data at 20 kOe for model catalysts (a) ModCatC (b) ModCatH after reduction and after thermal sintering tests in an inert atmosphere

5.3.4.3. Thermal sintering tests in a steam/hydrogen atmosphere

The additional effect of water vapour on thermally induced particle growth was also investigated by exposing the model catalysts to water vapour. The reactor was operated at 10 bar and a condition of $P_{H_2O}/P_{H_2} = 5$ was maintained for the sintering tests at each temperature. During each water co-feed sintering test, magnetic measurements of the samples were taken at 20 kOe and 0 kOe.

Figure 5.22 contains the magnetisation data recorded at 20 KOe for the model catalysts during the thermal sintering in a steam and hydrogen atmosphere. The magnetisation of both samples was dependent on temperature: as temperature increased, the magnetisation decreased. The samples again retained some magnetisation beyond the Curie temperature of bulk nickel. The magnetisation of ModCatC (Figure 5.22a) decreased between sintering tests for 350 °C and 450 °C. A decrease in the magnetisation is indicative of the conversion of the metallic Ni into a non-metallic form. Reoxidation of the metal to NiO may have taken place. Nickel aluminates may also have formed.

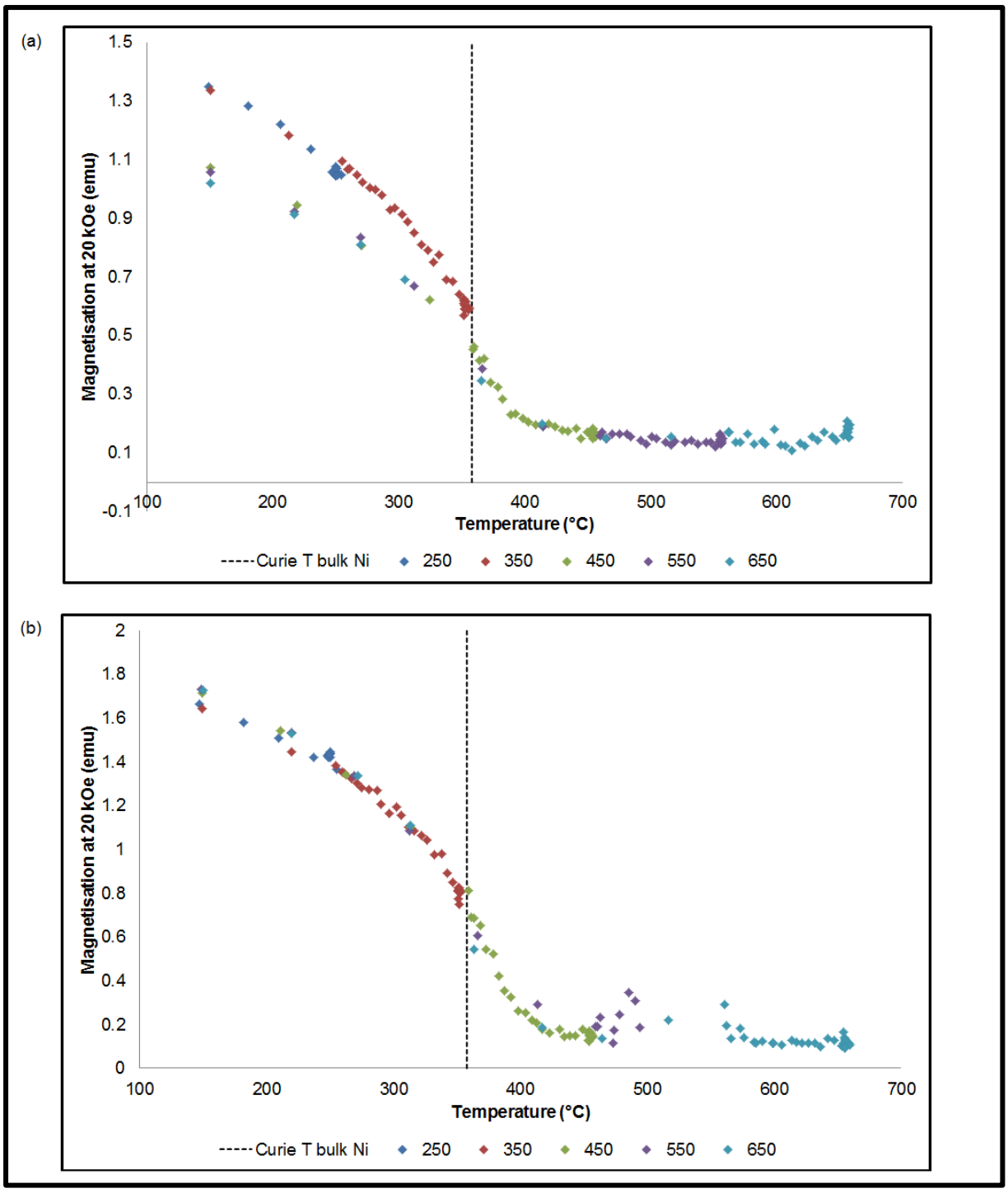

Figure 5.22. Magnetisation data at 20 kOe for model catalysts (a) ModCatC (b) ModCatH during thermal sintering investigation in a steam/hydrogen atmosphere

In order to again use the Langevin equation for size determination (Appendix D), hysteresis data was collected after each water co-feed test (Appendix B). This size data is summarised in Figure 5.23.

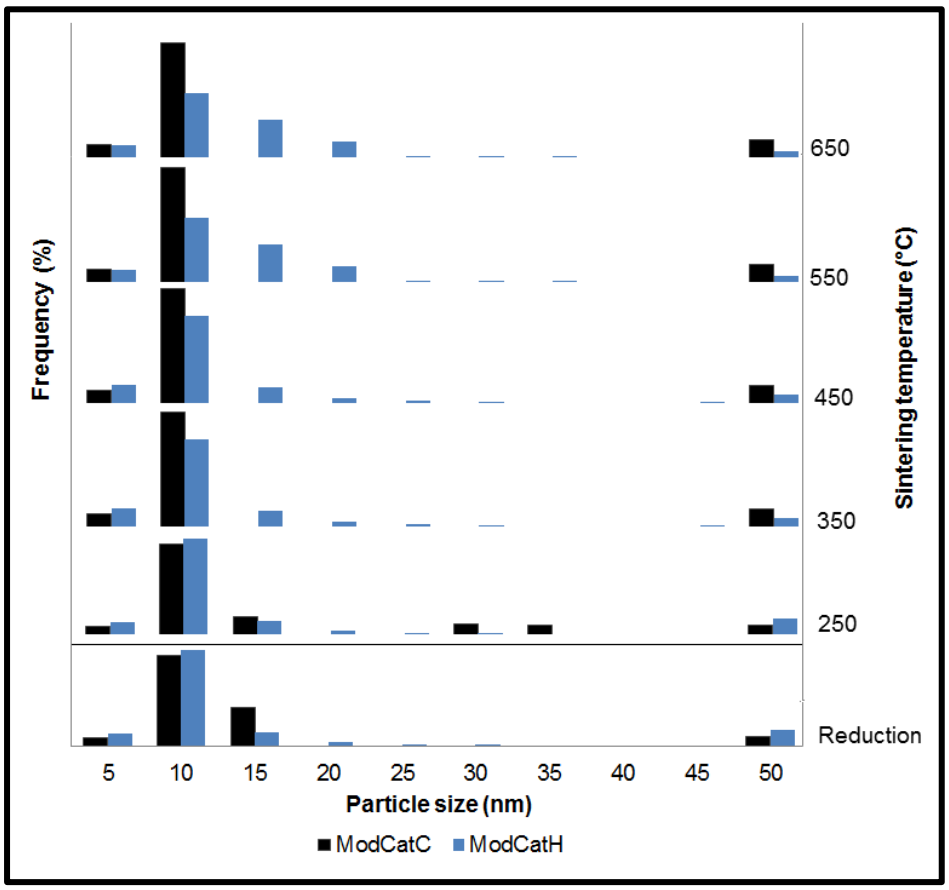

Figure 5.23. Size distribution data from *in situ* magnetometer for model catalysts after thermal sintering in a steam/hydrogen atmosphere

From Figure 5.23 it can be seen that there was a slight widening of the size distribution for ModCatH as sintering tests proceeded. The extent of this widening of the size distribution is greater than that observed during the sintering tests in an inert atmosphere, suggesting that water vapour exacerbated the sintering process at elevated temperatures. ModCatH is, however, still fairly stable with a large fraction of crystallites remaining below 20 nm.

The crystallite size increases observed in ModCatH were not as marked as those observed for ModCatC. When considering the data for ModCatC, size distribution data was obtained only at 250 °C, beyond which it is postulated that extensive sintering took place resulting in a skewed size distribution which did not reflect the true crystallite size. This is again because the crystallites no longer displayed superparamagnetic behaviour and the Langevin equation could not be used successfully to determine crystallite size.

The hysteresis data can be used as a qualitative indication of sintering. An increase in hysteresis behaviour is an indication of an increase in the amount of ferromagnetic material. Figure 5.24 contains the hysteresis data recorded for the model catalysts. ModCatC (Figure 5.24a) showed a decrease in the magnetisation, indicating that some of the metallic nickel was converted to a non-magnetic form during the thermal sintering tests in steam and hydrogen atmosphere. There was also a slight increase in hysteresis behaviour, suggesting that the amount of ferromagnetic material in the sample increased. ModCatH (Figure 5.24b) showed fairly constant magnetisation after being exposed to different conditions. There was however a discernible increase in the hysteresis behaviour after exposure of the catalyst to a steam and hydrogen atmosphere. The amount of ferromagnetic material increased, indicating crystallite growth.

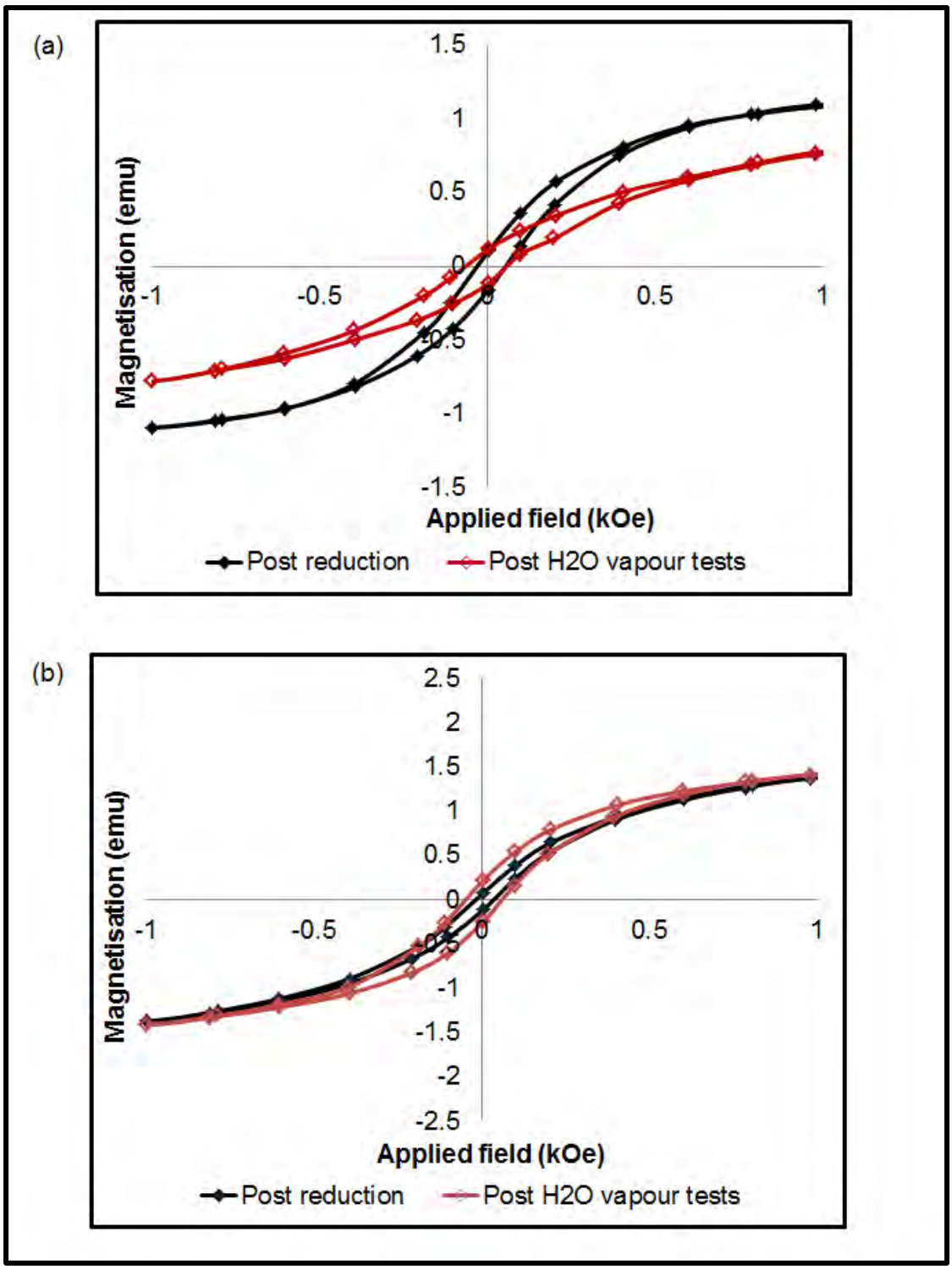

Figure 5.24. Hysteresis data recorded at 150 °C in Ar after reduction and thermal sintering tests in a steam/hydrogen atmosphere for (a) ModCatC and (b) ModCatH

Figure 5.25 contains the magnetisation as a function of temperature curves for the model catalysts after reduction and after thermal sintering tests in a steam and hydrogen atmosphere. This data can be used to determine the extent to which the catalysts may have reoxidised during thermal sintering tests in water vapour and hydrogen atmosphere.

According to Figure 5.25a, the magnetisation after the thermal sintering tests conducted in a steam and hydrogen atmosphere for ModCatC was lower than after reduction and the DOR also decreased from 77 % after reduction to 59 % after exposure to steam and hydrogen (Table 5.11). This confirms that some of the nickel was converted to a form which was not magnetic i.e. nickel oxide or nickel aluminate. ModCatH (Figure 5.25b) showed no changes in the magnetisation between reduction and after the sintering tests in a steam and hydrogen atmosphere. There was, in fact, a slight increase in the DOR (Table 5.11). This again confirms that ModCatH displayed greater stability than ModCatC.

Table 5.11. DOR for model catalysts after thermal sintering tests in a steam and hydrogen atmosphere

Sample code	DOR (%)
ModCatC	59
ModCatH	95

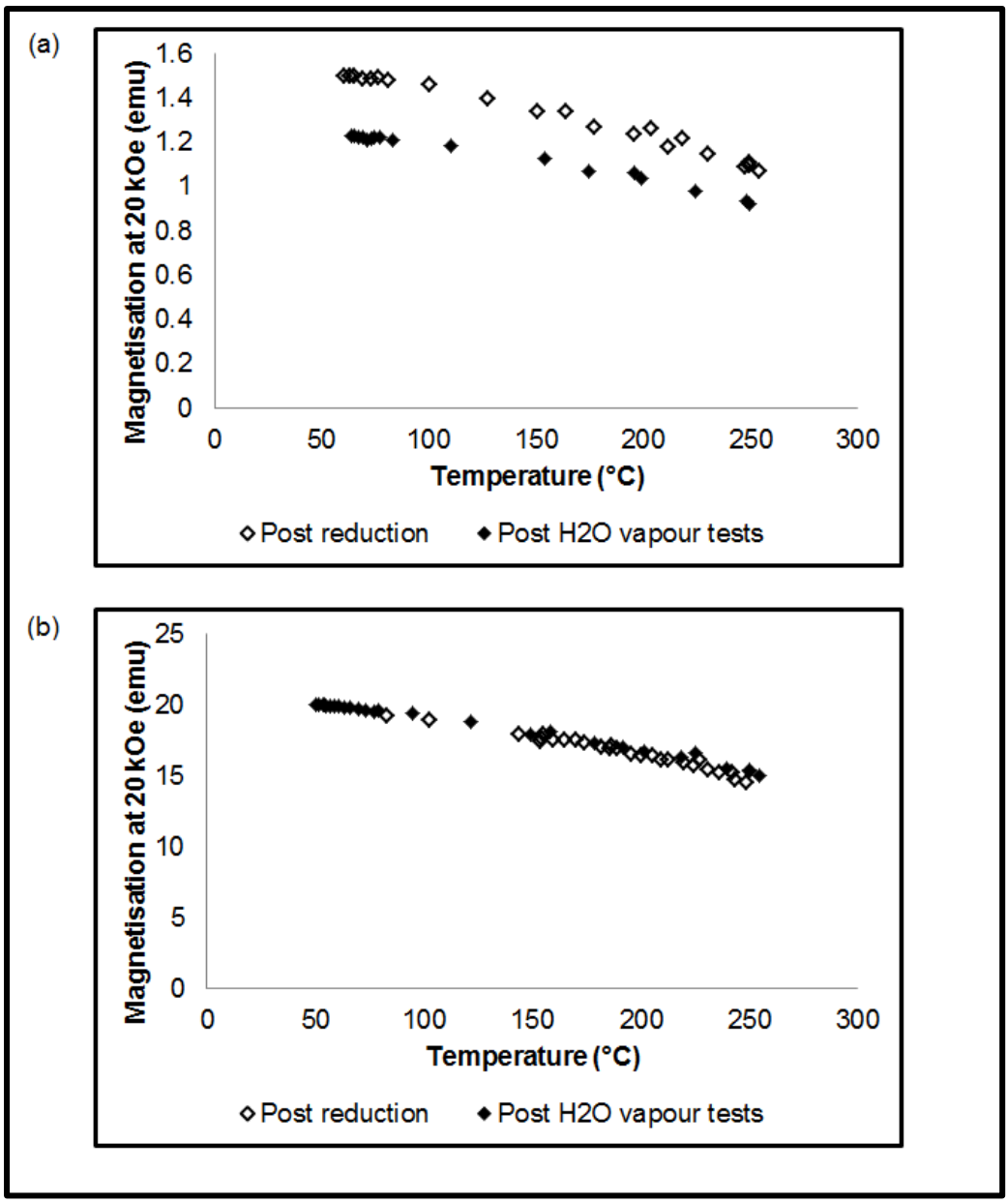

Figure 5.25. Magnetisation data at 20 kOe for model catalysts (a) ModCatC (b) ModCatH after reduction and after thermal sintering tests in a steam/hydrogen atmosphere

According to the size distribution data obtained for ModCatC and ModCatH, it appears that ModCatH, which was prepared using larger nickel oxide nanoparticles, was the more thermally stable catalyst. This correlates with the work conducted by, Munnik, *et al*. (2014), who found that small particles grew to a excessively large extent whilst larger particles displayed superior stability. Munnik, *et al*. (2014) propose that this may be because slightly larger particles remain confined by the pores of the support.

5.3.5. PXRD analysis of model catalysts

The model catalysts, the externally reduced and passivated catalyst samples as well as the spent catalyst samples after sintering tests were characterised using PXRD. The average crystallite size was determined as well as the phases present in the samples. The diffraction patterns from each model catalyst after exposure to different conditions are displayed in Figure 5.26 and Figure 5.27 for ModCatC and ModCatH respectively.

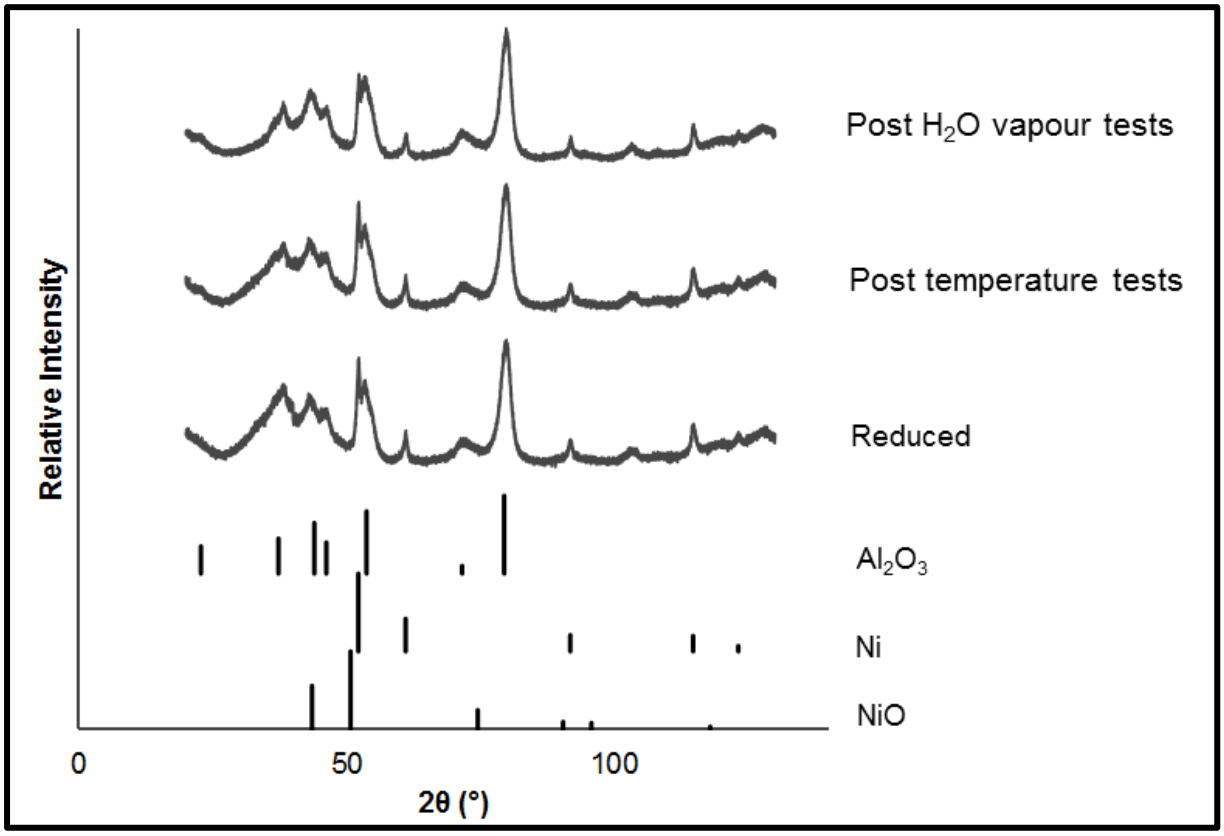

Figure 5.26. PXRD diffractograms of model Ni catalyst ModCatC

The diffractograms for the samples after reduction and thermal sintering tests in an inert and water and hydrogen atmosphere show characteristic nickel peaks. From the magnetic results, it was suspected that there may have been a phase transformation of the reduced metallic nickel to non-magnetic nickel oxide or nickel aluminate. However, from the diffraction pattern of ModCatC, there was no indication of these phases. Perhaps the relative amounts were too small to be observed in the

pattern which was significantly dominated by the diffraction pattern of the carrier, γ-alumina.

The average crystallite sizes obtained from these diffraction patterns using TOPAS are recorded in Table 5.12. After reduction, ModCatC had an average crystallite size of 14.5 nm. After sintering tests in an inert atmosphere and steam and hydrogen atmosphere, this average crystallite size increased to 18.6 nm and 21.8 nm respectively. These crystallite sizes were, however, not indicative of the extreme crystallite size growth observed in ModCatC. There may have been some unidentified phases in the catalyst samples which were not accounted for during Rietveld refinement in TOPAS, leading to inaccurate results.

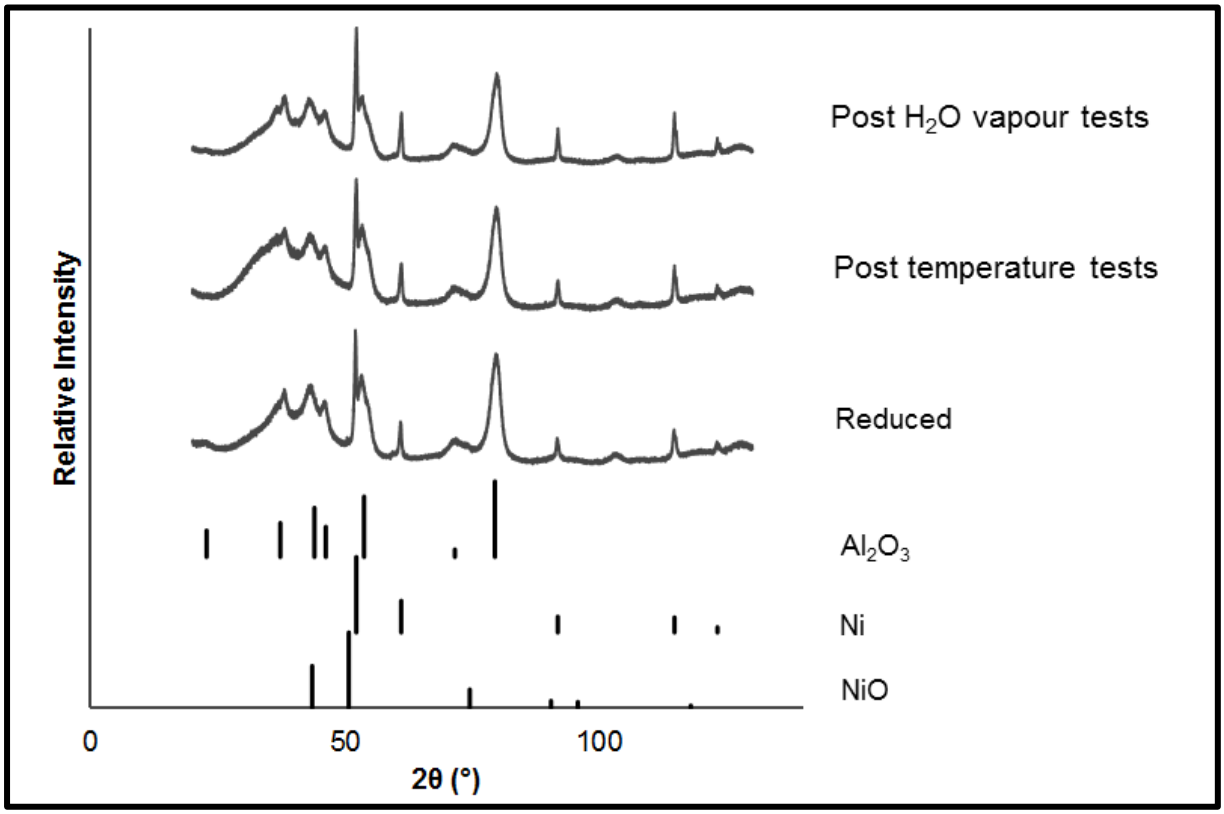

Figure 5.27. PXRD diffractograms of model Ni catalyst ModCatH

Figure 5.27 indicates that the diffraction pattern of the γ-alumina was again particularly dominant. However, very distinctive nickel peaks were observed for all samples. For this model catalyst, PXRD was not particularly useful. An average

crystallite size of the nickel is obtained for the spent catalyst sample. However, this average includes the very large nickel particles which were already present before sintering tests. No conclusions could be drawn from this data.

Table 5.12. Average crystallite sizes of model catalysts after exposure to different conditions as determined from PXRD

Sample code	d_{Ni} (nm)		
	Reduced	Sintering inert atmosphere	Sintering H_2O/H_2 atmosphere
ModCatC	14.5	18.6	21.8
ModCatH	34.9	32.1	34.6

5.3.6. TEM analysis of model catalysts

The model catalysts which were reduced and exposed to different conditions in the sintering study were characterised using TEM analysis. This allowed for the determination of the average particle size of nickel as well as the size distribution. The morphology of the particles after being exposed to different conditions could also be considered.

Figure 5.28 and Figure 5.30 contain the TEM micrographs obtained for the model catalysts ModCatC and ModCatH, respectively, after reduction and after sintering tests. Depicted in Figure 5.29 and Figure 5.31 are the STEM images obtained for the model catalysts after sintering tests. ModCatC and ModCatH had particles which were spherical in shape. From the aforementioned figures, it can be seen that after reduction, the particles were still spherical in nature. There were, however, areas of good dispersion and areas where the particles were poorly distributed. After temperature tests, no extensive growth of particles was observed. However, after exposure to water vapour, both catalysts sintered extensively, particularly ModCatC.

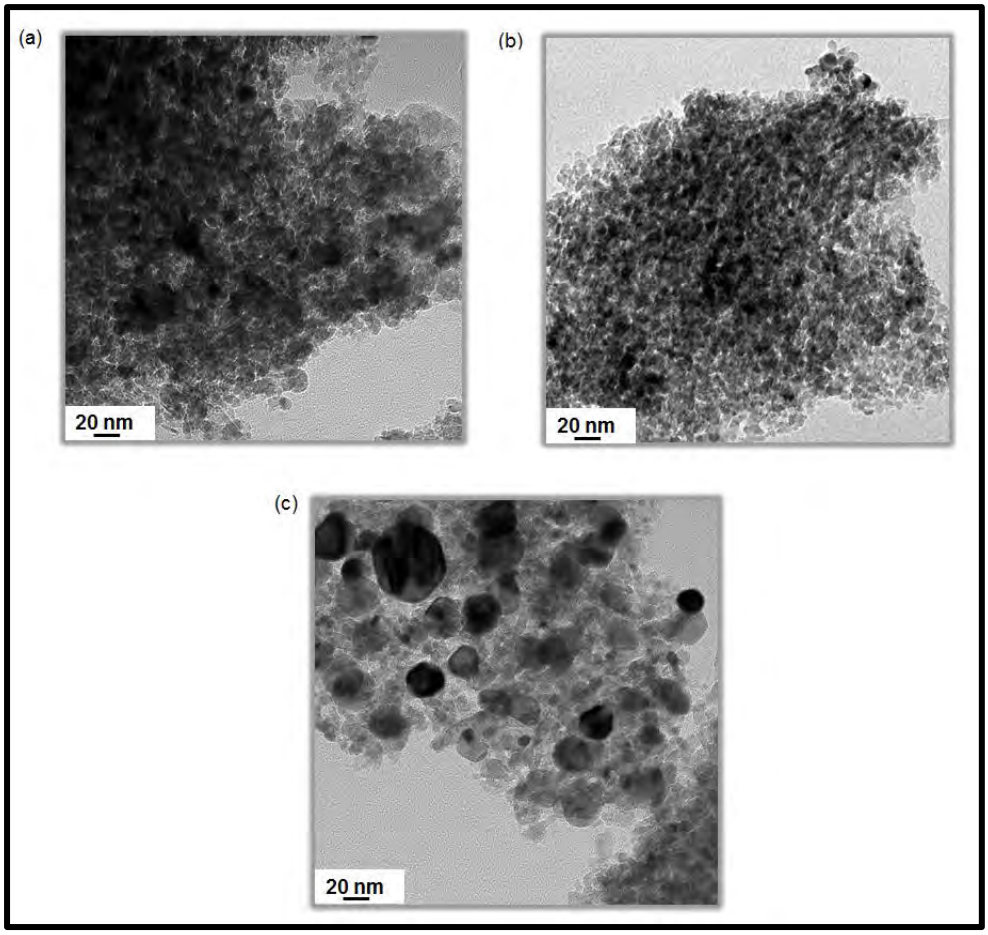

Figure 5.28. TEM micrographs model Ni catalyst ModCatC (a) post reduction (b) post sintering tests in an inert atmosphere (c) post sintering tests in a steam/hydrogen atmosphere

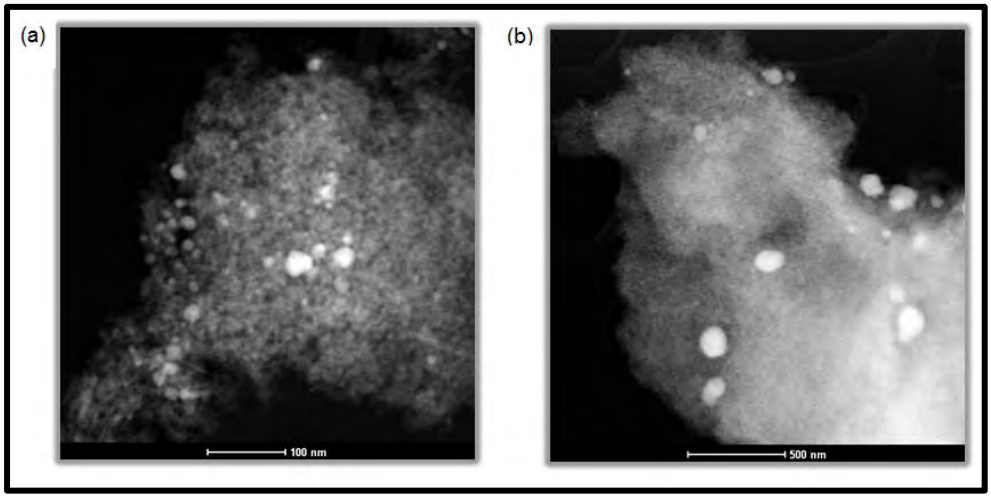

Figure 5.29. STEM micrographs model Ni catalyst ModCatC (a) post sintering tests in an inert atmosphere (b) post sintering tests in a steam/hydrogen atmosphere

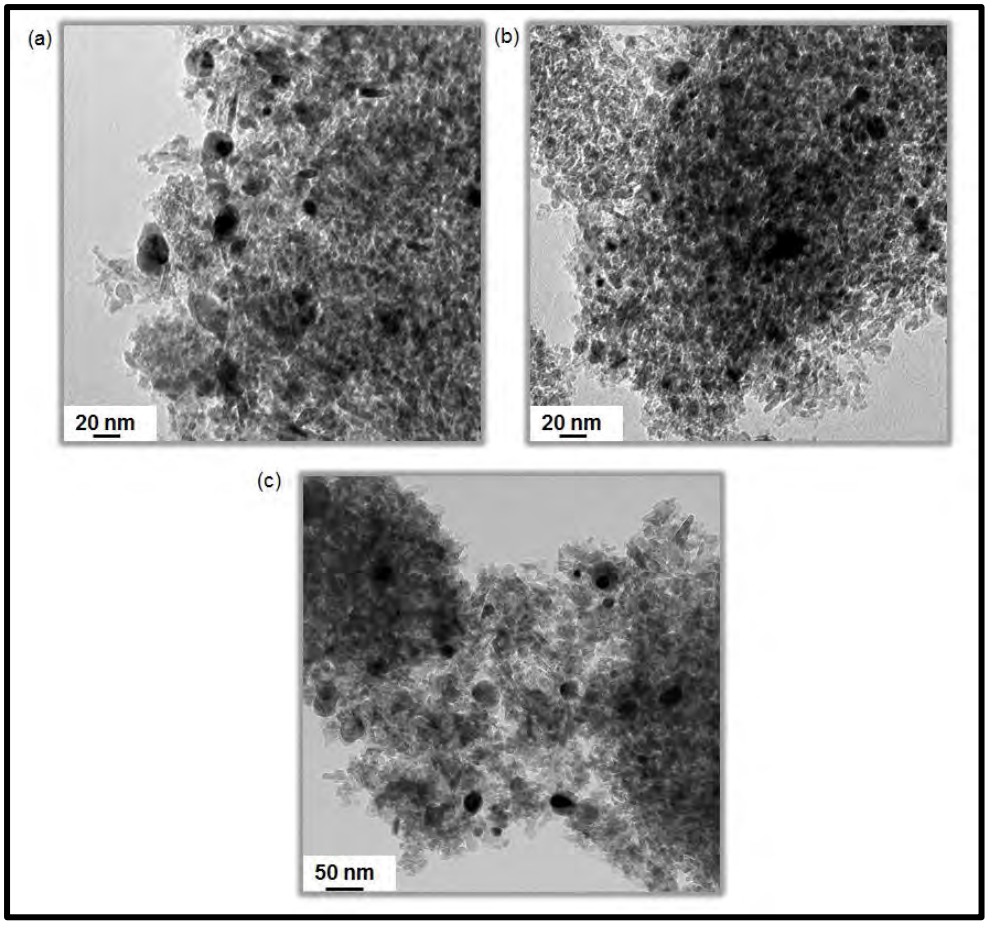

Figure 5.30. TEM micrographs model Ni catalyst ModCatH (a) post reduction (b) post sintering tests in an inert atmosphere (c) post sintering tests in a steam/hydrogen atmosphere

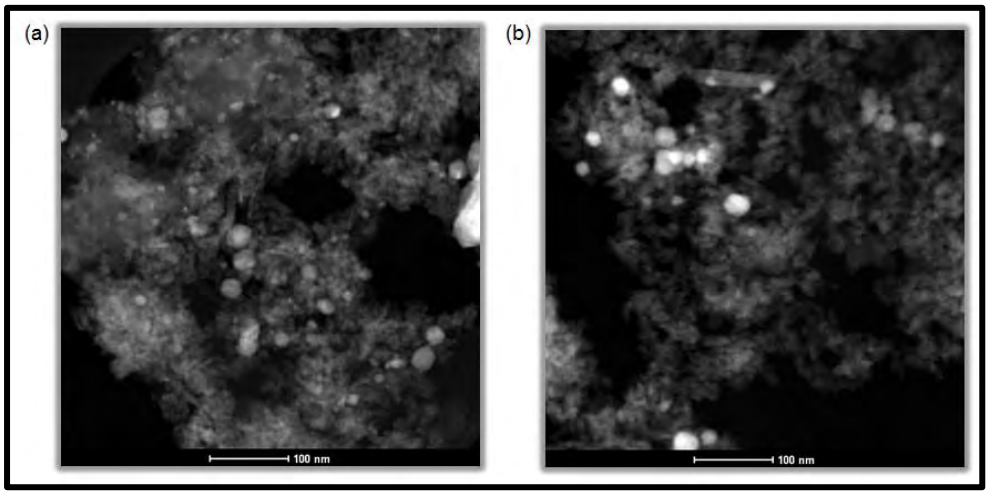

Figure 5.31. STEM micrographs model Ni catalyst ModCatH (a) post sintering tests in an inert atmosphere (b) post sintering tests in a steam/hydrogen atmosphere

Figure 5.32 and Figure 5.33 give an indication of the size distributions of the nanoparticles in the model catalysts after reduction, temperature tests, and water co-feed tests. When considering the size distribution data of ModCatC (Figure 5.32), it can be noted that during temperature tests, there was a shift in the size distribution to larger sizes. After exposure to water vapour, there was a significant shift in the distribution to larger sizes, with the formation of a large number of very big particles greater than 55 nm. A similar trend was observed for ModCatH (Figure 5.33). However, this shift in size distribution was less pronounced, suggesting that ModCatH was more stable than ModCatC under these conditions.

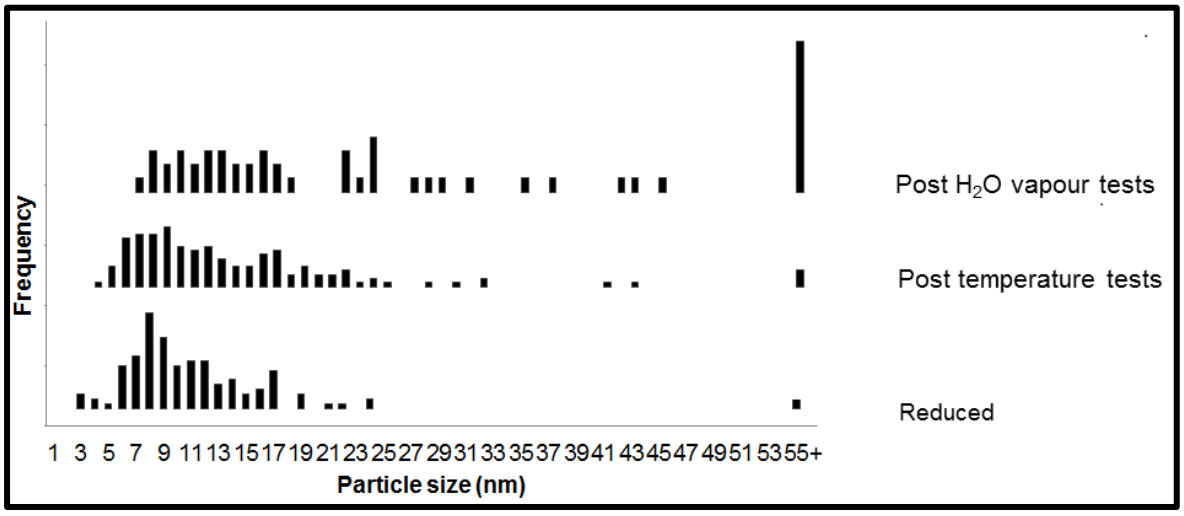

Figure 5.32. Size distributions for ModCatC after exposure to different conditions as obtained from TEM analysis

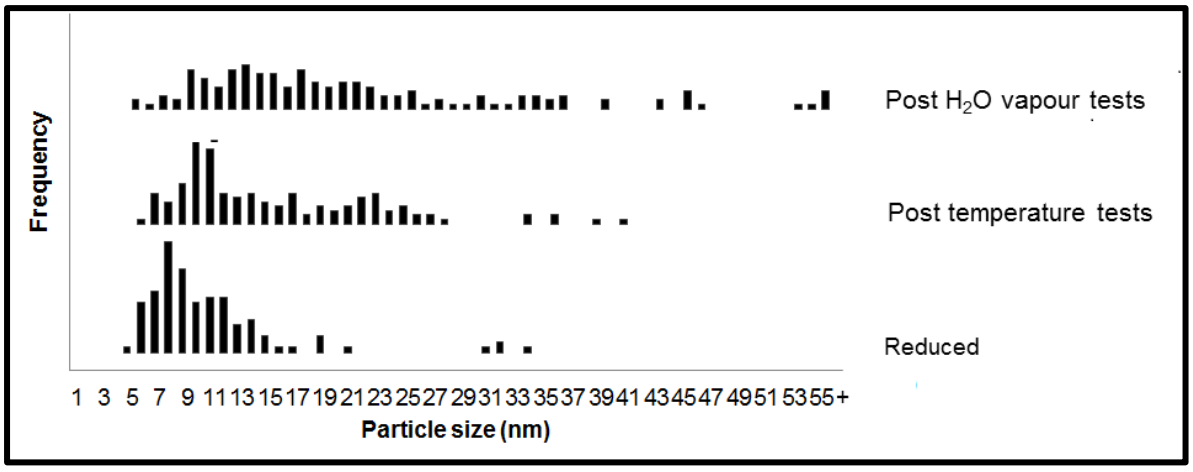

Figure 5.33. Size distributions for ModCatH after exposure to different conditions as obtained from TEM analysis

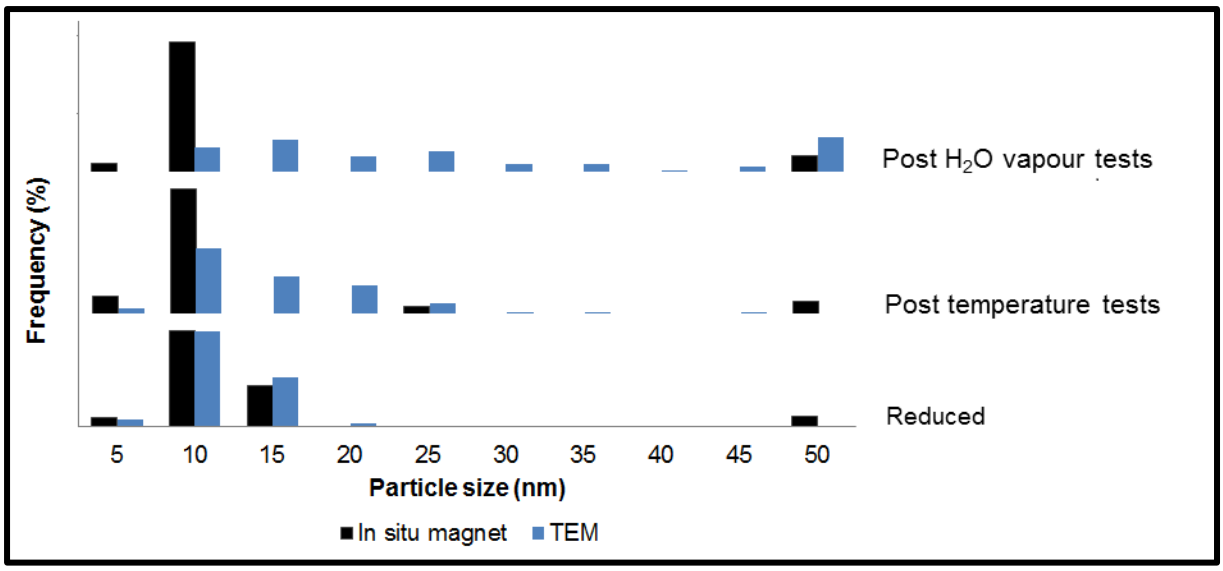

Figure 5.34. Comparison *in situ* magnetometer and TEM size for ModCatC after exposure to different conditions

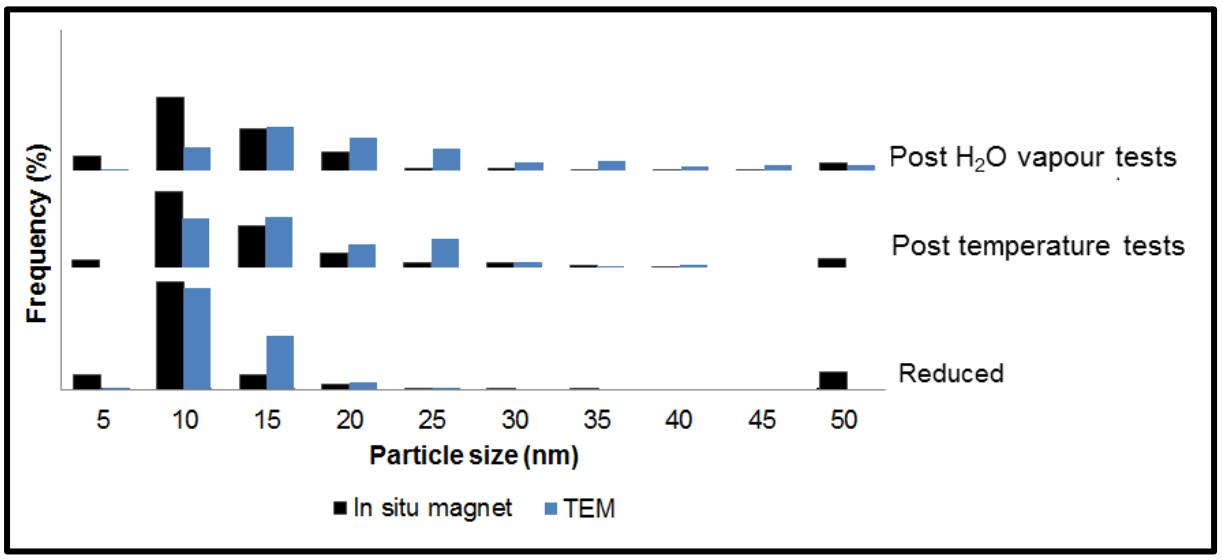

Figure 5.35. Comparison *in situ* magnetometer and TEM size for ModCatH after exposure to different conditions

Figure 5.34 and Figure 5.35 represent a comparison between the data obtained from TEM analysis and the *in situ* magnetometer. There was relatively good correlation between the data obtained from TEM data and the magnetometer for ModCatH. The Langevin equation can only be applied to superparamagnetic samples. ModCatH

sintered less extensively than ModCatC, retaining areas of good dispersion were particles behaved as single domains, thus allowing for the determination of size distributions over the whole range of reaction conditions. With ModCatC, due to severe particle growth, the particles no longer behaved as single domains and may have instead started to assume the magnetic behaviour of bulk nickel (ferromagnetic behaviour). This made any size distribution determinations using the Langevin equation difficult for this catalyst.

5.3.7. Summary

Model catalysts with a narrow size distribution were successfully synthesised by mechanically depositing nickel nanoparticles prepared using the reverse micelle technique onto the γ-alumina support. Decreasing the metal loading to 4.0 wt.% resulted in an improved dispersion of the nanoparticles on the support. From the *in situ* PXRD reduction of the model catalysts it was noted that the catalyst with smaller particles began its reduction at a lower temperature than the catalyst sample with larger particles. The model catalysts displayed sufficient reducibility to conduct a magnetic study. Both catalysts had similar size distributions after reduction. They, however, did not display similar behaviour during the sintering studies. The catalyst synthesised using smaller nanoparticles showed a far greater propensity to sinter, both in an inert and oxidising atmosphere. Due to the significant particle growth in this catalyst, the particles no longer behaved as single domains, making it difficult to extract size distribution data using magnetic measurements.

6. Conclusions

The reverse micelle technique was successfully employed to synthesise spherical NiO nanoparticles with a narrow size distribution, where the size of the particles was linearly dependent on the water/surfactant ratio. During calcination of the nanoparticles, large metallic nickel particles were formed. This was postulated to be as a result of the decomposition of the surfactant which created a reducing atmosphere. The tendency of the particles to aggregate then created an environment which promoted the sintering of the resultant nickel.

γ-alumina supported nanoparticles of two different sizes (approximately 5 nm and 12 nm) were prepared using two different preparation methods. The samples prepared by support addition during the microemulsion preparation step could not be fully characterised using PXRD or TEM analysis. The targeted metal loading could also not be achieved using this method. These samples also displayed poor reducibility which may have been as a result of the incorporation of the nickel into the support matrix, forming nickel aluminates.

The supported nanoparticles prepared by support addition to already synthesised and calcined nickel nanoparticles resulted in material which could be effectively characterised using PXRD and TEM. PXRD was used to determine average size, which correlated well with the average particle size and size distribution obtained from TEM analysis. The particles retained their narrow size distribution and spherical morphology on support addition. These samples also showed markedly improved reducibility, making them highly suitable for a magnetic investigation.

This method was then used in the synthesis of model catalysts which had a narrow size distribution. Decreasing the metal loading resulted in an improved dispersion of the nanoparticles on the support. Reduction in the *in situ* magnetometer showed that the catalyst prepared using larger particles achieved a higher DOR. Although both model catalysts had similar size distributions after reduction, they did not display similar behaviour during the sintering studies. The catalyst synthesised using smaller

nanoparticles sintered extensively in both an inert and oxidising atmosphere whilst the catalyst prepared using larger nanoparticles remained relatively stable.

7. Recommendations

One of the challenges encountered in this investigation was maintaining a very narrow size distribution for larger nanoparticles. Perhaps an additional factor could be investigated. Hada, *et al*. (2013) proposed the use of a blend of anionic and non-ionic surfactants in order to achieve improved size control.

The sintering study should be extended to include CO. This will allow for a complete comparison of how atmosphere affects the sintering process for supported crystallites of different sizes at elevated temperatures.

The model catalysts employed in this study sintered after reduction, with a broadening in the size distribution. In order to conduct a meaningful crystallite size study, a narrow size distribution was required. The reverse micelle technique could perhaps be extended to synthesise metallic nickel in the 2 – 15 nm size with a sufficiently narrow size distribution which could then be used in the sintering study.

References

Abrevaya, H., & Targos, W. (1987). *Patent No. 4 714 692.* United States of America.

Agnelli, M., Swaan, H., Marquez-Alvarez, C., Martin, G., & Mirodatos, C. (1998). CO Hydrogenation on a Nickel Catalyst. *Journal of Catalysis 175*, 117-128.

Ahmad, T., Ramanujachary, K., Lofland, S., & Ganguli, A. (2006). Magnetic and electrochemical properties of nickel oxide nanoparticles obtained by the reverse-micellar route. *Solid State Sciences 8*, 425-430.

Amekura, H., Fudamoto, Y., Takeda, Y., & Kishimoto, N. (2005). Curie transition of superparamagnetic nickel nanoparticles in silica glass: A phase transition in a finite size system. *Physical Review B 71*, 172404.

Atkinson, G., & Nicks, L. (1976). *Patent No. U.S. Patent Application 738,201.* United States of America.

Ayyappan, S., Srinivasa Gopalan, R., Subbanna, G., & Rao, C. (1997). Nanoparticles of Ag, Au, Pd, and Cu produced by alcohol reduction of salts. *Journal of Materials Research 12*, 398-401.

Barkhuizen, D., Mabaso, I., Viljoen, E., Welker, C., Claeys, M., van Steen, E., & Fletcher, J.C.Q. (2006). Experimental approaches to the preparation of supported metal nanoparticles. *Pure Applied Chemistry 78*, 1759-1769.

Bartholomew, C. (2001). Mechanisms of catalyst deactivation. *Applied Catalysis A: General 212*, 17-60.

Bartholomew, C., & Sorensen, W. (1983). Sintering Kinetics of Silica- and Alumina-Supported Nickel in Hydrogen Atmosphere. *Journal of Catalysis 81*, 131-141.

Bartholomew, C., Pannell, R., & Butler, J. (1980). Support and Crystallite Size Effects in CO Hydrogenation on Nickel. *Journal of Catalysis 65*, 335-347.

Bartholomew, C., Weatherbee, G., & Jarvi, G. (1979). Sulfur Poisoning of Nickel Methanation Catalysts I. In Situ Deactivation by H_2S of Nickel and Nickel Bimettallics. *Journal of Catalysis 60*, 257-269.

Bezemer, G., Bitter, J., Kuipers, H., Oosterbeek, H., Holewijn, J., Xu, X., Kapteijn, F., van Dillen, A.J., & de Jong, K.P. (2006). Cobalt Particle Size Effects in the Fischer-Tropsch Reaction Studied with Carbon Nanofiber Supported Catalysts. *Journal of the American Chemical Society 128*, 3956-3964.

Blanco, M., & Lopez-Quintela, M. (1997). Preparation of Nanoparticles in Microemulsions: A Monte Carlo Study of the Influence of the Synthesis Variables. *Langmuir 13*, 4527-4534.

Boudart, M., & McDonald, M. (1984). Structure Sensitlvlty of Hydrocarbon Synthesls from CO and H_2. *The Journal of Physical Chemistry 88*, 2185-2195.

Boutonnet, M., Kizling, J., & Stenius, P. (1982). The preparation of monodisperse colloidal metal particles from microemulsions. *Colloids and Surfaces 5*, 209-225.

Capek, I. (2004). Preparation of metal nanoparticles in water-in-oil (w/o) microemulsions. *Advances in Colloid and Interface Science 110*, 49-74.

Chandel, M., & Williams, E. (2009). *Synthetic Natural Gas (SNG): Technolohy, Environmental Implications, and Economics.* Duke University.

Cheang, V. (2009). *Effect of Crystallite Size and Water Partial Pressure on the Activity and Selectivity of Low Temperature Iron-based Fischer-Tropsch Catalysts.* PhD Thesis, University of Cape Town, Department of Chemical Engineering, Cape Town.

Cheng, F., & Dupont, V. (2013). Nickel catalyst auto-reduction during steam reformingof bio-oil model compound acetic acid. *International Journal of Hydrogen Energy 38*, 15160-15172.

Chernavskii, P., Dalmon, J.-A., Perov, N., & Khodakov, A. (2009). Magnetic Characterization of Fischer-Tropsch Catalysts. *Oil & Gas Science and Technology 64*, 25-48.

Claeys, M., van Steen, E., Visagie, J., & van de Loosdrecht, J. (2010). *Patent No. PCT patent WO 2010/004419 A2.*

Couchman, P., & Jesser, W. (1977). Thermodynamic theory of size dependence of melting temperature in metals. *Nature 269*, 481-483.

Dagle, R., Wang, Y., Xia, G.-G., Strohm, J., Holladay, J., & Palo, D. (2007). Selective CO methanation catalysts for fuel processing applications. *Applied Catalysis A: General 326*, 213-218.

Dalmon, J. (1994). Magnetic measurements and catalysis. In B. Imelik, & J. Verdrine (Eds.), *Catalyst characterisation: Physical techniques for solid materials* (p. 585). New York: Plenum Press.

Danielsson, I., & Lindman, B. (1981). The definition of microemulsion. *Colloids and Surfaces 3*, 391-392.

Datye, A., Xu, Q., Kharas, K., & McCarty, J. (2006). Particle size distributions in heterogenous catalysts: What do they tell us about the sintering mechanism? *Catalysis Today 111*, 59-67.

Dave, D. (2013). *Davy Methanation Process Technology.* IHS Chemical.

Derouane, E., Simoens, A., Colin, C., Martin, G., Dalmon, J., & Vedrine, J. (1978). Effect of Particle Size and Degree of Reduction on the Magnetic Properties of Dispersed Nickel Catalysts. *Journal of Catalysis 52*, 50-58.

Du, Y., Wang, W., Li, X., Zhao, J., Ma, J., Liu, Y., & Lu, G. (2012). Preparation of NiO nanoparticles in microemulsion and its gas sensing performance. *Materials Letters 68*, 168-170.

Eastoe, J., Hollamby, M., & Hudson, L. (2006). Recent advances in nanoparticle synthesis with reversed micelles. *Advances in Colloid and Interface Science 128-130*, 5-15.

Eastoe, J., Hollamby, M., & Hudson, L. (2006). Recent advances in nanoparticle synthesis with reversed micelles. *Advances in Colloid and Interface Science 128-130*, 5-15.

Enger, B., & Holmen, A. (2012). Nickel and Fischer-Tropsch Synthesis. *Catalysis Reviews: Science and Engineering 54*, 437-488.

Erekson, E., & Bartholomew, C. (1983). Sulfur Poisoning of Nickel Methanation Catalysts II. Effects of H2S Concentration, CO and H_2O Partial Pressures and Temperature on Deactivation Rates. *Applied Catalysis 5*, 323-336.

Eriksson, S., Nylen, U., Rojas, S., & Boutonnet, M. (2004). Preparation of catalysts from microemulsions and their applications in heterogeneous catalysis. *Applied Catalysis A: General 265*, 207-219.

Er-rbib, H., & Bouallou, C. (2014). Modelling and simulationof CO methanation process for renewable electricity storage. *Energy* , 1-8.

Fischer, N. (2011). *Preparation of Nano and Angstrom sized Cobalt Ensembles and their Performance in the Fischer-Tropsch Synthesis.* PhD Thesis, University of Cape Town, Department of Chemical Engineering, Cape Town.

Fischer, N., Clapham, B., Feltes, T., van Steen, E., & Claeys, M. (2014). Size-dependent phase transformation of catalytically active nanoparticles captured in situ. *Angewandte Chemie International Edition 53*, 1342-1345.

Fischer, N., van Steen, E., & Claeys, M. (2011). Preparation of supported nano-sized cobalt oxide and fcc cobalt crystallites. *Catalysis Today 171*, 174-179.

Fitzharris, W., Katzer, J., & Manogue, W. (1982). Sulfur Deactivation of Nickel Methanation Catalysts. *Journal of Catalysis 76*, 369-384.

Forzatti, P., & Lietti, L. (1999). Catalyst deactivation. *Catalysis Today 52*, 165-181.

Fujita, S.-I., & Takezawa, N. (1997). Difference in the selectivity of CO and CO_2 methanation reactions. *Chemical Engineering Journal 68*, 63-68.

Gao, J., Jia, C., Zhang, M., Gu, F., Xu, G., & Su, F. (2013). Effects of nickel nanoparticle size in Ni/α-Al_2O3 on CO methanation reaction for the production of synthetic natural gas. *Catalysis Science and Technology 3*, 2009-2015.

Gao, J., Wang, Y., Ping, Y., Hu, D., Xu, G., Gu, F., Xu, G., & Su, F. (2012). A thermodynamic analysis of methanation reactions of carbon oxides for the production of synthetic natural gas. *RSC Advances 2*, 2358-2368.

Gong, W., Li, H., Zhao, Z., & Chen, J. (1991). Ultrafine particles of Fe, Co, and Ni ferromagnetic metals. *Journal of Applied Physics 69*, 5119-5121.

Gorke, O., Pfeifer, P., & Schubert, K. (2005). Highly selective methanation by the use of a microchannel reactor. *Catalysis Today 110*, 132-139.

Hada, R., Rani, A., Devra, V., & Amritphale, S. (2013). A Novel Process for Making Nickel Oxide Nanoparticles. *International Research Journal of Pure & Applied Chemistry 3*, 111-117.

Han, D., Yang, H., Shen, C., Zhou, X., & Wang, F. (2004). Synthesis and size control of NiO nanoparticles by water-in-oil microemulsion. *Powder Technology 147*, 113-116.

Haryanto, A., Fernando, S., Pordesimo, L., & Adhikari, S. (2009). Upgrading of syngas derived from biomass gasification: A thermodynamic analysis. *Biomas and Bioenergy 33*, 882-889.

Haynes, W., Forney, A., Elliot, J., & Pennline, H. (1974). Synthesis of methane in hot gas recycle reactor: pilot plant tests. *American Chemical Society Division of Fuel Chemistry 19*, 10-19.

He, X., & Shi, H. (2012). Size and shape effects on magnetic properties of Ni nanoparticles. *Particuology 10*, 497-502.

Holm, V., & Clark, A. (1968). Reduction Studies on Supported Metal Oxide Catalysts. *Journal of Catalysis 11*, 305-316.

Hu, D., Gao, J., Ping, Y., Jia, L., Gunawan, P., Zhong, Z., Xu, G., Gu, F., & Su, F. (2012). Enhanced Investigation of CO Methanation over Ni/Al_2O_3 Catalysts for Synthetic Natural Gas Production. *Industrial & Engineering Chemistry Research 51*, 4875-4886.

Huang, Y., Chen, H., Su, J., & Xiao, T. (2014). Highly active and selective catalyst for synthetic natural gas (SNG) production. *Applied Petrochemical Research 4*, 81-88.

Hwang, S., Lee, J., Hong, U., Seo, J., Jung, J., Koh, D., Lim, H., Byun, C., & Song, I.K. (2011). Methane production from carbon monoxide and hydrogen over nickel–alumina. *Journal of Industrial and Engineering Chemistry 17*, 154-157.

Jasik, A., Wojcieszak, R., Monteverdi, S., Ziolek, M., & Bettahar, M. (2005). Study of nickel catalysts supported on Al_2O_3, SiO_2 or Nb_2O_5 oxides. *Journal of Molecular Catalysis A: Chemical 242*, 81-90.

Jensen, J., Poulsen, J., & Andersen, N. (2011, March-April). From coal to clean energy. *Nitrogen+Syngas 310*, pp. 34-38.

Jurascik, M., Sues, A., & Ptasinski, K. (2009). Exergetic evaluation and improvement of biomass-to-synthetic natural gas. *Energy and Environmental Science 2*, 791-801.

Karellas, S., Panopoulos, K., Panousis, G., Rigas, A., Karl, J., & Kakaras, E. (2012). An evaluation of Substitute natural gas production from different coal gasification. *Energy 45*, 183-194.

Katz, J., & Miquel, P. (1994). Syntheses and applications of oxides and mixed oxides produced by a flame process. *Nanostructured Materials 4*, 551-557.

Kester, K., Zagli, E., & Falconer, J. (1986). Methanation of carbon monoxide and carbon dioxide on Ni/Al_2O_3 catalysts: effects of nickel loading. *Applied Catalysis 22*, 311-319.

Kishida, S., & Teranishi, S. (1968). Kinetics of Liquid-Phase Hydrogenation of Acetone over Raney Nickel Catalyst. *Journal of Catalysis 12*, 90-96.

Kondrat, S., Davies, T., Zu, Z., Boldrin, P., Bartley, J., Carley, A., Taylor, S.H., Rosseinsky, M.J., & Hutchings, G.J. (2011). The effect of heat treatment on phase transformation of copper manganese oxide: Influence on catalytic activity for ambient temperature carbon monoxide oxidation. *Journal of Catalysis 281*, 279-289.

Lee, S. (2007). Gasification of Coal. In *Handbook of Alternative Fuel Technology.* Florida: Taylor & Francis Group, LLC.

Li, C., & Chen, Y.-W. (1995). Temperature-programmed-reduction studies of nickel oxide/alumina catalysts: effects of the preparation method. *Thermochimica Acta 256*, 457-465.

Li, G., Hu, L., & Hill, J. (2006). Comparison of reducibility and stability of alumina-supported Ni catalysts prepared by impregnation and co-precipitation. *Applied Catalysis A: General 301*, 16-24.

Liu, J., Shen, W., Cui, D., Yu, J., Su, F., & Xu, G. (2013). Syngas methanation for substitue natural gas over Ni-Mg/Al_2O_3 catalyst in fixed and fluidized bed reactors. *Catalysis Communications 38*, 35-39.

Liu, Z., Chu, B., Zhai, X., Jin, Y., & Cheng, Y. (2012). Total methanation of syngas to synthetic natural gas over Ni catalyst in a micro-channel reactor. *Fuel 95*, 599-605.

Lopez-Quintela, M., & Rivas, J. (1993). Chemical Reactions in Microemulsions: A Powerful Method to Obtain Ultrafine Particles. *Journal of Colloid and Interface Science158*, 446-451.

Luterbacher, J., Froling, M., Vogel, F., Marechal, F., & Tester, J. (2009). Hydrothermal Gasification of Waste Biomass: Process Design and Life Cycle Assessment. *Environmental Science and Technology 43*, 1578-1583.

Mabaso, E. (2005). *Nanosized Iron Crystallites for Fischer-Tropsch Synthesis.* PhD Thesis, University of Cape Town, Department of Chemical Engineering, Cape Town.

McCarthy, J., & Wise, H. (1979). Hydrogenation of Surface Carbon on Alumina-Supported Nickel. *Journal of Catalysis 57*, 406-416.

Mihaly, M., Comanescu, A., Rogozea, A., Vasile, E., & Meghea, A. (2011). NiO-silica based nanostructured materials obtained by microemulsion assisted sol-gel procedure. *Materials Research Bulletin 46*, 1746-1753.

Mills, G. (1971). Gas from coal - fuel of the future. *Environmental Science and Technology*, 1178-1183.

Moon, Y., Lee, J., Kim, J., Jung, M., Lee, J., & Kim, S. (2009). Sintering kinetic measurement of nickel nanoparticle agglomerates by electrical mobility classification. *Current Applied Physics 9*, 928-932.

Moulijn, J., van Diepen, A., & Kapteijn, F. (2001). Catalyst deactivation: is it predictable? What to do? *Applied Catalysis A: General 212*, 3-16.

Munnik, P., Velthoen, M., de Jongh, P., de Jong, K., & Gommes, C. (2014). Nanoparticle Growth in Supported Nickel Catalysts during Methanation Reaction - Larger is Better. *Angewandte Chemie 126*, 9647-9651.

Nepijko, S., & Wiesendanger, R. (1995). Size Dependence of the Curie Temperature of Separate Nickel Particles Studied by Interference Electron Microscopy. *Europhysics Letters 31*, 567-572.

Ojeda, M., Rojas, S., Boutonnet, M., Perez-Alonso, F., Garcia-Garcia, F., & Fierro, J. (2004). Synthesis of Rh nano-particles by the microemulsion technology Particle size effect on the CO + H_2 reaction. *Applied Catalysis A: General 274*, 33-41.

Pileni, M.-P. (1993). Water in oil colloidal droplets used as microreactors. *Advances in Colloid and Interface Science, 46*, 139-163.

Rahimpour, M., Dehnavi, M., Allahgholipour, F., Iranshahi, D., & Jokar, S. (2012). Assessment and comparison of different catalytic coupling exothrmic and endothermic reactions: A review. *Applied Energy 99*, 496-512.

Rasmussen, F., Sehested, J., Teunissen, H., Molenbroek, A., & Clausen, B. (2004). Sintering of Ni/Al_2O_3 catalysts studied by anomalous small angle X-ray scattering. *Applied Catalysis A: General 267*, 165-173.

Richardson, J., & Crump, J. (1979). Crystallite Size Distributions of Sintered Nickel Catalysts. *Journal of Catalysis 57*, 417-425.

Richardson, J., & Propp, J. (1986). Pore Size Effects on Ni/Al_2O_3 Catalysts. *Journal of Catalysis 98*, 457-467.

Robinson, B., Towey, T., Zourab, S., Visser, A., & van Hock, A. (1991). Characterisation of cadmium sulphide colloids in reverse micelles. *Colloids and Surfaces 61*, 175-188.

Rostrup-Nielsen, J., Pedersen, K., & Sehested, J. (2007). High temperature methanation Sintering and structure sensitivity. *Applied Catalysis A: General 330*, 134-138.

Rynkowski, J., Paryjczak, T., & Lenik, M. (1993). On the nature of oxidic nickel phases in NiO/γ-Al_2O_3 catalysts. *Applied Catalysis A: General 106*, 73-82.

Schwarz, J., Contescu, C., & Contescu, A. (1995). Methods for Preparation of Catalytic Materials. *Chemical Reviews 95*, 477-510.

Seglin, L., & Geosits, R. (1975). Survey of Methanation Chemistry and Processes. In *Methanation of Synthesis Gas* (pp. 1-7). Washington, DC: American Chemical Society.

Sehested, J., Dahl, S., Jacobsen, J., & Rostrup-Nielsen, J. (2005). Methanation of CO over Nickel: Mechanism and Kinetics at High H_2/CO Ratios. *Journal of Physical Chemistry B 109*, 2432-2438.

Sehested, J., Gelten, J., & Helveg, S. (2006). Sintering of nickel catalysts: Effects of time, atmosphere, temperature, nickel-carrier interactions, and dopants. *Applied Catalysis A: General 309*, 237-246.

Sehested, J., Gelten, J., Remediakis, I., Bengaard, H., & Norskov, J. (2004). Sintering of nickel steam-reforming catalysts: effects of temperature and steam and hydrogen pressures. *Journal of Catalysis 223*, 432-443.

Serway, R., & Jewett, Jr., J. (2014). *Physics for Scientists and Engineers with Modern Physics.* Boston: Brooks/Cole.

Shen, W., Dumesic, J., & Hill, J. C. (1981). Criteria for Stable Ni Particle Size under Methanation Reaction Conditions: Nickel Transport and Particle Size Growth via Nickel Carbonyl. *Journal of Catalysis 68*, 152-165.

Song, K., & Kim, J. (1999). Preparation of Nanosize Tin Oxide Particles from Water-in-Oil Microemulsions. *Journal of Colloid and Interface Science 212*, 193-196.

Sudiro, M., & Bertucco, A. (2010). *Synthetic Natural Gas (SNG) from coal and biomass: a survey of existing process technologies, open issues and perspectives*. Retrieved August 26, 2014, from Natural Gas: http://www.intechopen.com/books/natural-gas/syntheticnatural-gas-sng-from-coal-and-biomass-a-survey-of-existing-process-technologies-open-issue

The DOW Chemical Company. (2013). *Thermal degradation of ethoxylated nonionic surfactants*. Retrieved July 28, 2014, from DOW Answer Center: dowac.custhelp.com/app/answers/detail/a_id/2017/~/thermal-degradation-of-ethoxylated-nonionic-surfactants

Tian, D., Liu, Z., Li, D., Shi, H., Pan, W., & Cheng, Y. (2013). Bimetallic Ni–Fe total-methanation catalyst for the production of substitute. *Fuel 104*, 224-229.

Trimm, D. (1983). Catalyst Design for Reduced Coking (Review). *Applied Catalysis 5*, 263-290.

University of South Dakota. (n.d.). *Pyrophoric Materials.* Retrieved August 25, 2014, from USD Environmental, Health and Safety Department: ehs@usd.edu

Utaka, T., Takeguchi, T., Kikuchi, R., & Eguchi, K. (2003). CO removal from reformed fuels over Cu and precious metal catalysts. *Applied Catalysis A: General 246* , 117-124.

van Meerten, R., Beaumont, A., van Nisselrooij, P., & Coenen, J. (1983). Structure sensitivity and crystallite size change of nickel during methanation of CO/H_2 on nickel-silica catalysts. *Surface Science 135*, 565-579.

Vannice, M. (1975). The Catalytic Synthesis of Hydrocarbons from H_2/CO Mixtures over the Group VIII Metals. *Journal of Catalysis 37*, 449-461.

Vannice, M. (1976). The Catalytic Synthesis of Hydrocarbons from H_2/CO Mixtures over the Group VIII Metals IV. The Kinetic Behavior of CO Hydrogenation over Ni Catalysts. *Journal of Catalysis 44*, 152-162.

Watson, G. (1980). *Methanation catalysts.* London: International Energy Agency Coal Research.

Williams, A., Butler, G., & Hammonds, J. (1972). Sintering of Nickel-Alumina Catalysts. *Journal of Catalysis 24*, 352-355.

Yan, X., Liu, Y., Zhao, B., Wang, Z., Wang, Y., & Liu, C.-J. (2013). Methanation over Ni/SiO_2: Effect of the catalyst. *International Journal of Hydrogen Energy 38*, 2283-2291.

Zhao, A., Ying, W., Zhang, H., Ma, H., & Fang, D. (2012). $Ni–Al_2O_3$ catalysts prepared by solution combustion method for syngas methanation. *Catalysis Communications 17*, 34-38.

Appendix A: Calibration of magnetometer

100 mg of bulk nickel oxide was placed into the *in situ* magnetometer. The sample was then heated to 700 °C (heating rate: 4 °C/min) in 100 mL (NTP)/min of hydrogen. Thereafter, the gas was changed from hydrogen to argon (100 mL (NTP)/min) and held for 2 hours. The sample was then cooled to 25 °C (cooling rate: 1 °C/min) and held at 25 °C for 3 hours.

A calibration factor was obtained for the *in situ* magnetometer by comparing the mass specific saturation magnetisation of Ni at 27 °C, reported as 43.8 emu/g (Gong, *et al*., 1991), with the signal obtained in the *in situ* magnetometer for a known mass of Ni at the same temperature (3.13 a.u./g). Multiplying the two together results in a calibration factor for the *in situ* magnetometer – 14 emu/a.u. This converts the signal to magnetic units.

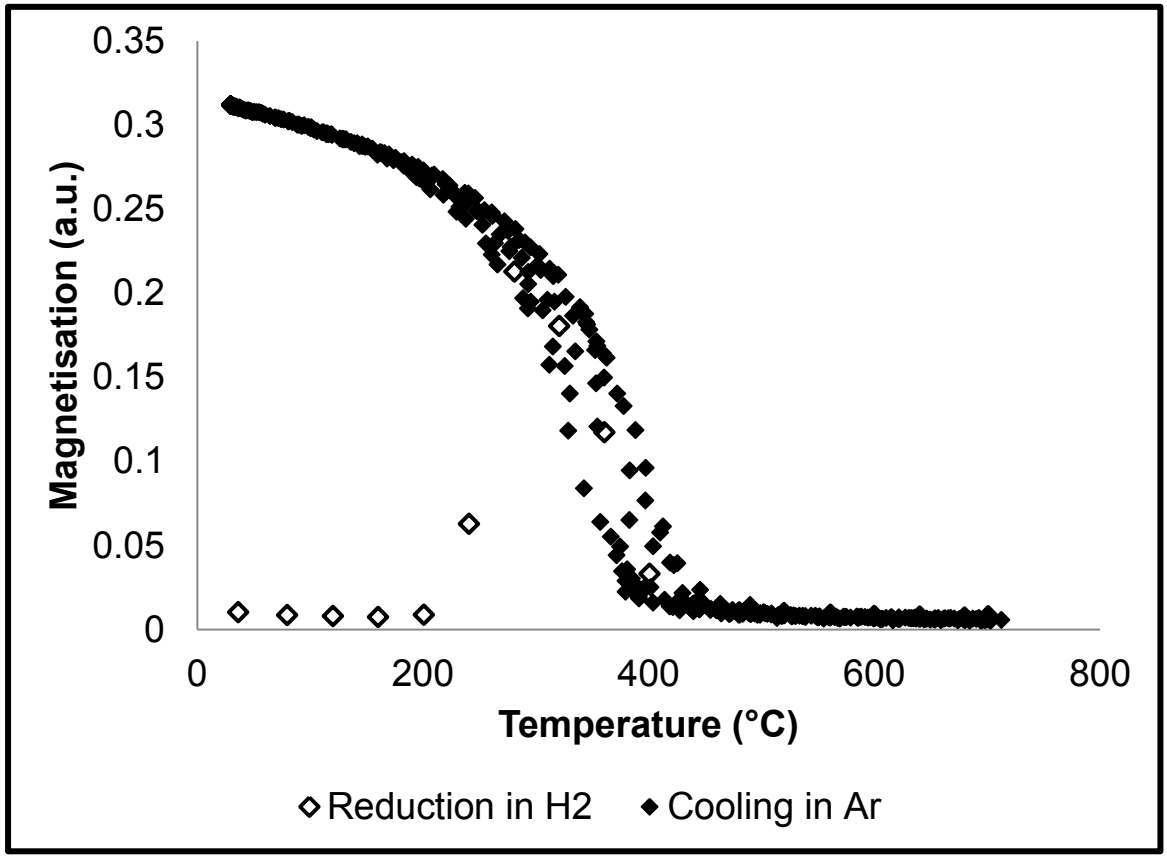

Figure A.1. Reduction of bulk nickel oxide in *in situ* magnetometer

Appendix B: Hysteresis measurements

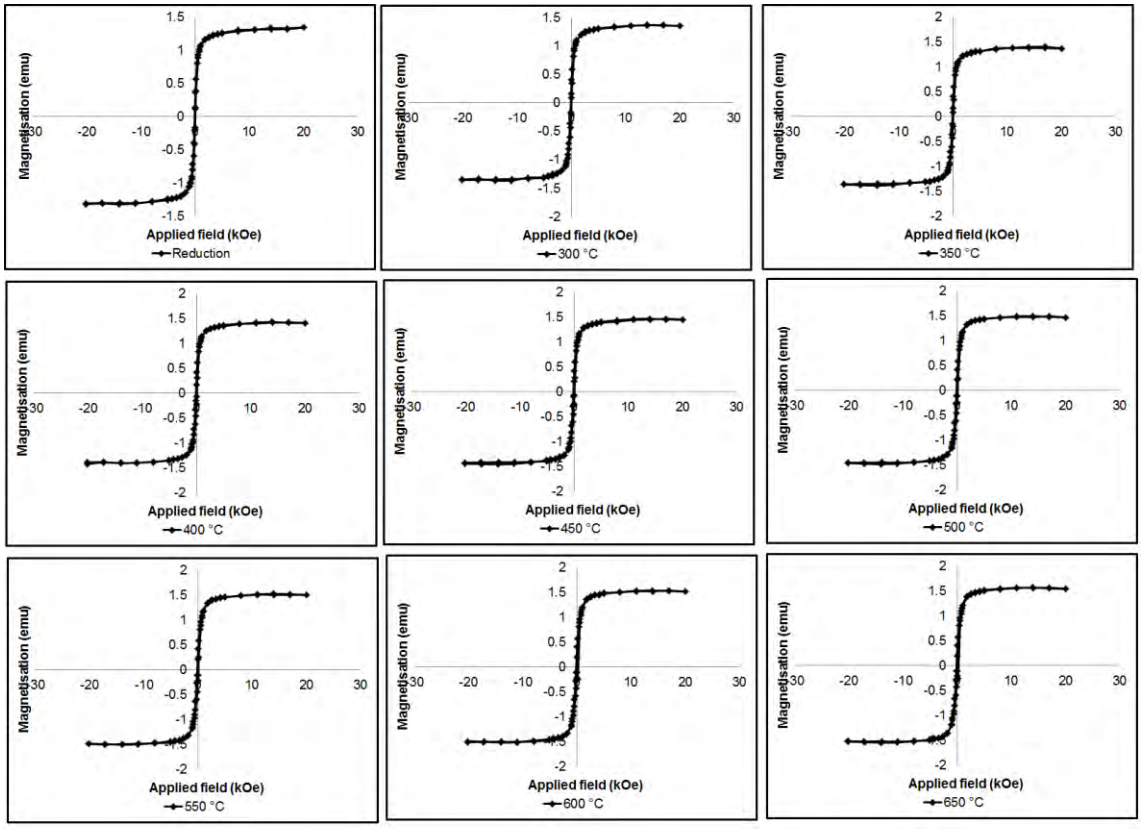

Figure B.1. Hysteresis data recorded at 150 °C after thermal sintering tests in an inert atmosphere for ModCatC

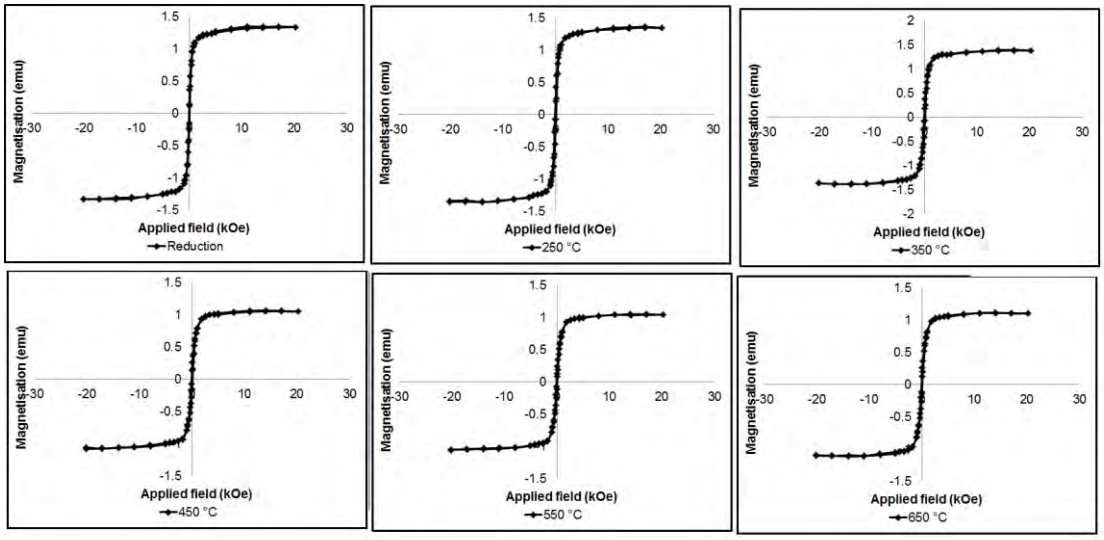

Figure B.2. Hysteresis data recorded at 150 °C after thermal sintering tests in a steam/hydrogen atmosphere for ModCatC

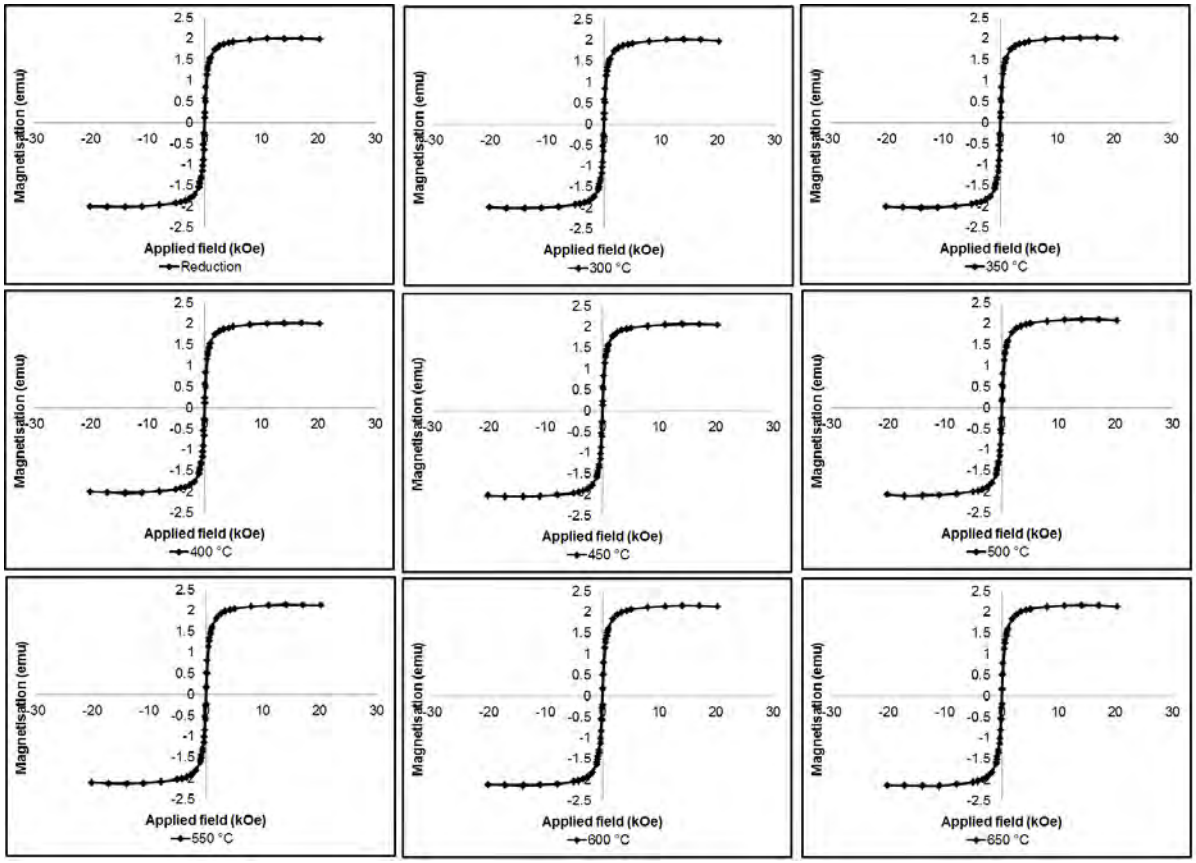

Figure B.3. Hysteresis data recorded at 150 °C after thermal sintering tests in an inert atmosphere for ModCatH

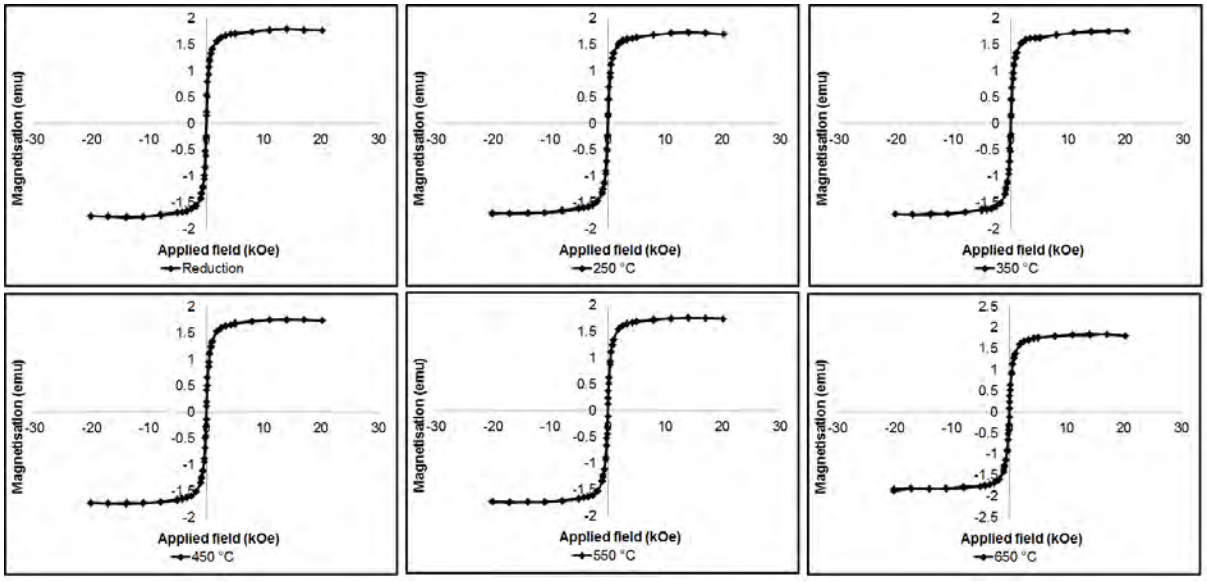

Figure B.4. Hysteresis data recorded at 150 °C after thermal sintering tests in a steam/hydrogen atmosphere for ModCatH

Appendix C: Analysis of a diffractogram using TOPAS

Rietveld refinement using TOPAS was used in order to extract average crystallite size data from PXRD diffractograms. Prior to refinement, an attempt was made to identify all phases present in the sample to be investigated. The corresponding structure files were then obtained for each component. In this study the phases of interest were NiO, metallic Ni and γ-alumina.

Firstly, a program file with the specifications of the PXRD instrument was loaded. This was followed by replacing the scan data with the scan to be analysed (1). The most appropriate order of magnitude for the background was then selected (2) and the zero correction (3) refined then fixed for all subsequent calculations. The structure files of the components present in the scan to be investigated were then loaded (4).

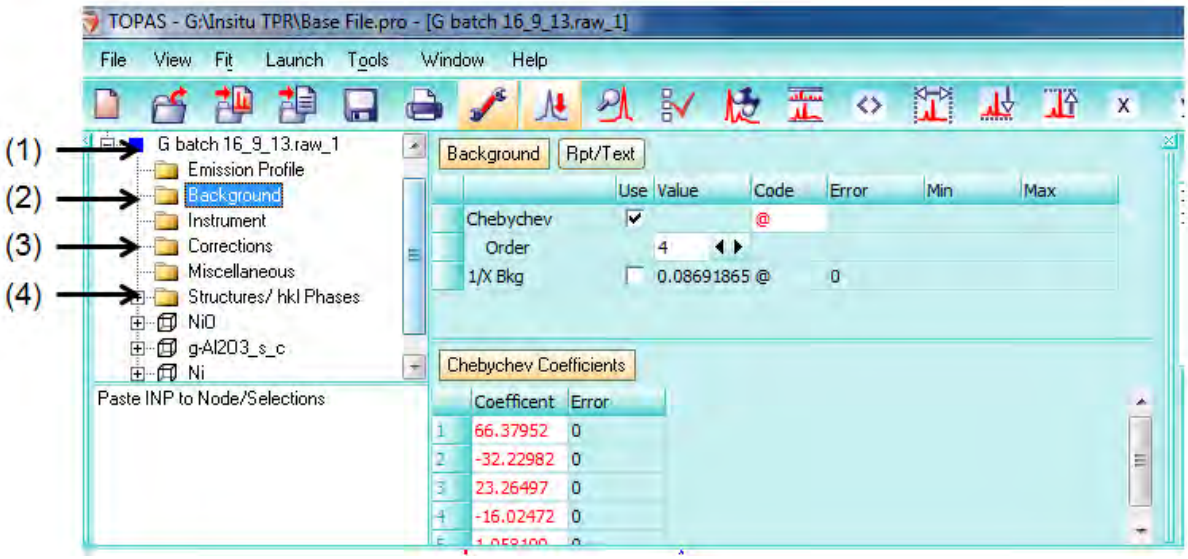

The model parameters associated with each component (5) were continuously refined (6) until there was a sufficiently good fit (R_{wp} < 10) between the actual and the calculated diffraction pattern.

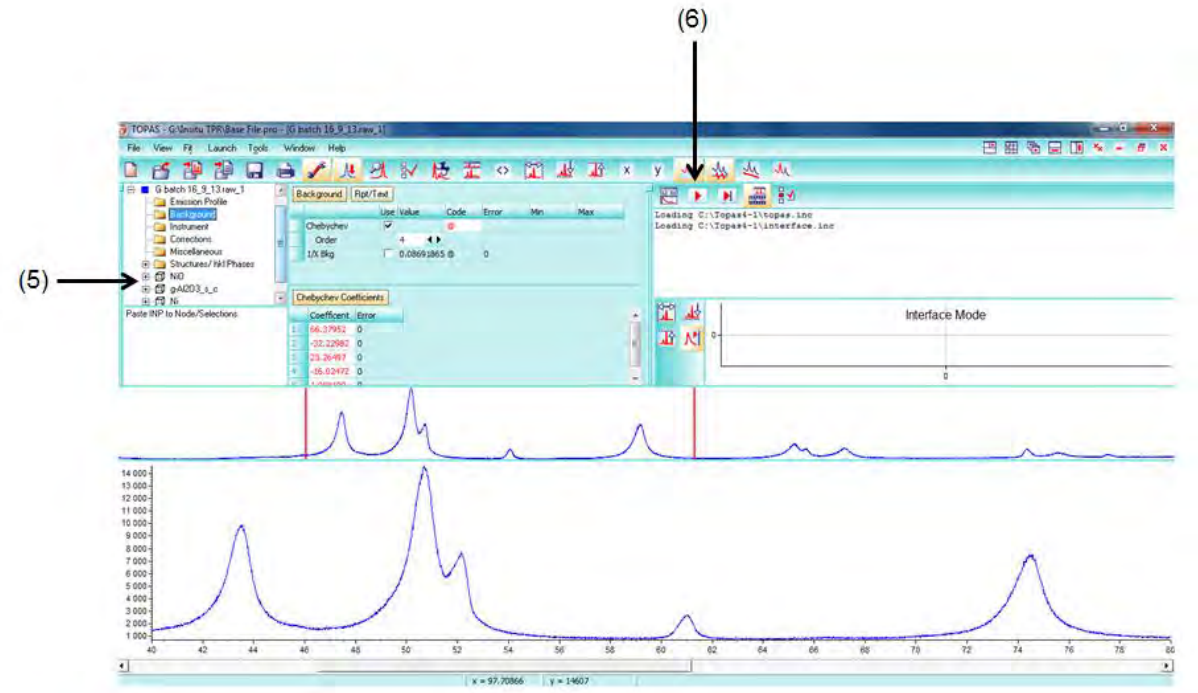

Once an acceptable R_{wp} value has been obtained (7), the crystallite size (8) as well as the relative phase compositions (9) corresponding with the calculated diffraction pattern can be found.

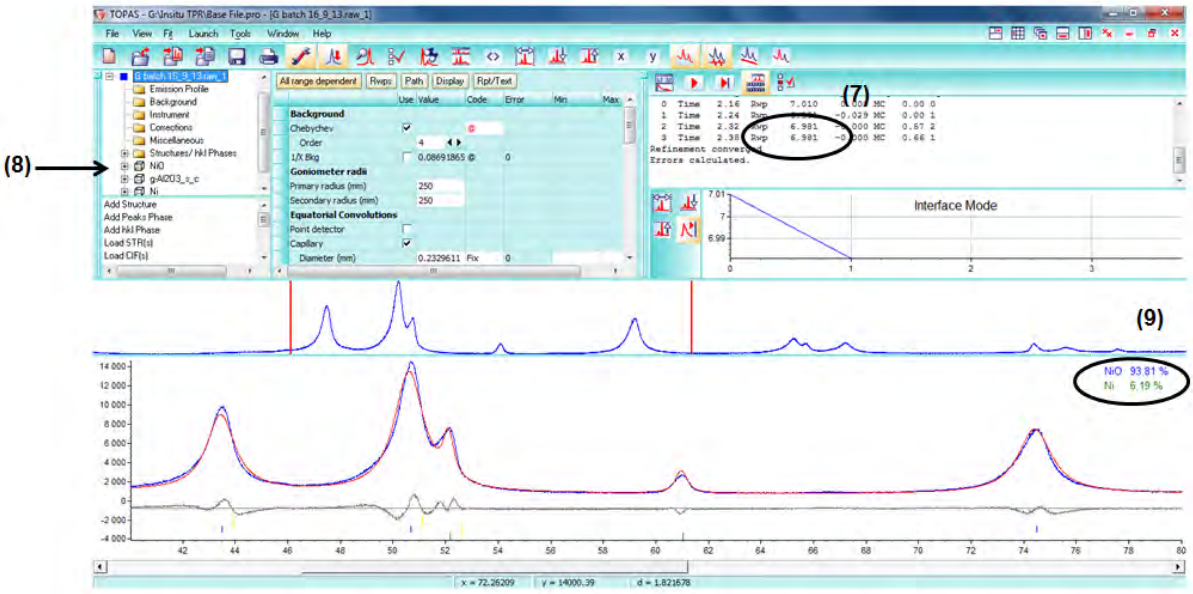

Appendix D: Analysis of hysteresis data using Langevin equation

Hysteresis data is recorded between -20 kOe and 20 kOe. When applying the Langevin equation in order to determine crystallite size, only the data collected between 20 kOe and 0 kOe is considered.

The magnetisation (M) as a function of the reciprocal of the applied field (1/H) is then plotted (Figure D.1). By considering the region of the graph where the data points become linear, a straight line could be drawn and extrapolated to 1/H = 0. At this point, the applied field approaches infinity and the corresponding magnetisation is the saturation magnetisation (M_S).

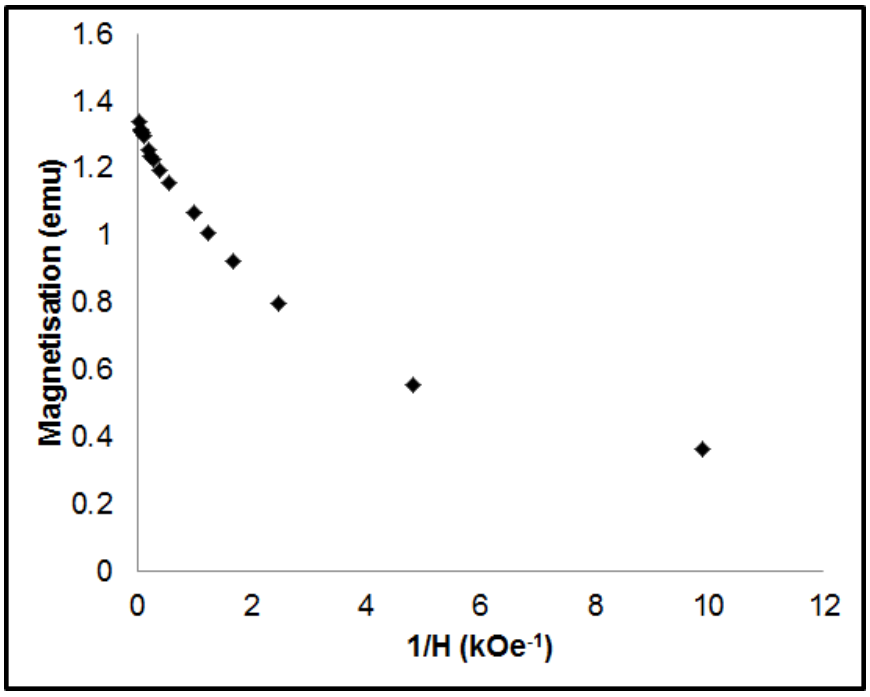

Figure D.1. Magnetisation as a function of the reciprocal of the applied field

M/M_S can then be determined for the experimental data points.

The Langevin equation is then used to estimate crystallite size. Multiple functions are plotted by varying the crystallite size. The contribution from each fit is then used to determine crystallite size distribution.

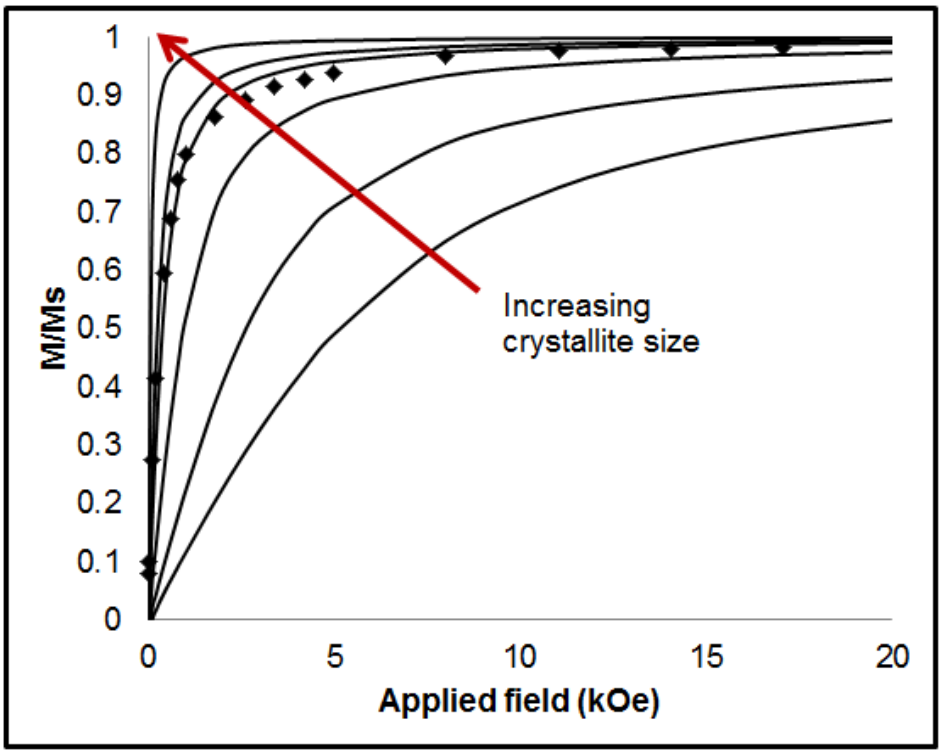

Figure D.2. Langevin functions for various crystallite sizes